



Universitat Autònoma de Barcelona

ADVERTIMENT. L'accés als continguts d'aquesta tesi queda condicionat a l'acceptació de les condicions d'ús establertes per la següent llicència Creative Commons:  http://cat.creativecommons.org/?page_id=184

ADVERTENCIA. El acceso a los contenidos de esta tesis queda condicionado a la aceptación de las condiciones de uso establecidas por la siguiente licencia Creative Commons:  <http://es.creativecommons.org/blog/licencias/>

WARNING. The access to the contents of this doctoral thesis it is limited to the acceptance of the use conditions set by the following Creative Commons license:  <https://creativecommons.org/licenses/?lang=en>

Photoactive Materials Based on Cyclodextrin-Functionalized Gold Nanoparticles

Marc Padilla Barriento

2017

Director/s:

Dr Jordi Hernando Campos

Dr José Luis Bourdelande

Programa de Doctorat en Química

Departament de Química

Universitat Autònoma de Barcelona

Table of Contents

TABLE OF CONTENTS

Abbreviations	1
Chapter 1. Introduction	
1.1. Gold nanoparticles	6
1.1.1. Optical properties of gold nanoparticles.....	7
1.1.2. Applications of the optical properties of gold nanoparticles.....	8
1.2. Supramolecular Host-Guest Chemistry	13
1.2.1. Supramolecular hosts.....	13
1.2.2. Combined use of gold nanoparticles and supramolecular hosts	15
1.3. Bibliography	18
Chapter 2. Objectives	21
Chapter 3. Synthesis and characterization of host-functionalized gold nanoparticles	
3.1. Introduction	25
3.1.1. Cyclodextrins, the family of supramolecular hosts of choice	25
3.1.2. Cyclodextrin-functionalized gold nanoparticles	27
3.1.3. Objectives: preparation of cyclodextrin-functionalized gold nanoparticles	29
3.2. Preparation of thiolated cyclodextrin derivatives	31
3.2.1. Perthiolation vs monothiolation of β -CD: a case study.....	32
3.2.2. Perthiolation of α -CD: synthesis of α -CD-(SH) ₆	38
3.2.3. Perthiolation of γ -CD: synthesis of γ -CD-(SH) ₈	41
3.3. Synthesis and characterization of cyclodextrin functionalized gold nanoparticles	43
3.3.1. Direct synthesis of cyclodextrin-functionalized gold nanoparticles	43
3.3.2. Indirect synthesis of cyclodextrin-functionalized gold nanoparticles.....	47

3.4. Summary and conclusions	62
3.5. Bibliography	64

Chapter 4. Photocatalysis with gold nanoparticles

4.1. Introduction	69
4.1.1. Mechanism of photocatalytic action	69
4.1.2. Direct photocatalysis vs use of other (photo)catalysts	73
4.1.3. Strategies of use	74
4.1.4. Objectives: a new strategy for the use of Au NPs as photocatalysts based on supramolecular chemistry	78
4.2. Photocatalysis of unimolecular reactions	80
4.2.1. Synthesis of (<i>Z</i>)-stilbenes	81
4.2.2. Host-guest supramolecular interaction between β -CD and stilbenes	82
4.2.3. Preparation and characterization of β -CD-coated Au NPs	84
4.2.4. Photochemical and thermal isomerization of stilbenes	88
4.2.5. Photocatalytic studies with gold nanoparticles	91
4.2.6. Photocatalytic mechanism of (<i>Z</i>)-stilbenes isomerization with Au NPs	101
4.3. Photocatalysis of bimolecular reactions	107
4.3.1. Photoinduced [4+4] cycloaddition of 2-anthracenecarboxylate	107
4.3.2. Preparation of gold nanoparticles functionalized with γ -cyclodextrin	109
4.3.3. Photocatalytic dimerization of 2-anthracenecarboxylate with gold nanoparticles.....	111
4.4. Summary and conclusions	113
4.5. Bibliography	114

Chapter 5. Controlled assembly using cyclodextrin-based supramolecular chemistry

5.1. Introduction	119
5.1.1- Cyclodextrin-based methodologies for the assembly of plasmonic nanoparticles.....	119

5.1.2- Objectives: stimulus-responsive heteroassemblies of gold nanoparticles via cyclodextrin-based supramolecular chemistry.....	127
5.2. Synthesis and photochemical characterization of the ligands.....	129
5.2.1-Synthesis of OEG-SH	130
5.2.2- Synthesis of Azo-OEG-1	133
5.2.3 Synthesis of Azo-OEG-2	137
5.2.4- Photochemical characterization of Azo-OEG-2	139
5.2.5- Host-Guest complexation of Azo-OEG-2 with α-CD	143
5.3. Preparation of gold nanoparticles functionalized with a-cyclodextrin and azobenzene ligands.....	145
5.3.1- Preparation of citrate-stabilized Au NPs using the seed-growth method..	145
5.3.2- Preparation of α -CD(SH) ₆ -functionalized gold nanoparticles: AuNP-G0@αCD and AuNP-G5@αCD	148
5.3.3. Preparation of azobenzene/olygoethyleneglycol-functionalized gold nanoparticles: AuNP-Gn@ AzoOEG/OEG	149
5.4. Supramolecular host-guest self-assembly of gold nanoparticles	155
5.4.1- Ligand-free AuNP homoassembly	156
5.4.2- Ligand-induced Au NP homoaggregation.....	161
5.4.3- Ligand-induced Au NP heteroaggregation.....	164
5.5. Summary and conclusions	170
5.6 Biblioigraphy	172
Chapter 6. General conclusions	173
Chapter 7. Experimental section	179
Formula index	221
Annex spectra of selected compounds	225

ABBREVIATIONS

ACN	Acetonitrile	EtOAc	Ethyl acetate
Ac ₂ O	Acetic anhydride	EtOH	Ethanol
Ad-NH ₂	1-Adamantylamine	GC	Gas chromatography
anh	Anhydrous	HEPES	4-(2-hydroxyethyl)-1-piperazineethane sulfonic acid
aq	Aqueous	HPLC	High performance liquid chromatography
atm	Atmosphere	HRMS	High resolution mass spectrometry
<i>c</i>	Concentration	ICP-MS	Inductively-coupled plasma mass spectrometry
CB	Cucurbituril	IE	Ionization energy
CD	Cyclodextrin	IR	Infrared
CE	Counter electrode	KSAC	Potassium thioacetate
DCC	<i>N,N'</i> -dicyclohexyl carbodiimide	LSPR	Localized surface plasmon resonance
DCU	<i>N,N'</i> -dicyclohexyl urea	MALDI-TOF	Matrix-assisted laser desorption ionization-time of flight
DLS	Dynamic light scattering	MetOH	Methanol
DMAP	4-dimethylaminopyridine	NIR	Near-infrared
DMF	<i>N,N'</i> -dimethylformamide	NMR	Nuclear magnetic resonance
DMSO	Dimethylsulfoxide	NP	Nanoparticle
DNA	Deoxiribonucleic acid	NR	Nanorod
DOSY	Diffusion-ordered spectroscopy	OEG	Olygoethylene glycol
DTCC	Dithiocarbamate calixarene	RE	Reference electrode
EGFR	Epidermal growth factor receptor	rpm	Round per minute
E _{ox}	Oxidation Potential		
ESI	Electrospray ionization		
exc	Excitation		
ET	Energy transfer		

rt	Room temperature
PEG	Polyethylene glycol
Ph	Phenyl
PSS	Phostationary state
PTE	Photothermal effect
PTT	Photothermal therapy
PVP	Polyvinylpirrolidone
Pyr	Pyridine
SAM	Self-assembled monolayer
SCE	Saturated calomel electrode
SERS	Surface Enhanced Raman Spectroscopy
THF	Tetrahydrofuran
TEM	Transmission electron microscopy
TLC	Thin layer chromatography
TPA	Two-photon absorption
TsCl	Tosyl chloride
UV	Ultra-violet
WE	Working electrode
vis	Visible
2P	Two-photon

Chapter 1:

Introduction



During the last decades, the development of nanostructures and functional nanomaterials has been one of the principal motors of scientific research.¹ Nanomaterials are defined as collections of atoms, ions or molecules with at least one spatial dimension within the range 1 - 100 nm. The main reasons that justify the interest for such structures are²: (i) their high surface-to-volume ratio, which is greater than that of bulk materials, and therefore, can be exploited in applications where surface effects play a key role (for example, in heterogeneous catalysis); (ii) quantum confinement effects, which emerge when the quasi-continuous energy band structure of bulk materials breaks down into a set of separated electronic states as size is reduced to the nanoscale, thus leading to novel properties for nanomaterials. These two factors are strongly relevant in the case of nanoparticles (NPs), a type of nanomaterial which is characterized for presenting nanometer sizes in all dimensions.¹ Among them, gold nanoparticles (Au NPs) are the object of interest of this thesis.

1.1.- GOLD NANOPARTICLES

Au NPs are clusters of Au atoms in their elementary state with varying sizes between 1 – 100 nm, which can have different morphologies depending on the synthetic conditions employed for their preparation (Figure 1.1A).³ Owing to their combination of properties, these nanomaterials are among the most studied metal NPs nowadays.⁴ However, their use dates back to ancient times, well before any knowledge on Au NPs had already been acquired. This is the case of the manufacturing of colored glass, in which ruby red colors were obtained by the addition of a gold salt during the fabrication process that resulted in the formation of nanoparticles. One of the most famous examples of this type of material is the Lycurgus Cup, a 4th century Roman glass cup that shows red color in transmission (i.e. when lit from behind) and green color in reflection (i.e. when lit from in front, Figure 1.1B).⁵ Such dichroic behavior is caused by the particular optical properties of Au NPs, which will be discussed in detail below. In addition, Au NPs present other interesting features which make them very attractive for various applications. First of all, they present high chemical stability in contrast with other metal NPs like Ag or Cu NPs, which are more prone to be oxidized. Furthermore, they are easy to functionalize with (bio)organic ligands⁶ and biocompatible,^{7,8} making them versatile platforms for biological and medical applications. Finally, Au NPs can also act as efficient catalysts of different reactions.⁹

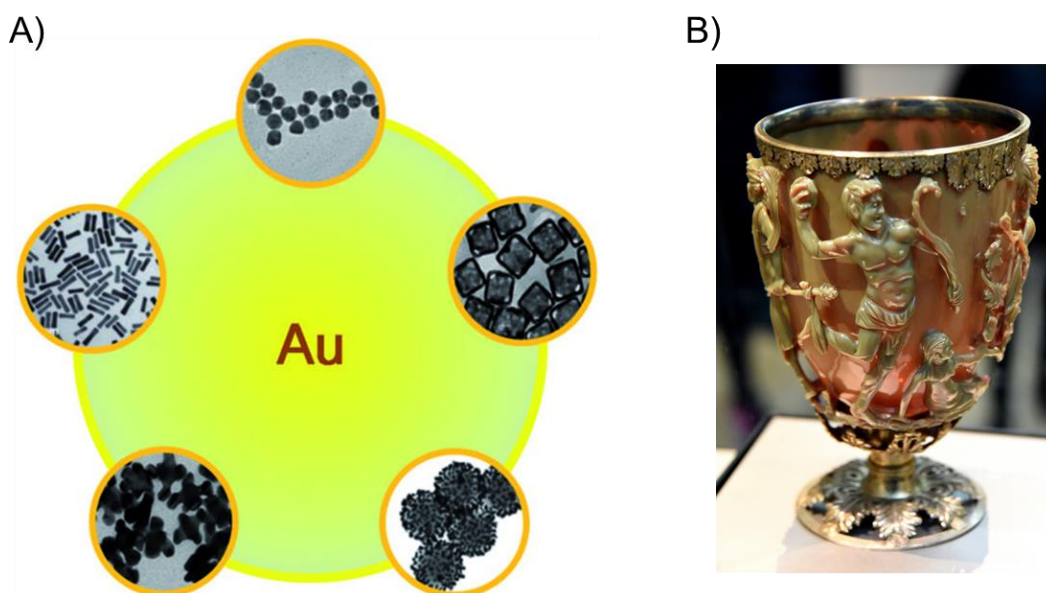


Figure 1.1. A) Distinct Au NP morphologies achieved under different synthetic conditions. Reproduced from reference 3. B) Image of the Roman Lycurgus Cup made of dichroic glass due to the presence of silver and gold NPs. Reproduced from reference ¹⁰

1.1.1.- Optical properties of gold nanoparticles: plasmonic effects

An interesting feature of Au NPs is the red color shown by their colloidal suspensions (Figure 1.2A). This color is a fingerprint of the intricate optical properties that this type of nanomaterials present, which are a direct consequence of a physical phenomenon called localized surface plasmon resonance (LSPR) or plasmon. When a metal NP is irradiated with light, the oscillation of the incident electric field generates the coherent oscillation of the conduction band electrons at the surface of the NP (Figure 1.2B).¹¹ This phenomenon is due to: (i) the reduced size of the NPs, which is much smaller than the wavelength of the incident light when UV, visible or IR radiation is used; (ii) the high polarizability of the metal atoms which the NP is composed of. Under certain circumstances, the frequency of the excitation light may become resonant to the dipole induced on the surface of the NP by the oscillatory electron cloud, which is then dramatically amplified and leads to the excitation of the plasmon of the nanoparticle. As a consequence of this excitation, light of certain wavelengths is selectively dispersed or absorbed by the NPs, thus making their colloidal suspensions to present defined colors, as evidenced by naked eye inspection or by recording their extinction spectra^A (Figure 1.2A).

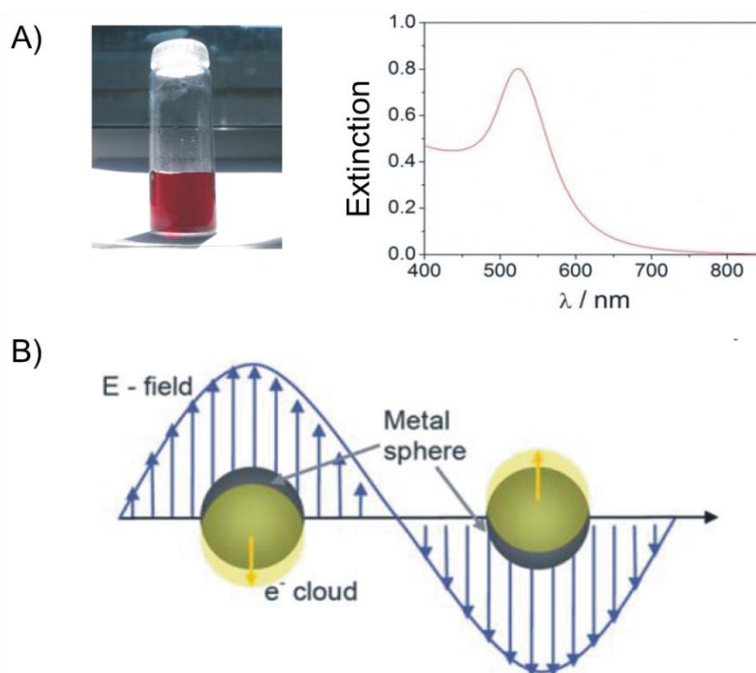


Figure 1.2. A) Picture and extinction spectrum of a colloidal suspension of spherical Au NPs of ~20 nm diameter in water. B) Schematic illustration of the oscillating electron cloud generated

^A Extinction spectra are measured with UV-Vis spectrophotometers and, for colloidal suspensions of NPs, they arise from the combination of absorption and dispersion signals.

on the surface of Au NPs upon light irradiation, which causes the excitation of its surface plasmon. Adapted from reference 8.

The spectral range where LSPR excitation and dispersion take place is determined by four different factors: the composition, the size and the shape of the NPs and the dielectric constant of the surrounding medium.¹² As can be observed in Figure 1.2A, these phenomena are observed at around 530 nm for spherical Au NPs of around 20 nm in diameter suspended in aqueous media, meaning that their plasmon resonance can be excited with green light from the visible spectrum. Bigger NPs would exhibit a bathochromical shift of their LSPR, whereas a hypsochromical shift would be observed for smaller NPs.

1.1.2.- Applications of the optical properties of gold nanoparticles

The interesting plasmon-based optical properties of Au NPs have given rise to a plethora of potential applications in numerous and diverse fields of research such as sensing, nanomedicine and catalysis, among others. In this section, some of the most remarkable applications of the optical properties of gold nanoparticles will be highlighted, with the exception of those related to catalysis and Au NP assembly which will be thoroughly discussed in Chapters 4 and 5, respectively.

(a) Gold nanoparticles as colorimetric sensors

One of the most exploited plasmon-based features of Au NPs is the environment dependency of their extinction spectra. In particular, variation of the dielectric constant of the surrounding medium by simply modifying the coating layer around the nanoparticles or, more dramatically, by inducing nanoparticle aggregation, results in measurable spectral changes.¹³ As such, colorimetric sensing of ions, small organic molecules or even large biomolecules such as proteins and nucleic acids can be achieved upon direct adsorption onto Au NPs or, more preferably, upon analyte-promoted particle assembly.¹⁴ One of the first examples of this type of application was reported by Mirkin *et al*, who developed a colorimetric method for the detection of polynucleotides using mercaptoalkyl-oligonucleotide-modified Au NPs.¹⁵ Two distinct Au NP sets were capped with different single-stranded DNA oligonucleotides. Upon addition of a single-stranded oligonucleotide composed by two fragments complementary to the sequences on the NP surfaces to a colloidal dispersion of the modified Au NPs, the formation of a polymeric Au NP network and the subsequent color change from red to pinkish/purple was observed (Figure 1.3).

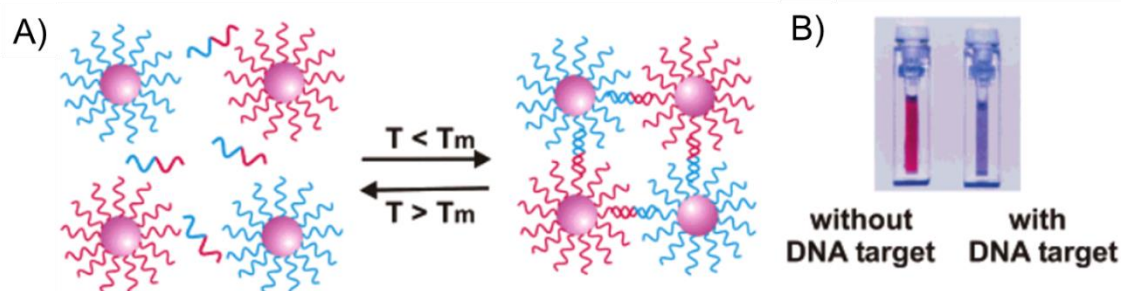


Figure 1.3. A) Schematic representation of oligonucleotide-functionalized Au NPs aggregation in the presence of complementary target DNA. B) Samples without (red) and with (blue) the target DNA showing distinct color due to Au NP aggregation.

(b) Plasmon-enhanced spectroscopies

The optical properties of Au NPs have also led to the improvement of already existing analytical techniques. For instance, this is the case of Raman spectroscopy, which enables measuring the vibrational spectrum of a sample from the inelastic scattering of photons. Unfortunately, this process is known to present extreme low cross-sections for molecules, which makes it of limited use for (bio)chemical sensing. However, when molecules lie in close contact to plasmonic nanostructures like Au NPs, a dramatic increase of their Raman signal is observed, which may reach up to 14 orders of magnitude.¹³ This phenomenon is called surface-enhanced Raman scattering (SERS) and it is mainly attributed to the electric field enhancement of the incident radiation that takes place around Au NPs upon plasmon excitation. As if Au NPs behave as antennae, the intensity of such dispersed radiation is amplified up to several orders of magnitude with respect to the incident beam. This process, however, only affects the near-field component of the radiation, which corresponds to evanescent waves that are generated on the surface of the NPs and the intensity of which decays exponentially with the distance. Since it provides a fingerprint of analytes by measuring their vibrational spectra, the discovery of SERS has revolutionized the application of Raman spectroscopy in analytical and medical fields. A very nice example of use of SERS was recently reported by Long *et al.*¹⁶ These authors described the intracellular detection of superoxide radical anion ($O_2^{\cdot-}$) down to 10^{-8} M using Au NPs functionalized with cytochrome c as SERS nanosensors (Figure 1.4).

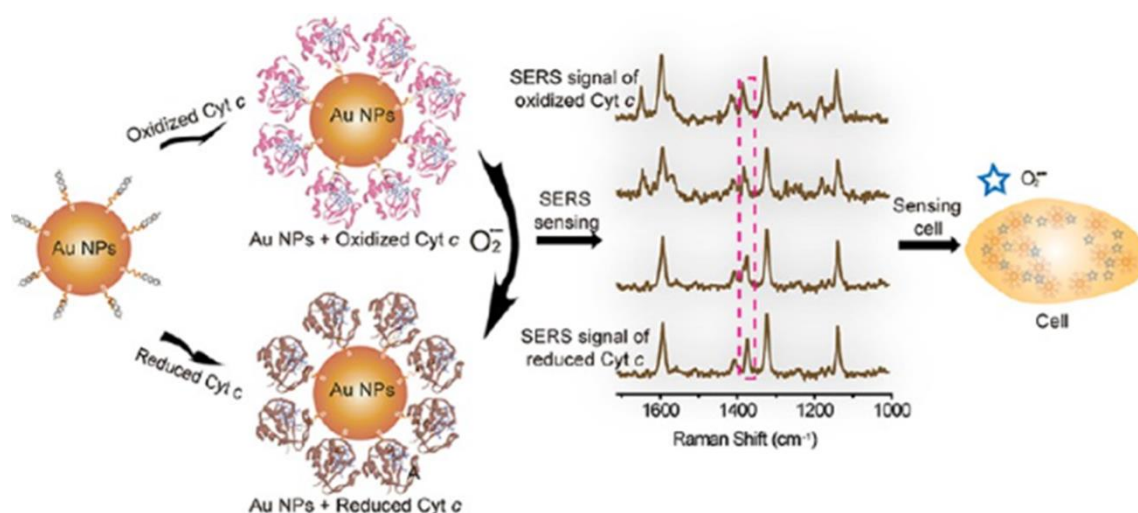


Figure 1.4. Intracellular superoxide radical anion detection with Au NPs decorated with cytochrome c. Reproduced from reference 16.

The combined use of fluorescence spectroscopy with the plasmonic properties of Au (and other metal) NPs has also received strong attention. Although luminescence quenching is often observed when fluorophores lie in close proximity to metals, plasmon-induced enhancement of the incident electromagnetic radiation and of the radiative rate of the emitter also take place in the case of Au NPs. Overall, this may lead to an increase of the emission intensity if luminescent compounds are placed at proper nanometer-scale distances from the plasmonic structures, thereby increasing the sensitivity of fluorescence spectroscopy.^{17,18,19}

Electromagnetic field enhancement effects mainly accounting for these plasmon-enhanced spectroscopies are very sensitive to the shape, size and arrangement of Au NPs. By appropriately varying these parameters, dramatic field enhancements can be generated in certain areas around the plasmonic nanostructures, which are commonly referred as *hot spots*.^{20,21} For instance, this can be achieved by plasmon coupling between Au NPs approached at very short distances, as shown in Figure 1.5. This finding has raised special interest towards the preparation of Au NP assemblies as platforms for SERS and luminescence-enhanced spectroscopy.²² Special attention will be given to this topic in Chapter 5.

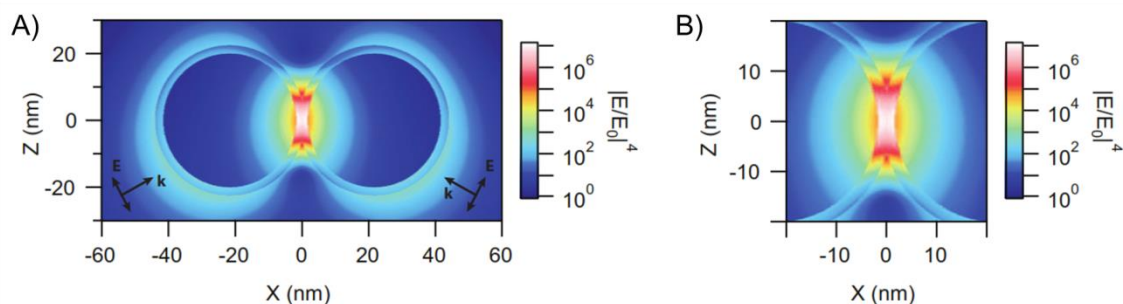


Figure 1.5. A) Near-field map of the fourth power of the on-resonance field-enhancement $|E/E_0|^4$ for a dimer structure in water. The dimer is capped with a 2.5 nm thick layer of single-stranded DNA which has an effective refractive index of 1.7. The gap between the gold nanoparticles is confined to 3.3 nm. B) Enlarged version of the gap region.

(c) Photothermal therapy

A very important application of the optical properties of Au NPs is photothermal therapy (PTT), which has been developed in the field of nanomedicine.²³ This application takes profit of the heat release exhibited by Au NPs upon plasmon excitation, a process called photothermal effect (PTE). This effect is due to the major relaxation pathway of the excited LSPR, which is produced by collisions between the oscillating electron cloud and the NP nuclei through electron-phonon interactions. This phenomenon generates heat homogeneously in the lattice of the NP that dissipates to the surrounding medium. Even though such heat release only contributes to a small increase in the macroscopic temperature of the sample, the temperature rise can be in the range of several hundreds of degrees at very short distances from the NPs.^{24,25} Upon irradiation with ns-pulsed lasers of suitable wavelength, targeted Au nanostructures can induce bacterial and cancer cell death due to the local heating produced by plasmon excitation (Figure 1.6).^{26,27}

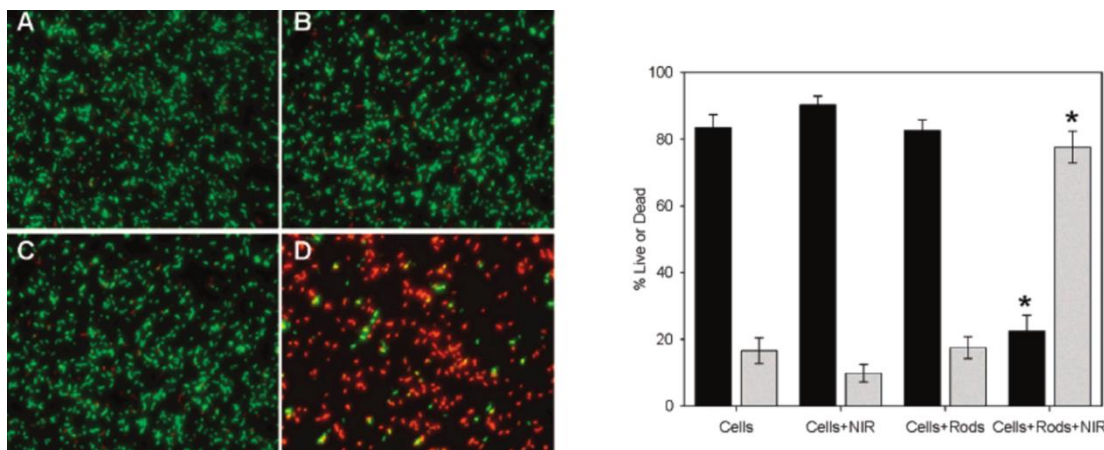


Figure 1.6. Viability of *Pseudomonas aeruginosa* cells with attached gold nanorods following exposure to NIR light. Left panels: A) Control cells without nanorods or NIR exposure, B) cells without nanorods exposed to NIR, C) cells with nanorods without NIR exposure and D) Cells with nanorods and exposed to NIR for 10 min. Green fluorescent cells are representative of live cells while red fluorescent are representative of dead or compromised cells. The graph on the right shows the quantified LIVE/DEAD data. Adapted from reference 26.

(d) Photovoltaics

The application of the optical properties of Au NPs has also been expanded to the energy conversion field. In particular, plasmonics has gained increasing attention as one of the solutions to improve the performance of photovoltaic devices, since the use of Au (or other metal) nanostructures may enhance several of the key processes occurring in these materials.²⁸ On the one hand, simple dispersion of light by Au NPs or, even better, electromagnetic field enhancement effects have been shown to increase the efficiency of photon absorption by nearby semiconductors. On the other hand, Au NPs can also act as photosensitizers which, upon light absorption and plasmon excitation, inject high energy charge carriers (electrons or holes) to the surrounding semiconductors, thus rising the efficiency of charge generation. Based on these distinct phenomena, enhanced performances have been achieved for different types of photovoltaic devices like silicon, polymer-based, dye-sensitized and perovskite solar cells.²⁸

1.2.- SUPRAMOLECULAR HOST-GUEST CHEMISTRY

Most of the applications of Au NPs discussed above require the approach of the compounds of interest to their surface (e.g. of analytes for SERS detection) and/or the assembly of nearby nanoparticles (e.g. for hot spot generation). The main objective of this thesis has been to explore the use of supramolecular chemistry to promote these processes and, as a result, enhance the plasmon-based activity of Au NPs.

Supramolecular chemistry studies the interaction between atomic, ionic and molecular fragments by means of intermolecular forces such as hydrogen bonding, van der Waals interactions or π -stacking instead of covalent bonds. Supramolecular host-guest complexes are among the most important supramolecular systems, and they are usually formed by large molecules presenting inner cavities (hosts) and small molecules or ions which are capable to fit inside these cavities through noncovalent interactions (guests).

1.2.1.- Supramolecular hosts

Figure 1.7 shows the structure of some of the most important supramolecular hosts developed to date. Although calix[n]arenes, cyclodextrins and cucurbit[n]urils were first synthesized more than seventy years ago, the serendipitous discovery of crown ethers by Pedersen in the 1960s constituted a major breakthrough in the field of host-guest supramolecular chemistry, as recognized by the Nobel Committee in 1987. In their simplest form, crown ethers are defined as macrocyclic oligomers of ethylene oxide and they are capable to efficiently bind alkali and alkaline-earth metal ions.²⁹ Cram and Lehn, who shared the Nobel Prize in Chemistry with Pedersen, later on synthesized 3-dimensional analogues of crown ethers, such as cryptands, which exhibit even larger association constants with alkali and alkaline-earth metal ions due to the higher preorganization of their binding sites.³⁰

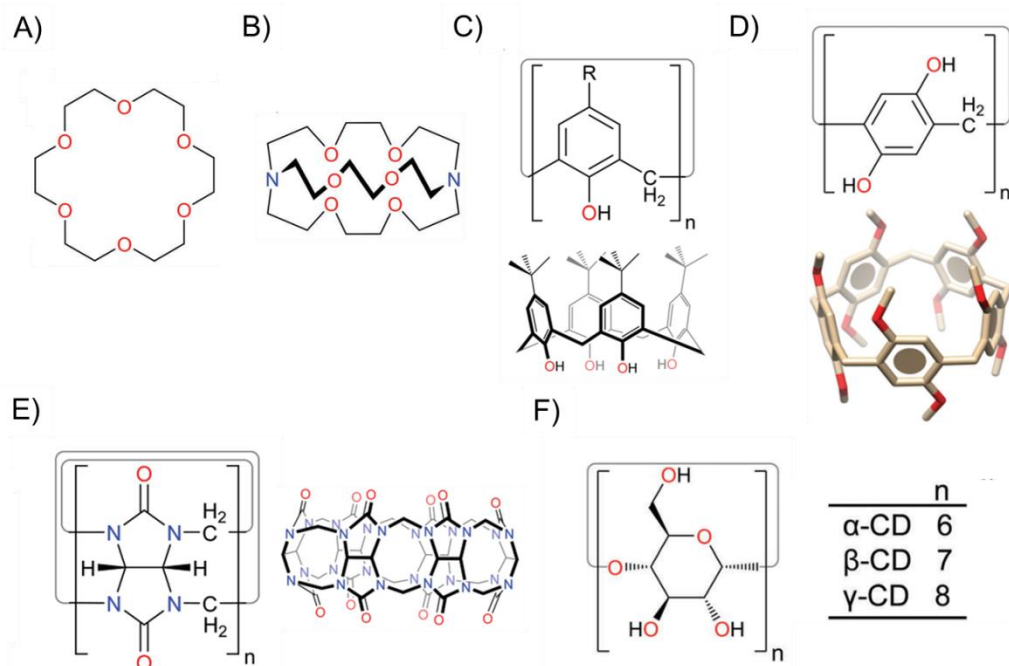


Figure 1.7. Chemical structure of A) crown ethers, B) criptands, C) calixarens, D) pillarenes; e) cucurbiturils and F) cyclodextrins. Adapted from reference 29.

Calix[n]arenes are calix-shaped supramolecular hosts resulting from the condensation of formaldehyde and *p*-substituted phenol units, which are linked by methylene bridges in the final cyclic structure. In a similar fashion, pillar[n]arenes can also be prepared, where their methylene-bridged 1,4-hydroquinone units make the host present a cylindrical section instead of a conical shape. Both types of systems have size-tunable π -electron-rich cavities capable to interact with aromatic molecules via π - π interactions as well as with ions and other polar guests through electrostatic interactions involving their external hydroxyl groups.²⁹ This allows the use of calix[n]arenes and pillar[n]arenes as supramolecular hosts in both aqueous and organic media.

Cyclodextrins (CDs) and cucurbit[n]urils (CBs, CB[n]s) are macrocyclic molecules composed of α -D-glucopyranoside and glycoluril groups, respectively, the size of the inner cavity of which can also be tuned upon variation of the number of monomer repeating units. The former present a truncated-cone structure, while the latter exhibit pumpkin-like shape. In contrast to calix[n]arenes and pillar[n]arenes, CDs and CBs are noncyclophanic hosts that cannot interact with molecular guests via π - π interactions. Instead, their complexes are mainly formed based on hydrophobic effects, often in combination with electrostatic interactions (e.g. hydrogen bonding, ion-dipole

interactions) with their external hydroxyl or carbonyl groups. This restricts their use to the recognition and capture of hydrophobic organic molecules in aqueous media. Although extremely stable supramolecular complexes can be formed with CBs, cyclodextrins are cheaper (and commercially available), more soluble in water and easier to functionalize. For these reasons, they were the supramolecular hosts of choice in this work. Accordingly, their properties will be further discussed in Chapter 3.

1.2.2.- Combined use of gold nanoparticles and supramolecular hosts

As mentioned above, this thesis pursues the enhancement of the plasmon-based activity of Au NPs by means of supramolecular chemistry, for which the surfaces of these nanostructures have been functionalized with cyclodextrin derivatives. Several precedents of the combined use of gold nanoparticles and supramolecular hosts for various applications can be found in the literature.³¹ In most of these precedents, cyclodextrins were also employed, and they will be reviewed in detail in Chapter 3. However, the use of other families of supramolecular hosts has also been reported, as illustrated by the examples described below.

For instance, Maity *et al.* reported the colorimetric detection of mercury (II) in aqueous media mediated by Au NPs functionalized with a dithiocarbamate calixarene derivative (DTCC-AuNPs).³² Addition of the metal ion into a colloidal dispersion of Au NPs caused a color change from pinkish-red to violet-blue, indicating that Au NP assembly was taking place via supramolecular host-guest interactions between Hg^{2+} and the calixarene moieties of distinct Au NPs. In addition, such detection could be achieved selectively with almost no interference coming from other metal cations (Figure 1.8).

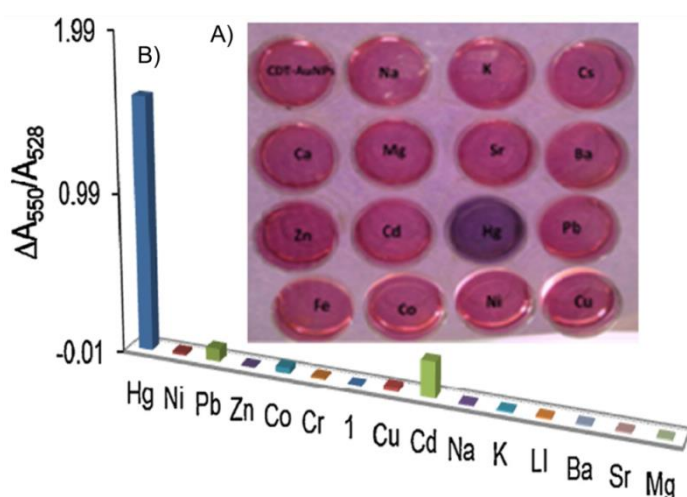


Figure 1.8. Photographic images of DTCC-AuNPs (3.2 nM) in presence of various metal ions (100 μM) in 10.0 mM HEPES buffer (pH 6.8). B) Bar diagram obtained from UV-vis spectral changes of DTCC-AuNPs (3.2 nM), expressed in terms of ratio of change of absorption intensity (A_{550}/A_{528}), after addition of various metal ions (100 μM).

In another example pillar[n]arenes Wang *et al.* reported the formation of a drug delivery system consisting in mesoporous silica NPs gated with carboxylatopillar[5]arene-functionalized Au NPs (CP5-AuNPs, Figure 1.9).³³ Upon addition of a suitable guest competitor CP5-AuNPs are displaced from the system and previously loaded Rhodamine B molecules can be delivered. This process could also be achieved by thermal heating, which caused the supramolecular interaction between CP5-AuNPs and Rhodamine B to be weakened, delivering these molecules to the surrounding medium.

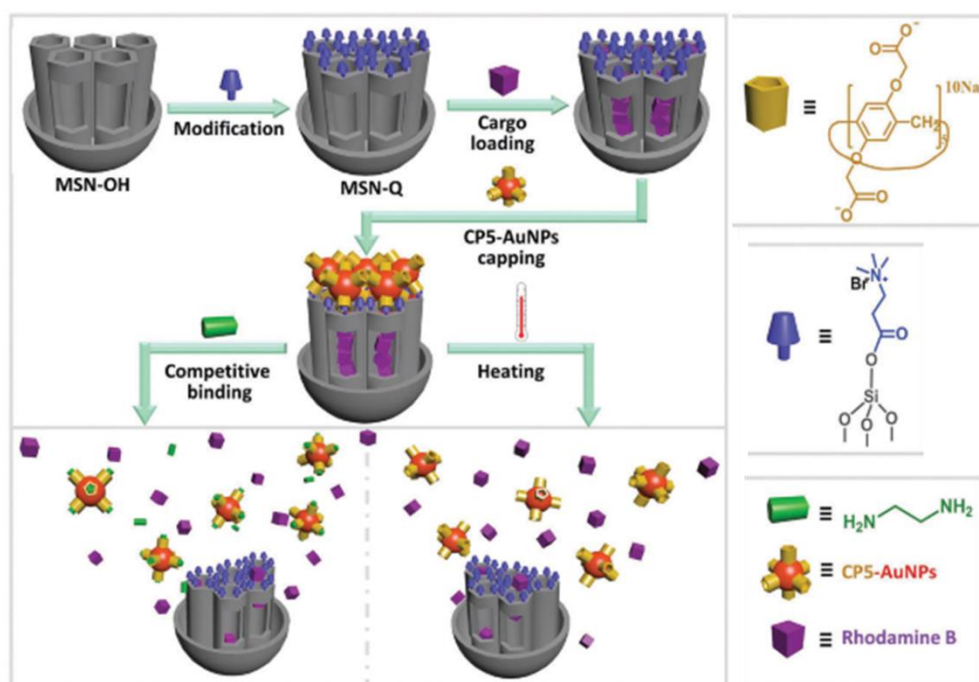


Figure 1.9. Schematic illustration of the Rhodamine B (RhB)-loaded, AuNPs-capped mesoporous silica nanoparticles (MSN) nanosystem, and their controlled release mechanism in response to competitive binding and temperature variations.

The last example presented herein refers to the use of cucurbit[n]urils () and Au NPs for the construction of a SERS-nanoreactor. Taylor *et al.* performed the photochemical isomerization or dimerization of (*E*)-4,4'-diaminostilbene (DAS) to obtain the corresponding *Z* isomer and the tetrasubstituted cyclobutane (*syn*-DAS) inside the appropriate cucurbit[n]uril member (CB[7] or CB[8]) located at the interface of Au NPs (Figure 1.10). They could monitor the extent of the reaction using time-resolved SERS.

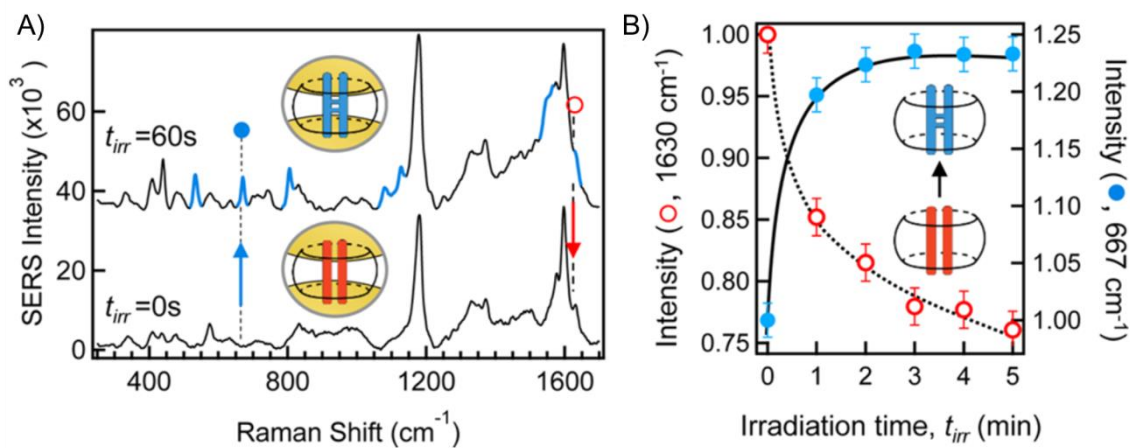


Figure 1.10. A) SERS spectra of DAS c CB[8]:Au NP nanocluster solution before ($t = 60$ s) UV irradiation ($\lambda = 355$ nm). Highlighted modes (blue, $t_{irr} = 0$ s) and after ($t_{irr} = 60$ s) indicate newly emergent modes following photocyclisation. Spectra offset and background subtracted for clarity. B) Time-resolved normalized SERS intensity of the 1630 cm^{-1} alkene mode of the DAS “reactant” (○) and of the 667 cm^{-1} cyclic mode of the syn-TCB photocycleproduct (●)

1.3.- BIBLIOGRAPHY

- [1] Cao, G. *Nanostructures and Nanomaterials. Synthesis, Properties and Applications*. London, Imperial College Press, **2004**.
- [2] Roduner, E. *Chem. Soc. Rev.* **2006**, 35, 583.
- [3] Gong, N.; Chen, S.; Jin, S.; Zhang, J.; Wang, P. C.; Liang, X-J *Regen. Biomat.* **2015**, 2, 273.
- [4] Burda, C.; Chen, X.; Narayana, R.; El-Sayed, M. A. *Chem. Rev.* **2005**, 105, 1025.
- [5] Daniel, M.-C.; Astruc, D. *Chem. Rev.* **2004**, 104, 293.
- [6] Love, J. C.; Estroff, L. A.; Kriebel, J. K.; Nuzzo, R. G.; Whitesides, G. M. *Chem. Rev.* **2005**, 105, 1103.
- [7] Sepúlveda, B.; Angelomé, P. C.; Lechuga, L. M.; Liz-Marzán, L. M. *Nano Today*, **2009**, 4, 244.
- [8] Huang, X.; Jain, P. K.; El-Sayed, I. H. *Lasers Med. Sci.* **2008**, 23, 217.
- [9] Thompson, D. T. *Nano Today*, **2007**, 2, 40.
- [10] <https://www.ancient.eu/image/4842/>
- [11] Biswas, A.; Wuang, T.; Biris, A. P. *Nanoscale* **2010**, 2, 1560.
- [12] Kelly, K. L.; Coronado, E.; Zhao, L. L.; Schatz, G. C. *J. Phys. Chem. B.* **2003**, 107, 668-677.
- [13] Saha, K.; Agasti, S. S.; Kim, C.; Li, X.; Rotello, V. M. *Chem. Rev.* **2012**, 112, 2739.
- [14] Wang, P.; Lin, Z.; Su, X.; Tang, Z. *Nano Today* **2017**, 12, 64.
- [15] Rosi, N. L.; Mirkin, C. A. *Chem. Rev.* **2005**, 105, 1547.
- [16] Qu, L.-L.; Li, D.-W.; Qin, L.-X.; Mu, J.; Fossey, J. S.; Long, Y.-T. *Anal. Chem.* **2013**, 85, 9549.
- [17] Anger, P.; Bharadwaj, P.; Novotny, L. *Phys. Rev. Lett.* **2006**, 96, 113002.
- [18] Chen, J.; Jin, Y.; Fahrudin, N.; Zhao, J. X. *Langmuir* **2013**, 29, 1584.
- [19] Ribeiro, T.; Baleizão, C.; Farinha, J. P. S. *Scientific Reports* **2017**, 7, 2440.
- [20] Bek, A.; Jansen, R.; Ringler, M.; Mayilo, S.; Klar, T. A.; Feldmann, J. *Nano Lett.* **2008**, 485.
- [21] Chen, A.; De Prince III, A. E.; Demortière, A.; Joshi-Imre, A.; Shevshenko, E. V.; Gray, S. K.; Welp, U.; Vlasko-Vlasov, V. K. *Small* **2011**, 7, 2365.
- [22] Li, A.; Srivastava, S. K.; Abdulhalim, I.; Li, S. *Nanoscale* **2016**, 8, 15658.
- [23] Cai, W.; Gao, T.; Hong, H.; Sun, J.; *Nanotechnol. Sci. Appl.* **2008**, 17.
- [24] Baffou, G.; Quidant, R. *Chem. Soc. Rev.* **2014**, 43, 3898.
- [25] Fasciani, C.; Bueno-Alejo, J. C.; Grenier, M.; Netto-Ferreira, J. C.; Scaiano, J. C. *Org. Lett.* **2011**, 13, 204.

- [26] Norman, R. S.; Stone, J. W.; Gole, A.; Murphy, C. J.; Sabo-Attwood, T. L. *Nano Lett.* **2008**, 8, 302-306.
- [27] Tong, L.; Zhao, Y.; Huff, T. B.; Hansen, M. N.; Wei, A.; Cheng, J.-X. *Adv. Mater.* **2007**, 19, 3136-3141.
- [28] Fan, W.; Leung, M. K. H. *Molecules* **2016**, 21, 180.
- [29] Liu, Z.; Nalluri, S. K. M.; J. F. Stoddart *Chem. Soc. Rev.* **2017**, 46, 2459.
- [30] Dietrich, B.; Lehn, J. M.; Sauvage, J. P. *Tett. Lett.* **1969**, 10, 2885.
- [31] Li, H.; Wang, Y.-W. *Chinese Chem. Lett.* **2013**, 24, 545.
- [32] Wang, X.; Tan, L.-L.; Li, X.; Song, N.; Li, Z.; Hu, J.-N.; Cheng, Y.-M.; Waag, Y.; Yang, Y.-W. *Chem. Commun.* **2016**, 52, 13775.

Chapter 2:

Objectives



As described in Chapter 1, nanosized materials have opened new avenues in chemistry (and other areas) and they are revolutionizing several fields of research due to their special properties which differ from those of bulk materials. This is the case of gold nanoparticles, the plasmon-based optical properties of which hold high promise for a wide range of applications. In most of them, Au NPs must couple together or interact with other species, which eventually requires ensuring short separation distances between these nanostructures and molecular compounds. Supramolecular chemistry appears as a powerful tool to accomplish this goal by providing selective and reversible control over the assembly of nanometer-size components via noncovalent interactions. Accordingly, *this thesis explores the use of supramolecular host-guest chemistry to enhance the plasmonic activity of Au NPs, ultimately aiming at developing new nanomaterials with improved properties.* To reach this goal, the following objectives have been pursued:

Objective 1: Implementing in our research group robust and versatile methods for the preparation of gold nanoparticles functionalized with cyclodextrins, the family of supramolecular hosts of choice in this work. These methods should allow fine control of the size of the final nanoparticles, while enabling incorporation of different types of cyclodextrin derivatives onto their surface. The results obtained in this area are shown in Chapter 3.

Objective 2: The development of a novel strategy for plasmon-based Au NP photocatalysis, where enhanced efficiency should result from the formation of reversible supramolecular host-guest complexes with reactant molecules onto the surface of the nanoparticles (Figure 2.1). To validate this approach, both uni- and bimolecular organic reactions have been assayed using cyclodextrin-functionalized Au NPs as photocatalysts, as described in Chapter 4.

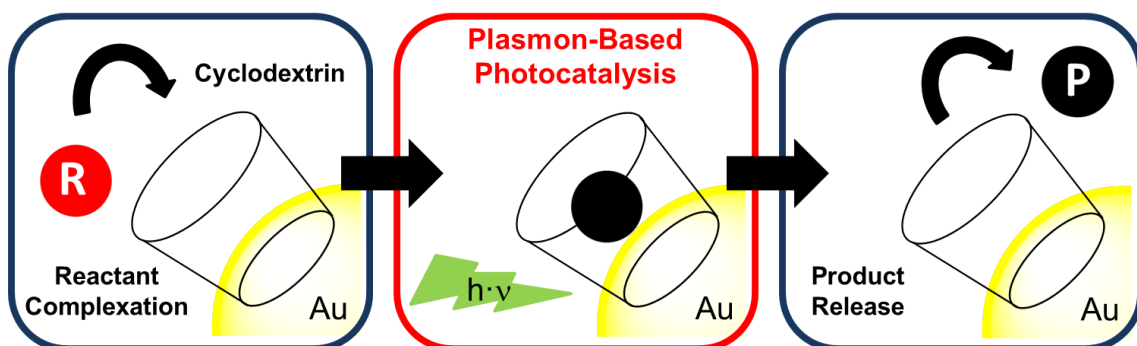


Figure 2.1. Schematic representation of the supramolecular strategy for enhancing the photocatalytic activity of Au NPs.

Objective 3: The development of a new methodology to attain reversible light-controllable heteroaggregation of Au NPs, thus generating smart nanomaterials that could eventually be applied in plasmon-enhanced spectroscopies. With this aim, gold nanoparticles have been decorated with photoresponsive ligands, the supramolecular interaction of which with cyclodextrin-coated Au NPs could be modulated upon illumination, as shown in Figure 2.2. The results obtained when exploring this objective are discussed in Chapter 5.

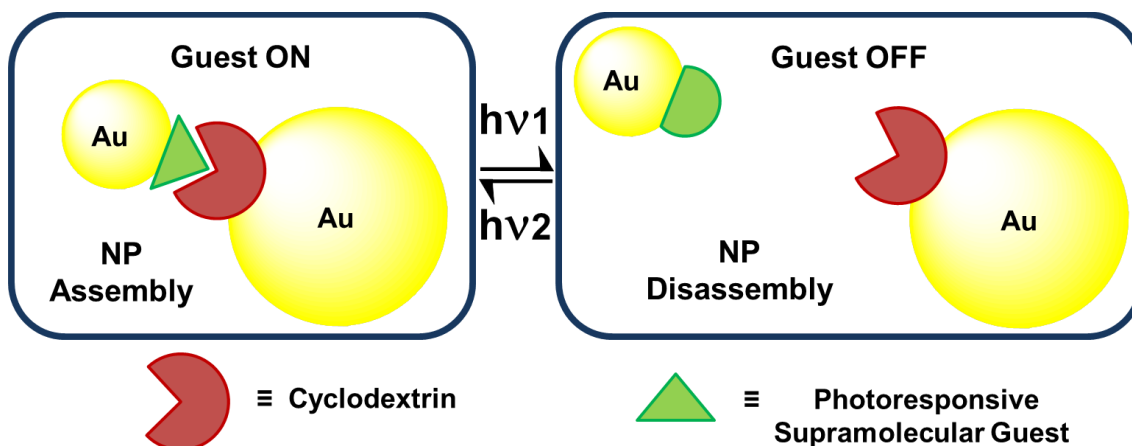


Figure 2.2. Schematic representation of light-controllable assembly and disassembly of Au NPs driven by supramolecular host-guest interactions.

Chapter 3:

Synthesis and Characterization of Host-Functionalized Gold Nanoparticles

3.1- INTRODUCTION

As commented in chapters 1 and 2, this thesis aims at the preparation of new photofunctional materials based on host-functionalized gold nanoparticles by combining supramolecular chemistry and the plasmonic properties of Au NPs. In particular, our interest specially focuses on the preparation of such systems for their application in photocatalysis and photoactive smart materials. In the proposed materials, the role of supramolecular hosts must be twofold: on the one hand, they should enable molecular recognition and reversible molecular assembly to take place on the surface of Au NPs; on the other hand, they should ensure nanoparticle colloidal stabilization. As such, the supramolecular hosts of choice have to fulfill some requirements. First of all, they have to be water soluble and display hydrophobic effect-driven supramolecular complexation, maximizing then the amount of associated guest molecules in aqueous media. Secondly, they must present low to moderate supramolecular association constants with a large number of organic molecules, allowing for reversible complexation of a wide variety of molecular guests. Finally, they have to be easy to functionalize as to prepare appropriate thiolated derivatives, enabling their anchoring to the surface of Au NPs by means of the formation of relatively strong Au-S bonds. Such modification is crucial to assure a proper stabilization of the final Au NPs that in some cases will be submitted to rather harsh conditions. According to these requirements it was decided to use the cyclodextrin family of supramolecular hosts along this thesis, which will be introduced in the following section.

3.1.1- Cyclodextrins, the family of supramolecular hosts of choice

Cyclodextrins are a class of natural cyclic oligosaccharides consisting in D-glucose units linked by α -1,4-glycosidic bonds. They were discovered in 1891 and are obtained by the enzymatic degradation of starch.¹ There are three main types of CDs depending on the number of D-glucose units that form the macrocycle: α -cyclodextrin (α -CD, 6 glucose units), β -cyclodextrin (β -CD, 7 glucose units) and γ -cyclodextrin (γ -CD, 8 glucose units), as shown in Figure 3.1A. All of them present a three-dimensional barrel-type structure with a truncated cone shape, which creates an accessible inner cavity that can accommodate other molecular species (Figure 3.1C). Table 3.1 shows the dimensions of the cavity of CDs.

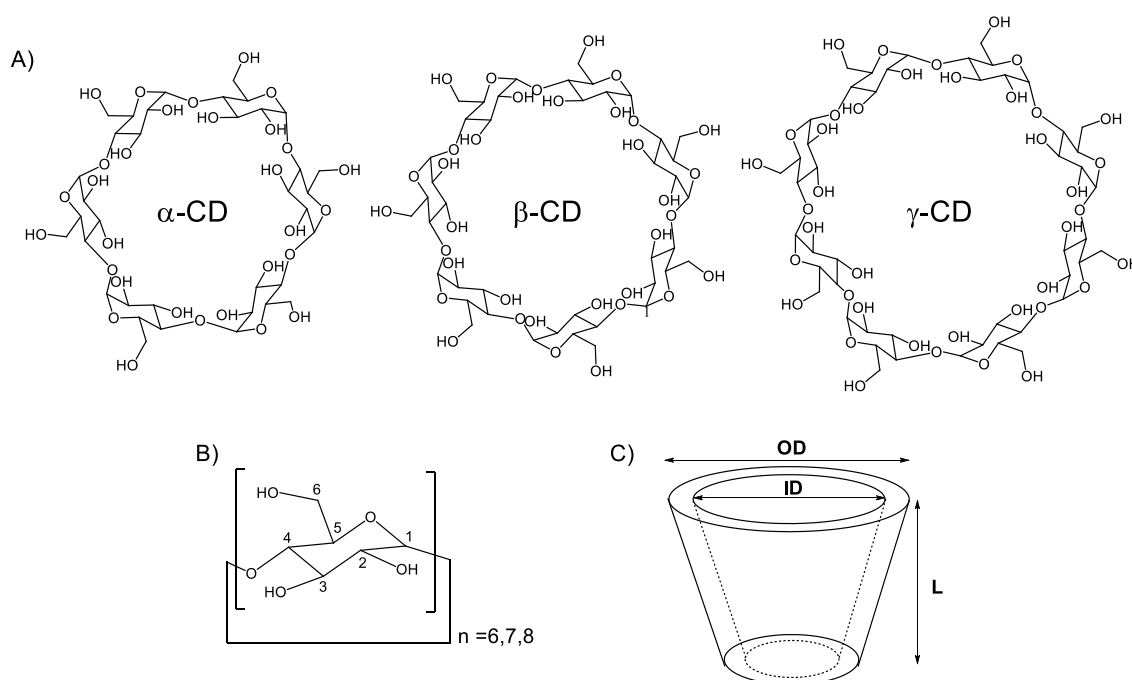


Figure 3.1. (A) Chemical structure of the three main types of CDs. (B) General structure of cyclodextrins. (C) Schematics of the 3-dimensional cone-like structure of CDs.

The chemical structure of CDs makes them strong amphiphilic molecules. Their inner cavity is hydrophobic due to the presence of the glycosidic bonds in it. By contrast, the exterior surface of CDs is highly hydrophilic due to the presence of the hydroxyl groups of the glucose units. In particular, the narrower rim is covered by the C6 primary hydroxyls, whereas the wider rim is covered by the C2 and C3 secondary hydroxyls.

Table 3.1. Geometrical and solubility properties of the different types of CDs.¹

	α -CD	β -CD	γ -CD
Inner Diameter (ID) / nm	0.47-0.53	0.60-0.65	0.75-0.83
Outer Diameter (OD) / nm	1.46 ± 0.1	1.54 ± 0.5	1.75 ± 0.5
Height (L) / nm	0.79	0.79	0.79
Solubility in water / g·100 mL⁻¹	14.5	1.85	23.2

Owing to their particular geometry and chemical nature, CDs have a good capability to associate with a variety of inorganic/organic molecules and ions in both aqueous solution and the solid state to form supramolecular host-guest inclusion complexes.² In most of the cases, these complexes present low to moderate association constants ($K_a < 10^{-4}$), and they are promoted by two main types of supramolecular interactions: (i) hydrophobic effects between CD inner cavity and the lipophylic component of the guest; (ii) ion-dipole and/or dipole-dipole interactions involving the external hydroxyl groups of the host.³ In addition to their supramolecular behavior, CDs possess other interesting properties which made them suitable candidates for the purposes of this thesis: they are commercially available at low prices and non-toxic, and more importantly, they present good water solubility (Table 3.1) and are easy to functionalize.

CDs are also attractive to us because they have already been used in applications similar to those pursued in this thesis. On the one hand, they have been profusely applied as molecular templates in some photochemical reactions involving both unimolecular and bimolecular processes in the absence of Au NPs.^{4,5,6} In addition, CDs are well-known building blocks for the preparation of 2D and 3D supramolecular structures due to their ability to self-assemble in multiple ways. Actually, several architectures can be achieved with different CD derivatives and the proper molecular hosts, such as pseudo-polyrotaxanes, polyrotaxanes, nanotubes and nanowires, and hydrogels, among others.² Finally, the functionalization of gold surfaces and, more specially, gold nanoparticles with CD derivatives have also been reported for the fabrication of functional materials, as next discussed.

3.1.2- Cyclodextrin-functionalized gold nanoparticles

As commented in chapter 1, the combined use of supramolecular hosts and Au NPs has given rise to the development of new functional materials with new or improved properties in numerous fields. Owing to the aforementioned properties that have been described in the previous section, CDs have played a key role in this development, as illustrated by the following examples in the medical and the analytical fields. Applications related to Au NP photocatalysis and Au NP assembly will be described in detail in chapter 4 and chapter 5 respectively.

There are plenty of examples in the literature describing the potential application of CD-modified Au NPs in the medical field. For instance, Park *et al.* reported a sophisticated system for the release of the anti-cancer drug β -laphacone.⁷

Three different ligands were attached to the surface of the NP: anti-epidermal growth factor receptor (anti-EGFR) antibodies as targeting moiety, polyethylene glycol (PEG) as antifouling agent and thiol-modified β -CDs as drug carrier. When these NPs entered the cells, reduction of thiol bonds took place and the β -CD: β -laphacone inclusion complexes were released, a process that was found to occur in a larger extent in tumoral cells displaying high glutathione concentrations. In another example Aykaç *et al.* reported the formation of Au NPs decorated with β -CD and lactose, capable to be recognized by different cell receptors and to deliver the anticancer drug methotrexate (MTX) (Figure 3.2).⁸

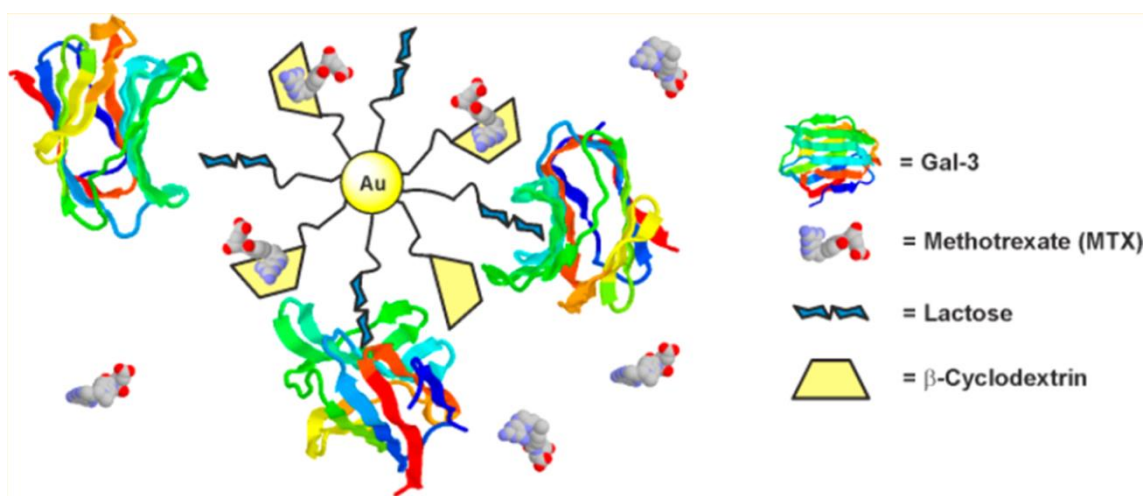


Figure 3.2. Schematic representation of CD-modified Au NPs bearing lactose as recognizing unit for the delivery of the anticancer drug methotrexate (MTX). Reproduced from reference 8.

Cyclodextrins have also been extensively applied in the analytical field. For instance, Yang *et al* reported the enantioseparation of diverse drugs and aminoacids using CD-modified Au NPs in pseudostationary phase-capillary electrophoresis, owing to the distinct association between both esteroisomers with the CD hosts.⁹ Alternatively, Li, et al. were able to detect α - and β - naphthol isomers with a detection method based on dye-incorporated CD-functionalized Au NPs.¹⁰ This method relies on the quenching of emission of the incorporated dye by energy transfer (ET) to the naphthol molecule upon analyte complexation by CD-modified Au NPs (Figure 3.3) With this method naphthol could be detected down to 8 and 50 nM concentration for the α - and the β - isomer respectively.

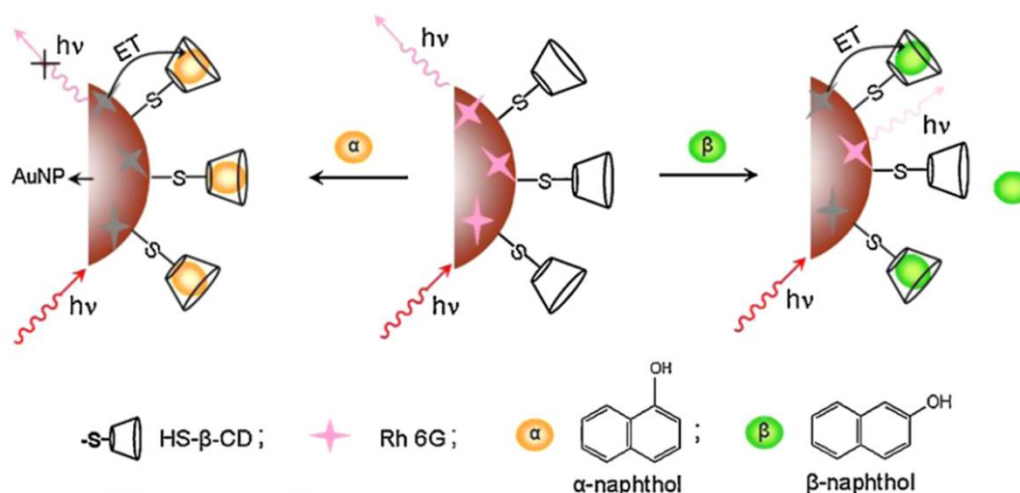


Figure 3.3. Schematic representation of recognition and detection of naphthol isomers by the CD-modified Au NPs incorporating the Rhodamine 6G dye (Rh 6G).

3.1.3- Objectives: preparation of cyclodextrin-functionalized gold nanoparticles

The first step towards the different objectives targeted in this thesis has been the preparation of suitable gold nanoparticles functionalized with cyclodextrins. Accordingly, this chapter aims at describing in detail the synthesis of such nanostructures, the application of which as photofunctional materials will be subsequently discussed in chapters 4 and 5. It must be noted that Au NPs of different sizes and coated with CDs bearing inner cavities of varying dimensions had to be considered along this work depending on their final use. For this reason, we have pursued in this thesis the synthesis of Au NPs with diameters ranging from few to tens of nanometers and functionalized with α -CD, β -CD and γ -CD derivatives. As outlined in Figure 3.4, this has involved two main steps that are described in the next sections: (i) the thio-derivatization of pristine α -CD, β -CD and γ -CD to facilitate chemisorption onto the surface of Au NPs via Au-S bond formation; and (ii) the preparation of Au NPs decorated with such CD derivatives.

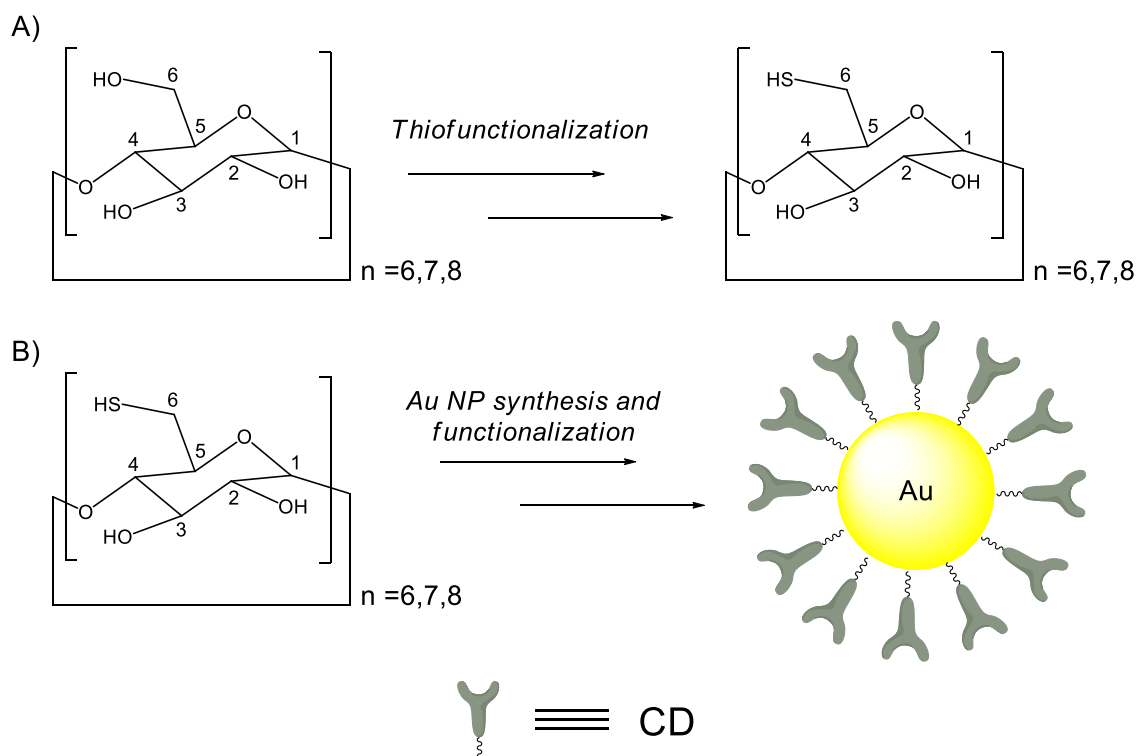


Figure 3.4. A) Thiofunctionalization of CD supramolecular hosts. B) Synthesis and functionalization of Au NPs with thiolated ligands.

3.2- PREPARATION OF THIOLATED CYCLODEXTRIN DERIVATIVES

CD derivatives were already synthesized during the 90's and a wide number of derivatives are currently being exploited in numerous fields.¹¹ Since this work aimed at the functionalization of Au NPs with cyclodextrins via Au-S bond formation, the derivatives of interest were those where one or all C6 primary hydroxyls had been exchanged by thiol functions. As can be seen in Figure 3.5, four different derivatives were prepared. First, our attention focused on β -CD, which we wanted to exploit for enhancing the photocatalytic activity of Au NPs in unimolecular reactions (see chapter 4). For this supramolecular host, both their heptathioloated (β -CD-(SH)₇) and monothioloated (β -CD-(SH)₁) derivatives were prepared. Next, perthiolation of α - and γ -CD at their C6 position to yield α -CD-(SH)₆ and γ -CD-(SH)₈ were also conducted to expand our photocatalytic studies to bimolecular reactions (see chapter 4) and attempt the fabrication of smart Au NP heteroaggregates (see chapter 5).

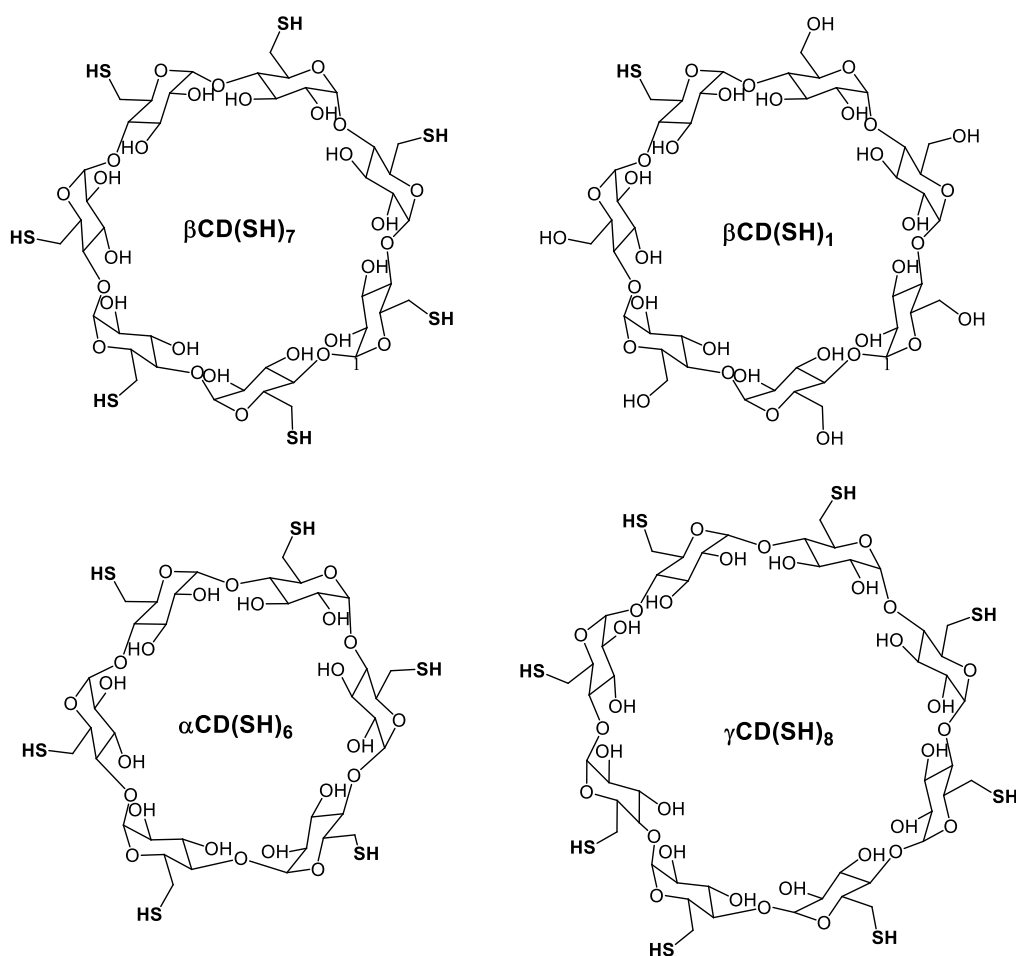


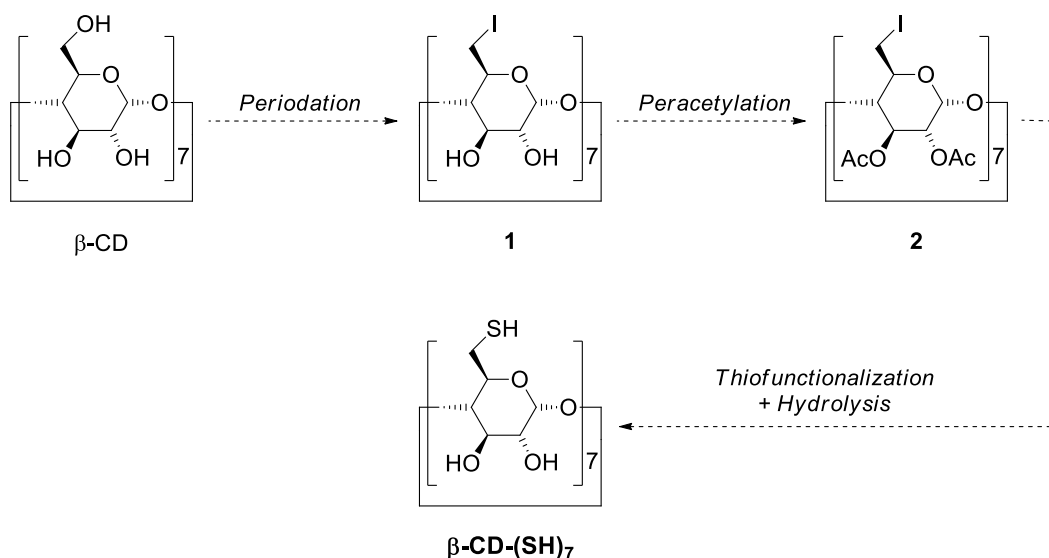
Figure 3.5. Chemical structures of the four cyclodextrin derivatives prepared in the present thesis.

3.2.1- Perthiolation vs monothiolation of β -CD: a case study

In the literature both the perthiolation¹² and monothiolation^{13,14} of pristine β -CD at its C6 position have already been described. The resulting CD derivatives differ in the number of anchoring groups to gold surfaces, which must influence the properties and functionality of the coating layer of supramolecular hosts subsequently created around Au NPs. Starting from β -CD-(SH)₇, more stiff and stable layers should be formed, which may however hinder supramolecular interaction with molecular guests. By contrast, more flexible and reactive layers might result from β -CD-(SH)₁, though at the expense of dramatically reducing their stability. For these reasons, both types of cyclodextrin derivatives were prepared and comparatively assayed for the preparation and application of CD-functionalized Au NPs.

(a) Synthesis of β -CD-(SH)₇

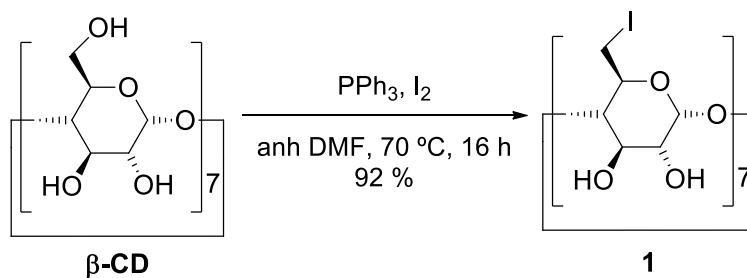
β -CD-(SH)₇ was prepared from commercially available β -CD according to a previously reported procedure to which some modifications were introduced.^{12,15} Scheme 3.1 shows the synthetic pathway followed towards the synthesis of this product.



Scheme 3.1. Synthetic route for the preparation of β -CD-(SH)₇.

The very first step of this synthetic route involves the selective substitution of all the primary hydroxyls in β -CD by iodine atoms, which benefits from the higher reactivity

of these groups with respect to the CD secondary -OH moieties at C2 and C3 positions. Scheme 3.2 summarizes the reaction conditions and the results obtained for this step, where iodation was accomplished with high yield by using iodine and triphenylphosphine in anhydrous DMF. The reaction proceeded via formation of an iodotriphenylphosphonium iodide intermediate, which was attacked by the primary hydroxyls of β -CD to form the corresponding oxyphosphonium leaving group. Then, nucleophilic substitution took place by iodide ions to afford **1**, which was characterized by ^1H and ^{13}C NMR spectroscopies and high-resolution mass spectrometry (HRMS) in agreement with reported data.¹² It must be noted that, by contrast to typical organic reactions, ^1H NMR is not the best suited technique to monitor the functionalization of CDs due to the appearance of several broad OH resonances throughout the spectrum. Instead, ^{13}C NMR provides a better insight into the chemical derivatization of CDs, since clear shifts of the narrow signals of the ^{13}C nuclei are normally observed. To illustrate this behavior, Figure 3.3 at the end of this section compares the ^{13}C NMR spectra of the starting material, product **β -CD-(SH)₇** and intermediates **1** and **2**, where it can be observed that replacement of the primary -OH groups of β -CD by iodine atoms in **1** dramatically shifted upfield the C6 signal from $\delta = 59.9$ ppm to 9.5 ppm.

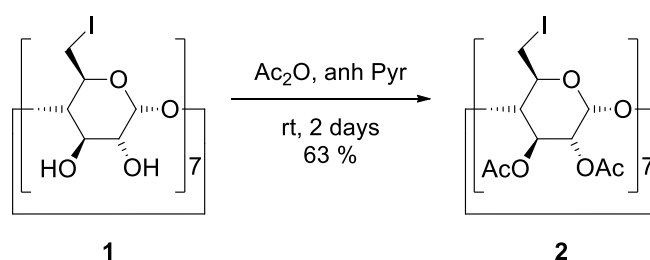


Scheme 3.2. Periodation of β -CD.

It is important to emphasize that the synthesis of **1** from β -CD is extremely sensitive to humidity, since the iodotriphenylphosphonium iodide intermediate hydrolyzes in the presence of water. This leads to incomplete substitution of the primary hydroxyl groups, causing the final product not to precipitate during the work-up of the reaction mixture. To avoid this situation, β -CD was oven-dried for 24 h prior to its use to fully remove all hydration and/or complexed water molecules. Another problem encountered for this reaction was the purification of the periodated product. Soxhlet extraction of **1** in methanol as reported in the literature¹² did not provide a completely pure compound, since the brown color of the solid obtained evidenced the presence of a significant amount of iodine, which might form a stable inclusion complex with the

cyclodextrin derivative. Because of that, successive digestions of **1** in dichloromethane were further carried out, since regular purification by flash column chromatography was not possible due to the high polarity of the molecule. Although the solid isolated in this way had the appearance of a white powder, concentrated solutions of this compound in water and DMSO turned to be brown-colored, thus indicating the presence of some residual iodine molecules. As a result, the yield determined for the reaction must be slightly overestimated and, worse still, a non-negligible amount of cyclodextrin-iodine complexes could be obtained at the end of the synthetic sequence that could affect the subsequent supramolecular experiments to be conducted with β -CD-(SH)₇ and β -CD-(SH)₇-coated Au NPs.

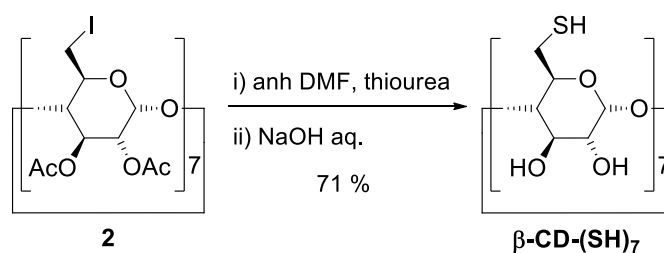
To circumvent this problem, we did not proceed to obtain β -CD-(SH)₇ directly from **1** as most authors report.¹² Instead, inspired by the procedures described for the preparation of the analogous compound γ -CD-(SH)₈,¹⁵ the synthesis of derivative **2** was undertaken with 63 % yield (Scheme 3.3). In this case, peracetylation of the C2 and C3 secondary -OH groups of **1** with acetic anhydride in pyridine decreased the polarity of the CD derivative, thus allowing the purification of **2** to be performed by flash column chromatography for removing all the residual iodine molecules. The formation of this compound was demonstrated by ¹H NMR and ¹³C NMR spectroscopies and HRMS. In particular, in the case of the ¹³C NMR spectrum shown in Figure 3.6, the signal at δ = 8.1 ppm arising from the C6 nuclei bonded to iodine atoms was still observed, while new resonances at δ = 170.69 and 169.46 ppm corresponding to the new acetate groups introduced appeared.



Scheme 3.3. Peracetylation of **1**.

As shown in Scheme 3.4, the final step for the synthesis of β -CD-(SH)₇ involved the substitution of the iodine atoms by thiol groups via the formation of an isothiuronium salt, which upon treatment in basic conditions with aqueous NaOH and further acidification with KHSO₄ provided the target compound in 71 % yield. It must be noticed that basic hydrolysis of the C2 and C3 ester groups of **2** took place

simultaneously, which implies that peracetylation of **1** to improve the purity of the final product only introduced one additional reaction step to the synthetic route. This compound was characterized by ^1H and ^{13}C NMR spectroscopies and HRMS in agreement with reported data.¹² Figure 3.3 shows the ^{13}C NMR spectra of $\beta\text{-CD-(SH)}_7$, where the down field shift of the C6 signal from $\delta < 10$ ppm for iodated intermediates **1** and **2** to $\delta = 26.0$ ppm for the final product clearly proves the replacement of the iodine atoms by thiol groups. Therefore, $\beta\text{-CD-(SH)}_7$ was successfully prepared from commercial $\beta\text{-CD}$ via three steps and an overall 41 % yield.



Scheme 3.4. Perthiolation and acetate hydrolysis of **2** for the obtention of $\beta\text{-CD-(SH)}_7$.

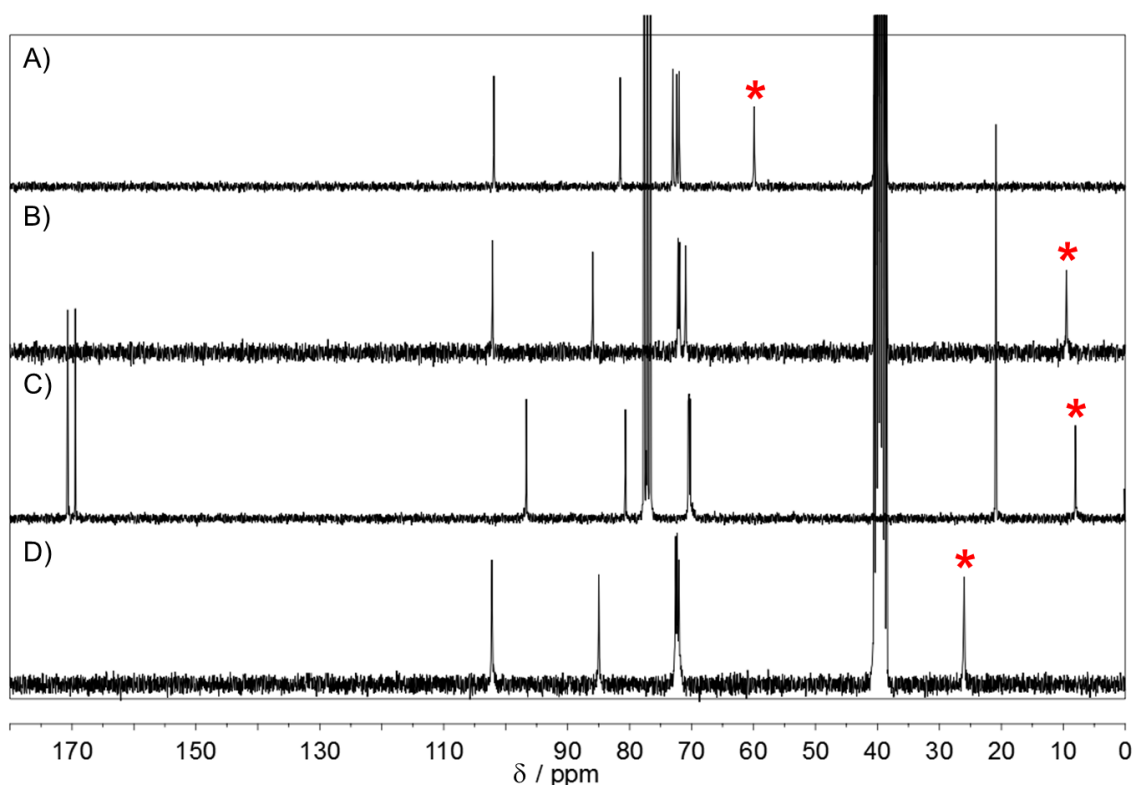
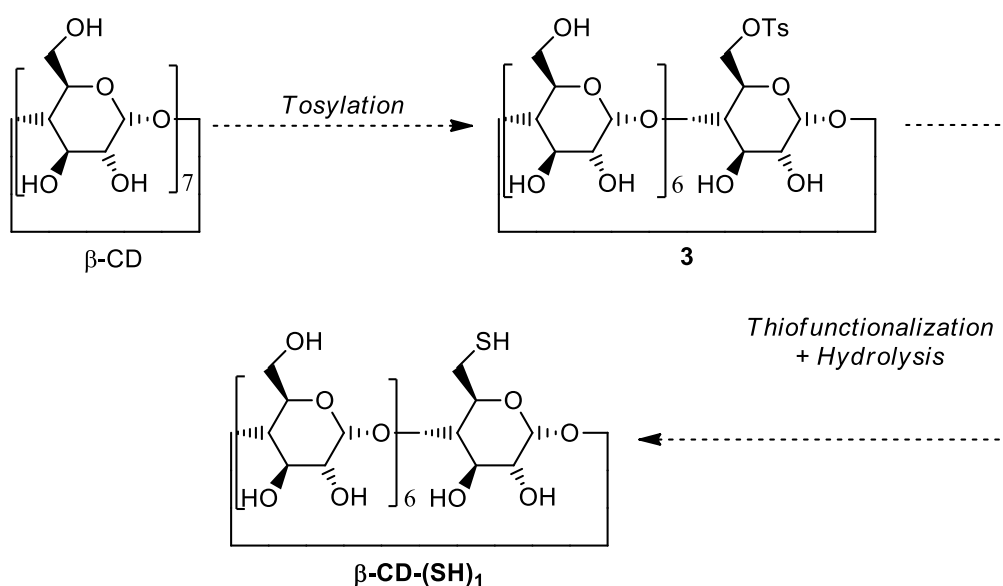


Figure 3.6. Comparison of the ^{13}C NMR spectra (250 MHz, $\text{DMSO-}d_6$, CDCl_3) of A) pristine $\beta\text{-CD}$. B) periodated derivative **2**. C) peracetylated derivative **3** and D) $\beta\text{-CD-(SH)}_7$. The red stars

indicate the location of the C6 signal, which shifts downfield upon iodine substitution and then upfield when the thiol function is incorporated.

(b) Synthesis of $\beta\text{-CD-(SH)}_1$

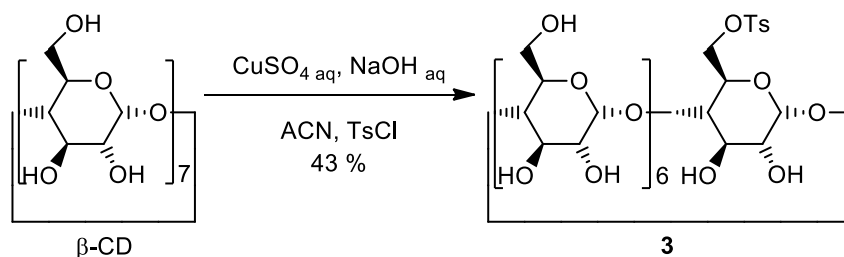
$\beta\text{-CD-(SH)}_1$ was prepared from commercially available $\beta\text{-CD}$ according to previously reported procedures.^{13,14} Scheme 3.5 shows the synthetic pathway followed for the preparation of this monothiolated $\beta\text{-CD}$ derivative.



Scheme 3.5. Synthetic pathway towards the preparation of $\beta\text{-CD-(SH)}_1$.

Scheme 3.6 shows the results obtained in the first step towards the synthesis of $\beta\text{-CD-(SH)}_1$, which involved the tosylation of one of the primary hydroxyl groups of $\beta\text{-CD}$ with *p*-toluenesulfonyl chloride in the presence of Cu(II) and basic conditions. This modification made the -OH moiety a better leaving group for the second step of the synthesis. The regioselective monotosylation of $\beta\text{-CD}$ achieved under these reaction conditions relied on two main aspects: (i) the coordinating properties of Cu(II), which promoted the formation of $\beta\text{-CD}$ dimers through the C2 and C3 secondary hydroxyls, thus blocking one side of the cyclodextrin torus and favoring reaction on its primary face;¹³ **Error! Marcador no definido.** and (ii) the size of the tosylate group, which prevented the reaction of other primary hydroxyl groups due to steric hindrance. Actually, it has been observed that the use of other reactants leads to persubstitution of

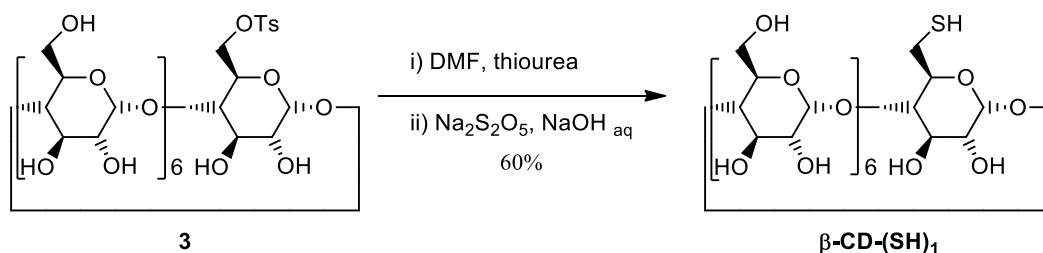
the primary hydroxyl groups (as in the synthesis of β -CD-(SH)₇), while the absence of Cu(II) in the reaction medium lowers the yield down to 11%.⁹



Scheme 3.6. Monotosylation of β -CD.

Compound **3** was characterized by means of ¹H and ¹³C NMR spectroscopies and HRMS. It must be noted that the ¹H and ¹³C NMR spectra of **3** were much more complex than those of the starting materials, as expected due to the loss of symmetry of β -CD upon partial derivatization. From the integrals of the ¹H NMR signals corresponding to the tosylate and hydroxyl groups as well as HRMS data, major formation of monotosylated product **3** was corroborated in agreement with reported data.¹⁴ Because of the high polarity of these CD derivatives, **3** could not be purified by flash column chromatography unless previous acetylation of the free -OH groups was performed, as shown before for the synthesis of β -CD-(SH)₇. In this case, however, this procedure was not applied and compound **3** was used without further purification.

The last step in the synthesis of β -CD-(SH)₁ involved the reaction of **3** with thiourea to form the corresponding isothiuronium salt, which upon posterior treatment with aqueous NaOH/Na₂S₂O₅ hydrolyzed to yield the target monothiolated CD derivative, as shown in scheme 3.7. In contrast to the synthesis of β -CD-(SH)₇, where precipitation of the desired compound took place spontaneously upon acidification, the precipitation of the more water-soluble β -CD-(SH)₁ compound required the use of an external agent to occur. Trichloroethylene was employed in this case, since its inclusion into the CD cavity enhances its hydrophobicity and promotes its precipitation in aqueous medium. The resulting solid was characterized by means of ¹H and ¹³C NMR spectroscopies and HRMS, corroborating the formation of the desired product by comparison with reported data.¹⁴ Therefore, β -CD-(SH)₁ was successfully prepared from commercial β -CD via two steps and an overall 20 % yield.

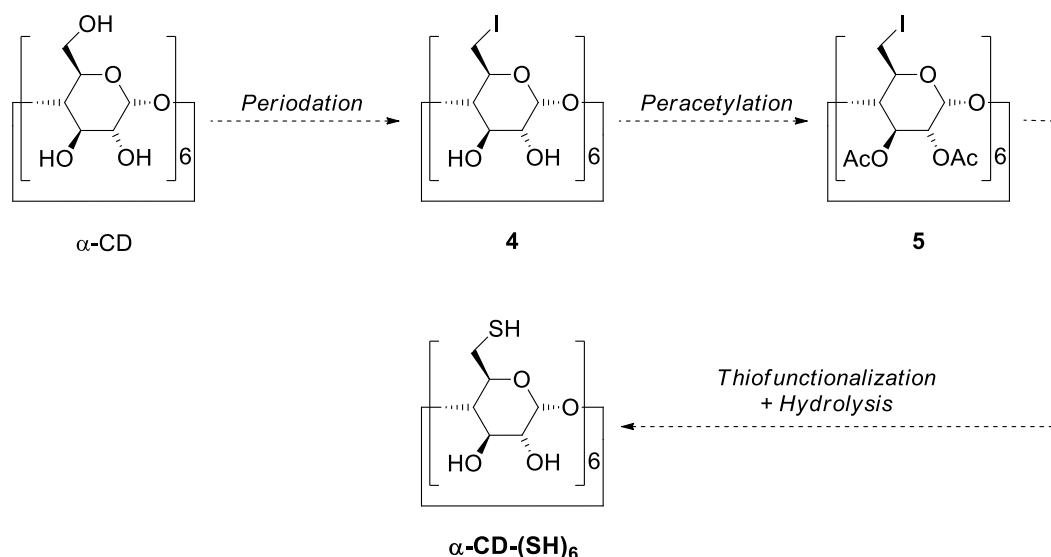


Scheme 3.7. Monothiolation of **3** to yield target product **$\beta\text{-CD-(SH)}_1$** .

With thiolated derivatives **$\beta\text{-CD-(SH)}_1$** and **$\beta\text{-CD-(SH)}_7$** in our hands, the corresponding CD-coated Au NPs were prepared and characterized. Preliminary experiments on those nanostructures demonstrated that **$\beta\text{-CD-(SH)}_1$** -functionalized Au NPs presented very low thermal and photochemical stability (see section 3.3.2 for further details), which made us abandon the use of the monothiolated derivative of β -CD. For this reason, when attempting the thioderivatization of α - and γ -CD, we directly focused our efforts on the preparation of the perthiolated **$\alpha\text{-CD-(SH)}_6$** and **$\gamma\text{-CD-(SH)}_8$** compounds.

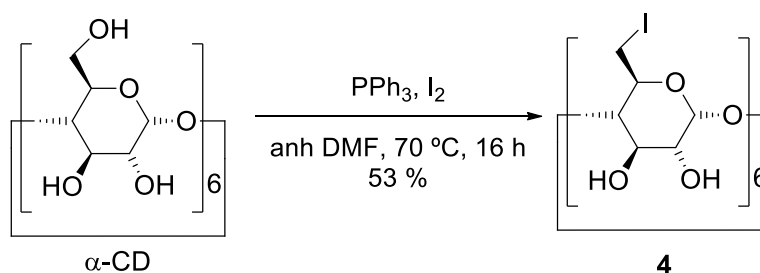
3.2.2- Perthiolation of α -CD: synthesis of **$\alpha\text{-CD-(SH)}_6$**

The corresponding perthiolated derivative of α -CD was synthesized following the very same procedure described in the previous section for the preparation of **$\beta\text{-CD-(SH)}_7$** . As shown in Scheme 3.8, periodation of the starting material was followed by the peracetylation step required to obtain an iodine-free α -CD derivative and, finally, the thiol functionalities were introduced and the acetate groups removed to afford **$\alpha\text{-CD-(SH)}_6$** .

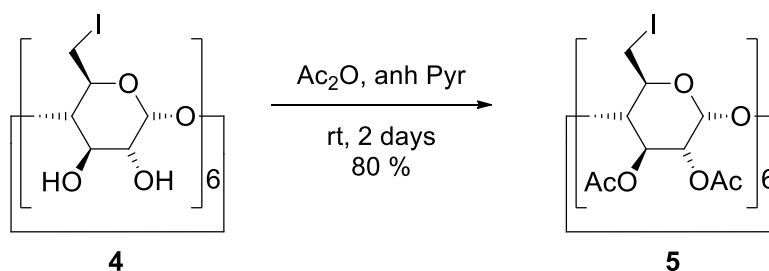


Scheme 3.8. Synthetic route for the preparation of α -CD-(SH)₆.

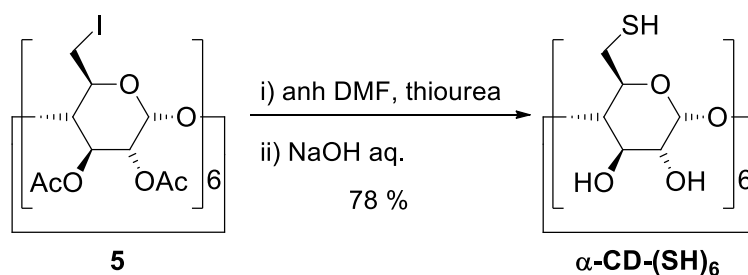
Even though α -CD and β -CD were expected to behave in the same way in terms of reactivity, the yield obtained in the first step of the synthetic sequence when preparing the periodated derivative **4** (55 %, Scheme 3.9) was significantly lower than that accomplished for **1** under the same conditions (92 %). In addition, different supramolecular interaction of the product obtained with the excess of molecular iodine used in this reaction was also observed. Thus, whereas 2-3 days were necessary in the case of **1** to eliminate most of the remaining I₂ by Soxhlet extraction in methanol, 5 days were not sufficient for **4**. This evidenced the higher affinity of α -CD derivatives towards molecular iodine than β -CDs, probably due to better size complementary between the guest and the inner cavity of the host. This result is in accordance with previous studies on the association between CDs and I₂.^{16,17} Digestion of **4** in hot methanol allowed removing a larger fraction of the excess of iodine, but still, the color of the final solid was by far darker than that of the 7-member analogue **1**, thereby indicating a larger presence of residual I₂ in the final product. In spite of this, the ¹H and ¹³C NMR and HRMS spectral data of the solid isolated corroborated the formation of **4**.

Scheme 3.9. Periodation of $\alpha\text{-CD}$.

Because of the large supramolecular affinity of **4** towards I_2 , peracetylation of this intermediate appeared crucial in order to remove all residual molecular iodine. Accordingly, **4** was submitted to the acetylation conditions already employed for the synthesis of $\beta\text{-CD-(SH)}_7$, which resulted in the formation of **5** with 80 % yield (Scheme 3.10). After purification by flash column chromatography, an iodine-free white solid could be obtained that was successfully identified by ^1H and ^{13}C NMR spectroscopies and HRMS.

Scheme 3.10. Peracetylation of **4**.

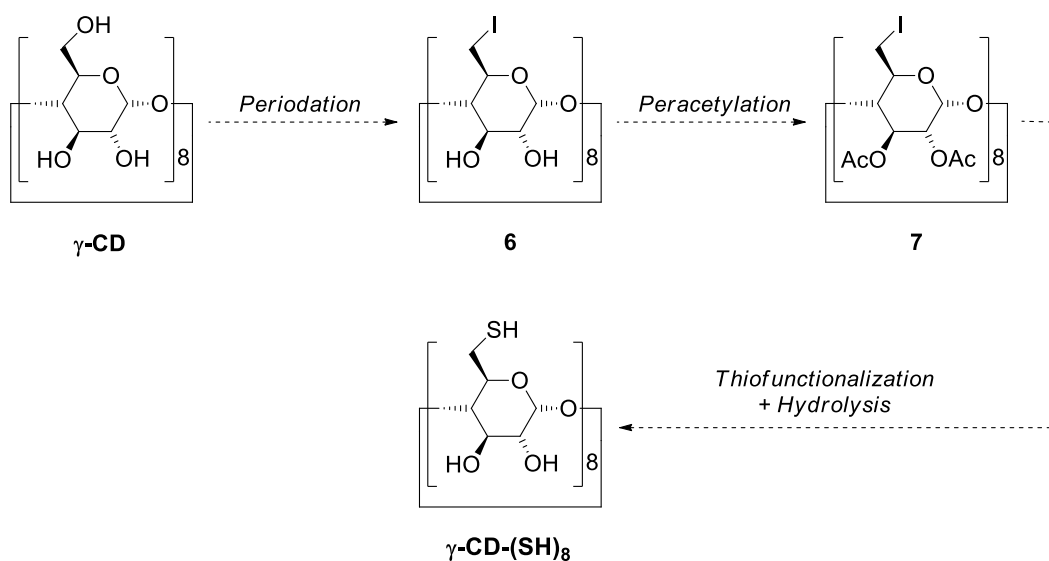
The final step in the preparation of $\alpha\text{-CD-(SH)}_6$ involved the formation of the isothiuronium salt derived from the reaction of **5** with thiourea, which was subsequently hydrolyzed in aqueous basic conditions to provide the desired perthiolated derivative of $\alpha\text{-CD}$ by simultaneous deprotection of the acetate groups. As shown in Scheme 3.11, this process took place in 78 % yield. The resulting product was characterized by ^1H and ^{13}C NMR spectroscopies and HRMS, and unambiguously identified as the target compound. Therefore, $\alpha\text{-CD-(SH)}_6$ was prepared from commercial $\alpha\text{-CD}$ via three steps and an overall 33 % yield.



Scheme 3.11. Perthiolation and acetate hydrolysis of **5** to obtain target product $\alpha\text{-CD-(SH)}_6$.

3.2.3- Perthiolation of $\gamma\text{-CD}$: synthesis of $\gamma\text{-CD-(SH)}_8$

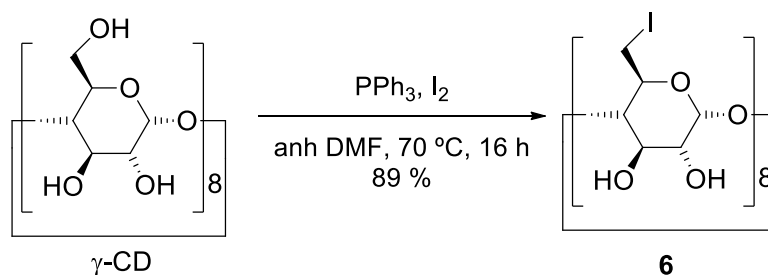
In analogy to the syntheses described for $\beta\text{-CD-(SH)}_7$ and $\alpha\text{-CD-(SH)}_6$ in the previous sections, the preparation of $\gamma\text{-CD-(SH)}_8$ from pristine $\gamma\text{-CD}$ was attempted through the same sequence involving the periodation, peracetylation and thiofunctionalization steps (Scheme 3.12).



Scheme 3.12. Synthetic strategy for the preparation of $\gamma\text{-CD-(SH)}_8$.

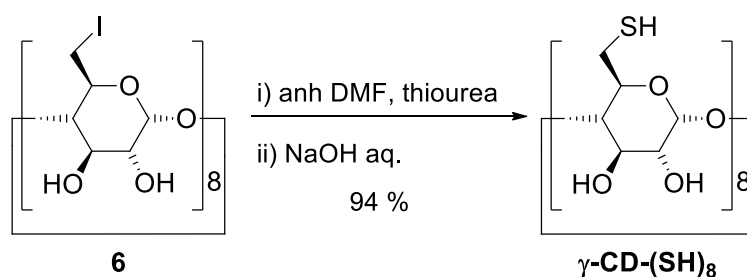
The first periodation step worked perfectly well for native $\gamma\text{-CD}$, as shown in Scheme 3.13. A significantly higher yield (89 %) was obtained in comparison with $\alpha\text{-CD}$ (53 %) and, more importantly, Soxhlet extraction in methanol for just 48 h seemed to efficiently remove all residual excess of molecular iodine. Actually, the solid obtained after this purification process had an off-white color that was preserved after dissolution and it was successfully identified as intermediate **6** based on NMR data. On the one

hand, this demonstrated that γ -CD derivatives poorly supramolecularly interact with I_2 , probably due to their large cavity, as expected from previously obtained results with α - and β -CD which are in accordance with literature reports.^{16,17} On the other hand, this made the planned peracetylation step for further removing residual iodine unnecessary and, as such, periodated compound **6** was directly converted into γ -CD-(SH)₈.



Scheme 3.13. Periodation of γ -CD.

Therefore, the second, and in this case final, step of the synthetic route was the thiofunctionalization of **6** to provide the target product γ -CD-(SH)₈. Surprisingly this step was accomplished with a 94 % yield, a value that significantly exceeded those obtained for the analogous β - and α -CD derivatives (Scheme 3.14). The white solid obtained was characterized by ¹H and ¹³C NMR spectroscopies and HRMS. Therefore, γ -CD-(SH)₈ could be obtained in two steps with an overall 84 % yield.



Scheme 3.14. Thiofunctionalization and hydrolysis of **6** to achieve γ -CD-(SH)₈.

3.3- SYNTHESIS AND CHARACTERIZATION OF CYCLODEXTRIN-FUNCTIONALIZED GOLD NANOPARTICLES

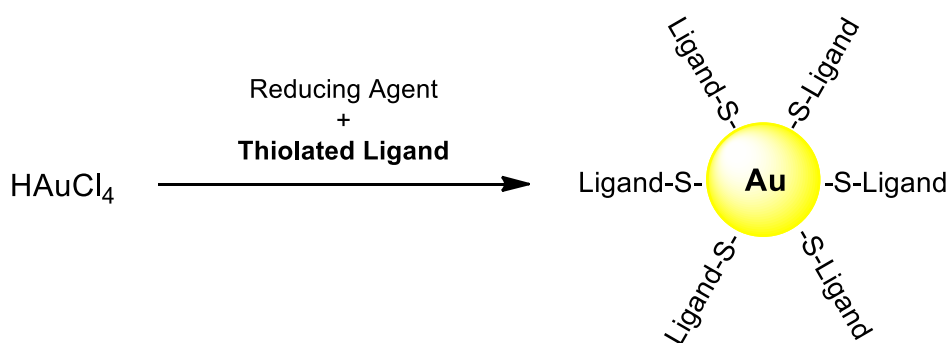
As commented in chapter 1, Au NPs were first prepared in ancient times, and they were mainly responsible of the ruby-red color in colored glasses (e.g. in stained-glass windows in medieval churches). Such color appeared after the thermal treatment of the glass precursors containing metal salts, which caused some reductive processes through which Au NPs were formed and trapped inside the glass matrix. From these precedents, one may think that two conditions are mainly necessary for the preparation of Au NPs: (i) the reduction of a gold precursor, and (ii) to avoid the formation of bulk metal by stabilizing the NPs formed. Actually, the methodologies employed in this thesis for the preparation of liquid colloids of gold nanoparticles have been based in this bottom-up strategy, for which the following common elements were used: commercially available tetrachloroauric (III) acid as a gold precursor, a chemical reducing agent and a stabilizing ligand. Mixing these different components in an appropriate solvent (in our case, water or DMSO) at suitable conditions results in the formation of a supersaturated solution of gold metal atoms, which leads to the nucleation of gold clusters and their subsequent growth into the final Au NPs.

In what regards to the functionalization of Au NPs with the desired ligands (in our case, thiolated cyclodextrin derivatives), there are different procedures available. These procedures can be classified as direct and indirect methodologies depending on whether the thiolated stabilizing ligand is present at the moment of the reduction of the gold salt, or by contrary, it is incorporated after the reduction has taken place and Au NPs have already been formed. Both types of methodologies were explored in this thesis, since they allow the preparation of functional Au colloids of different properties. For simplicity, β -CD-(SH)₇ and, in a minor extent, β -CD-(SH)₁ were chosen as the model thiolated ligands in these exploratory studies, although any other thiolated CD derivative could have been used for such purpose.

3.3.1- Direct synthesis of cyclodextrin-functionalized gold nanoparticles

The direct synthesis of thiol-stabilized Au NPs consists in the reduction of HAuCl₄ in the presence of the desired stabilizer and an appropriate reducing agent, as depicted in Scheme 3.15. There are two main methodologies reported in the literature to achieve this goal. One of them was first described by Brust and Schiffrin, consisting

in a two phase wet chemical synthesis typically using toluene and water as solvents, sodium borohydride as a reducing agent, and a quaternary ammonium salt as a phase transfer catalyst.¹⁸ This methodology is normally applied when the final Au NPs are expected to be dispersible in apolar organic solvents due to the hydrophobic nature of the thiolated ligand of choice, and it is only able to provide small particles with up to ~5 nm in diameter.¹⁸

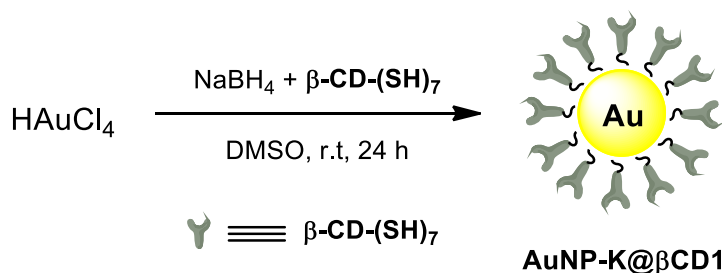


Scheme 3.15. Direct synthesis of thiol-stabilized Au NPs.

On the other hand, when the final Au NPs are to be redispersed in aqueous media, even if the thiolated ligand used is only moderately soluble in water, the procedure described by Kaifer is normally applied.¹⁹ Since water-dispersible Au NPs are required for the applications aimed all along this thesis, Kaifer's method was used here for the preparation of gold nanoparticles coated with $\beta\text{-CD-(SH)}_7$.

(a) Preparation of $\beta\text{-CD-(SH)}_7$ -coated Au NPs by Kaifer's method (AuNP-K@ βCD1)

As can be seen in Scheme 3.16, Kaifer's method for the preparation of thiolated Au NPs is carried out in rather mild conditions and lasts for 24 h. In a typical synthesis, a solution of the desired thiol is dissolved in DMSO together with the reducing agent (in our case, $\beta\text{-CD-(SH)}_7$ and NaBH_4 , respectively). Then, this solution must be quickly mixed with another DMSO solution containing the gold precursor. The reaction is almost instantaneous as evidenced by the rapid color change of the mixture from light yellow to deep brown-red; however, the mixture must be stirred for 24 h, during which time the thiolated monolayer on the surface of the nanoparticles is expected to be created, organized and well-packed.²⁰



Scheme 3.16. Preparation of **AuNP-K@βCD1** by Kaifer's method.

Interestingly, this procedure allows for a certain size tuning of the final particles by varying the initial concentration ratio of thiolated ligand and gold precursor ($r_{\text{CD}/\text{Au}}$). For this reason, a set of different **AuNP-K@βCD1** colloids were prepared for several distinct $r_{\text{CD}/\text{Au}}$ values (0.006-0.075), and they were next characterized by TEM and UV-vis absorption spectroscopy. As shown in Figure 3.5, two main effects were observed for the LSPR extinction band of the resulting NPs when decreasing $r_{\text{CD}/\text{Au}}$ from 0.75 down to 0.012: (i) it significantly red-shifted, and (ii) its extinction coefficient rose. These results are consistent with the increase of the size of **AuNP-K@βCD1** as $r_{\text{CD}/\text{Au}}$ diminishes, a conclusion that was confirmed by TEM analysis of two of the colloids prepared (Figure 3.6A-B). Thus, rather spherical nanoparticles with average diameters of 2.9 ± 0.9 and 4 ± 1 nm were obtained for $r_{\text{CD}/\text{Au}} = 0.075$ and 0.025, respectively. However, this is a limited strategy for size tuning since stabilization of the final colloid must become inefficient by further decreasing the amount of thiolated ligand molecules, which should lead to partial aggregation and/or coalescence of the final NPs. This seemed to be case for the sample prepared at $r_{\text{CD}/\text{Au}} = 0.006$, the LSPR band of which had lower intensity than expected and presented substantial spectral broadening compared to the other cases (Figure 3.7). Indeed, this was further corroborated by TEM measurements, where the formation of large aggregates of Au NPs could be observed (Figure 3.8C).

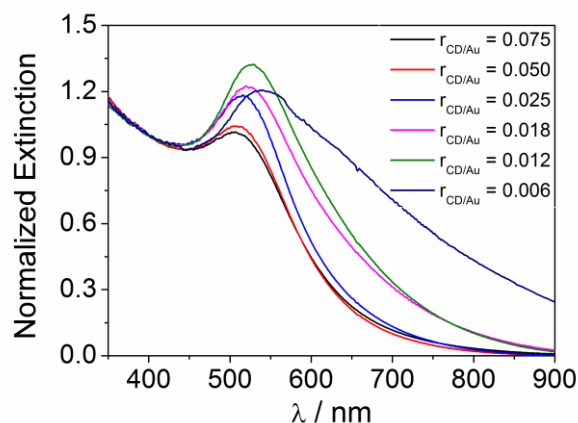


Figure 3.7. UV-Vis spectra of the synthesis of **AuNP-K@βCD1** using different **β-CD-(SH)₇/HAuCl₄** ($r_{\text{CD/Au}}$) molar ratios.

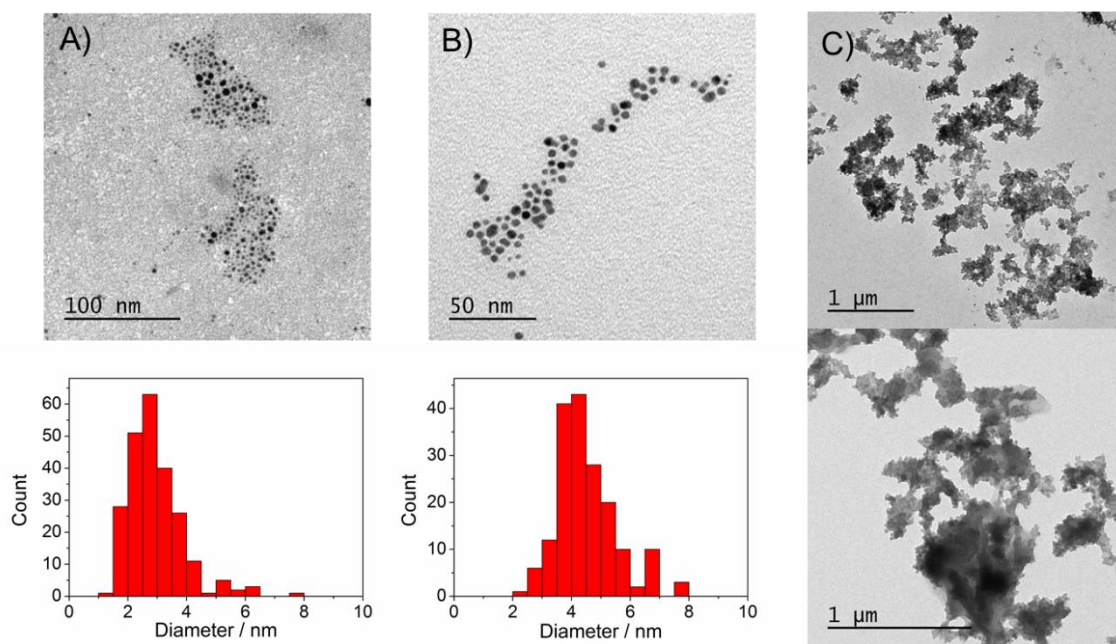


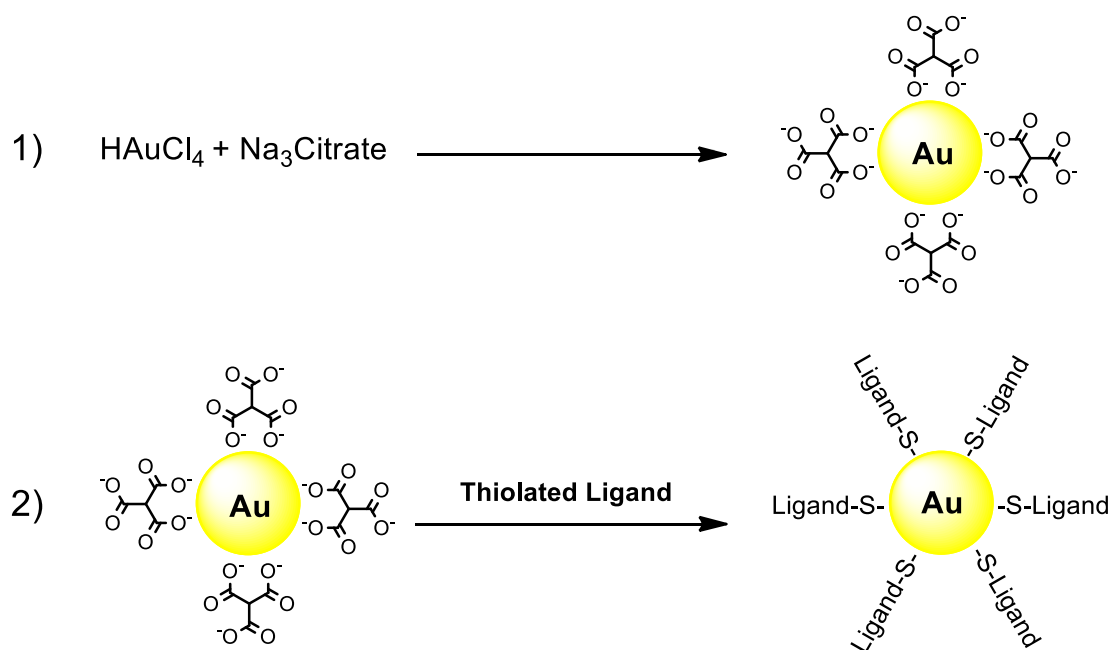
Figure 3.8. TEM images and histogram analyses of **AuNP-K@βCD1** corresponding to **β-CD-(SH)₇/HAuCl₄** molar ratios of A) 0.075 and B) 0.025. C) TEM images of **AuNP-K@βCD1** corresponding to a **β-CD-(SH)₇/HAuCl₄** molar ratio of 0.006.

Based on our results, Kaifer's method for the preparation of CD-coated Au NPs suffers from two drawbacks. First, large polydispersities were obtained for **AuNP-K@βCD1**, accounting for standard deviation of the size histograms determined being 25-30% of the average diameter of the nanoparticles (Figure 3.8A-B). More importantly, this method failed to produce surface-functionalized Au NPs with

diameters larger than 10 nm. Because of that, CD-coated Au NPs with bigger sizes had to be prepared by indirect methods.

3.3.2- Indirect synthesis of cyclodextrin-functionalized gold nanoparticles

Contrary to the direct synthesis of thiol-functionalized Au NPs, the indirect methods have two differentiated steps. First of all, Au NPs coated with labile stabilizers (in our case, citrate molecules) have to be prepared, and afterwards, a ligand exchange process has to be carried out to introduce the thiolated compounds of choice (Scheme 3.17). This ligand exchange step is mainly driven by the formation of rather strong Au-S bonds between Au NPs and the desired ligand with respect to the weaker interactions established with the initial stabilizer. In this way, different types of gold colloids functionalized with thiolated derivatives of β -CD were prepared, which mainly differed on the method employed for the preparation of the citrate-stabilized Au NPs.



Scheme 3.17. Synthetic two-step procedure for the preparation of thiol-stabilized Au NPs.

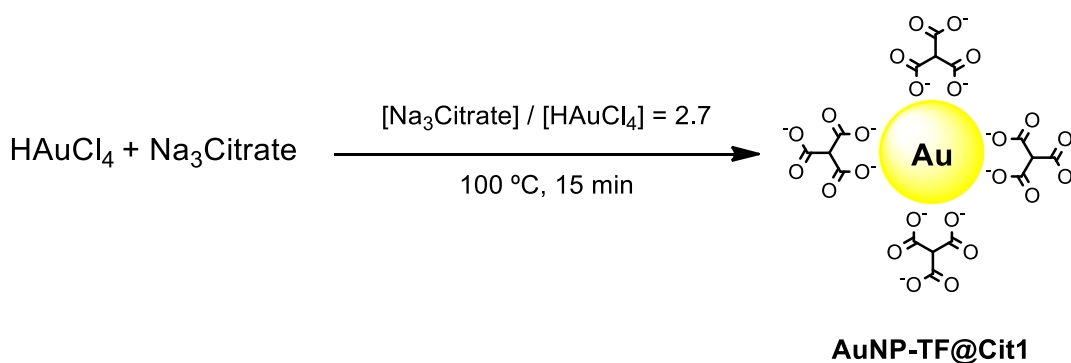
(a) Preparation of citrate-stabilized Au NPs: Turkevich-Frens method (AuNP-TF@Cit1)

In 1951 John Turkevich published a simple method for the synthesis of Au NPs, which relies on the chemical reduction of HAuCl_4 with sodium citrate in boiling aqueous

media.²¹ Within this methodology, citrate molecules do not only act as reducing agents, but also as stabilizers by weakly bind to the surface of the already formed Au NPs via electrostatic interactions. The negatively charged, physisorbed citrate molecules then avoid particle aggregation by electrostatic repulsion between nearby NPs. With this procedure, rather spherical Au NPs with an average diameter of ~20 nm are typically obtained.²² With respect to Kaifer's method, larger particles are formed in this case because of the use of: (i) a milder reductant (citrate instead of NaBH₄), which generates a less sudden supersaturation of Au⁰ atoms in the reaction mixture and, as such, a lower number of initial gold nuclei; (ii) a more labile stabilizer (citrate instead of organic sulfides), which favors nanoparticle growth afterwards.

Later on, Frens demonstrated that it was possible to tune the size of the final NPs obtained by simply varying the molar ratio between sodium citrate and the gold precursor ($r_{\text{Cit/Au}}$), thus allowing the preparation of AuNPs with diameters ranging from 10 – 150 nm.²³ However, by decreasing $r_{\text{Cit/Au}}$ with respect to Turkevich's original procedure, this method only produces good-quality NPs for diameters up to ~50 nm, and bigger nanoparticles are obtained at the expense of higher polydispersities. In addition, the final size, polydispersity and even morphology of the NPs prepared by means of the Turkevich-Frens method can be affected by many factors, such as pH, temperature and stirring velocity.²² For example, lowering the temperature leads to larger and more irregular nanoparticles.

As shown in Scheme 3.18, in this thesis the molar ratio between sodium citrate and HAuCl₄ was adjusted to 2.7. At such molar ratio, the NPs obtained presented a mean diameter ~15 nm.



Scheme 3.18. Preparation of **AuNP-TF@Cit1** by the Turkevich-Frens method.

For the obtention of **AuNP-TF@Cit1**, the proper amount of sodium citrate was added to a boiling solution of tetrachloroauric acid, which resulted in the reduction of the precursor and the formation of small gold metal clusters in a few seconds, as evidenced by the color change from yellow to blue-grey. This was followed by the rapid growth into larger particles, which led to the typical red-wine color of gold colloidal suspensions. Importantly, the initial solution was allowed to strongly boil with no reflux condenser prior to the addition of the reducing agent, in order to prevent the formation of temperature gradients that could have affected the polydispersity of the final colloid.²² As shown in Figure 3.9A, **AuNP-TF@Cit1** displayed a narrow LSPR band with a maximum extinction value centered at $\lambda = 521$ nm. TEM analysis of this sample revealed that indeed, the NPs obtained were rather spherical with a mean diameter of 15 ± 3 nm and a reasonably good polydispersity (Figure 3.9B-C).

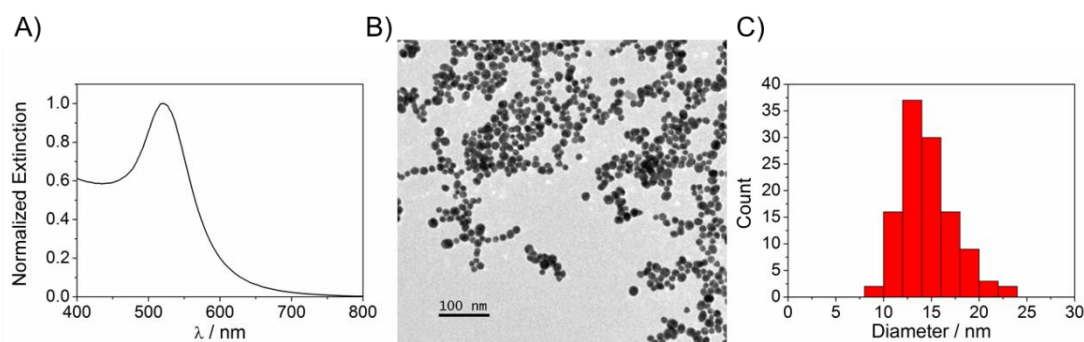


Figure 3.9. A) Extinction spectra, B) TEM image and C) size histogram of **AuNP-TF@Cit1** prepared by the Turkevich-Frens method with $r_{\text{Cit}/\text{Au}} = 2.7$.

Although this methodology fails to produce NPs with regular shapes and good polydispersities for diameters beyond 50 nm, an attempt to prepare **AuNP-TF@Cit2** of around 70 nm in diameter was carried out. However, NPs with an average diameter of 35 nm and presenting very irregular shapes were instead obtained (Figure 3.9). Because of this limitation, we explored an alternative methodology for the preparation good-quality bigger NPs: the seed-growth method.

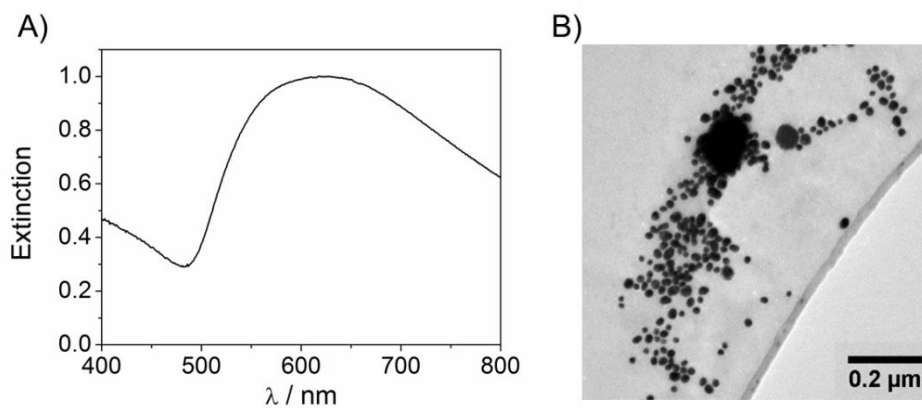
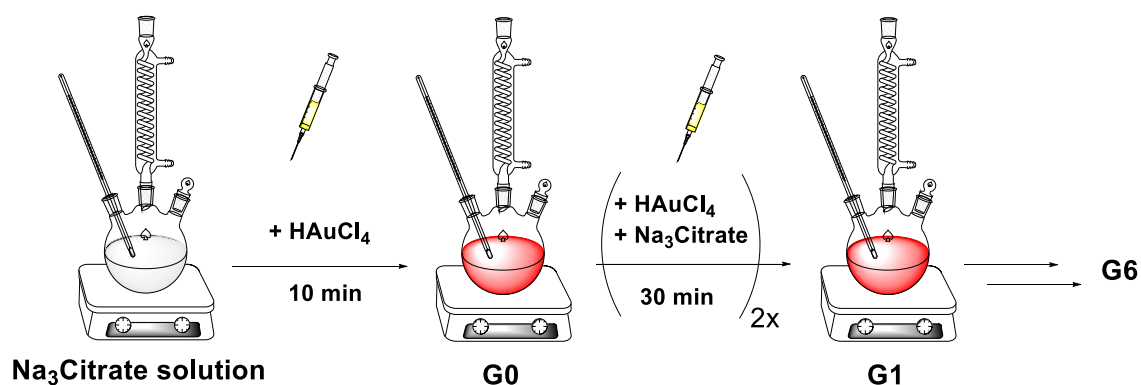


Figure 3.10. A) Extinction spectra in water and B) representative TEM image of **AuNP-TF@Cit2** prepared by the Turkevich-Frens method with $r_{\text{Cit}/\text{Au}} = 1$

(b) Preparation of citrate-stabilized Au NPs: seed-growth method (AuNP-Gn@Cit)

In the present work, the seed-growth methodology developed by Puntero *et al.* was applied, which allows the synthesis of size- and shape-controlled, large citrate-stabilized Au NPs.²⁴ As shown in Scheme 3.19, it consists in a multistep procedure, which starts with the preparation of small and monodispersed Au nuclei (seeds, **G0**), which are afterwards grown in short consecutive steps until reaching the desired size.



Scheme 3.19. Schematic representation of the synthetic procedure for the preparation of citrate-stabilized Au NPs followed in this work using the seed-growth method developed by Puntero *et al.*²⁴ See Chapter 7 for experimental details.

In each of these steps, HAuCl_4 and sodium citrate are used as gold precursor and reducing agent respectively, and their concentration and those of the growing seeds are controlled to warrant kinetic control of the growing process and to prevent secondary nucleation and Ostwald ripening processes. This should ensure a narrow

distribution of sizes for the final citrate-stabilized Au NPs, while the number of growth steps conducted controls the final size of the particles obtained. In our case, we aimed to obtain **AuNP-Gn@Cit** of about 80 nm in diameter, for which a total number of 6 growth steps of the initial seeds had to be performed (from G1 to G6).

For simplicity, the growing process of **AuNP-Gn@Cit** was monitored in situ by means of UV-vis absorption spectroscopy. In particular, Equation 3.1 was used to determine the diameter of **AuNP-Gn@Cit** obtained in each step from their LSPR extinction band, an expression that was derived to estimate the size of citrate-stabilized Au NPs ranging from 35 to 100 nm in diameter. In this equation, λ_{LSPR} is the wavelength of the maximum of the LSPR extinction band, λ_0 is 512 nm, and L1 and L2 are predefined parameters equal to 6.53 and 0.0216, respectively.²⁵

$$d = \frac{\ln\left(\frac{\lambda_{LSPR}-\lambda_0}{L_1}\right)}{L_2} \quad (3.1)$$

As shown in Figure 3.11, the LSPR extinction peak red-shifted and became more intense for each growing step, indicating that larger NPs were being obtained. Table 3.2 shows the sizes estimated for these nanoparticles according to Equation 3.1. For **AuNP-G6@Cit**, a diameter of 72 nm was determined and, accordingly, the synthesis was stopped after the 6th growth step.

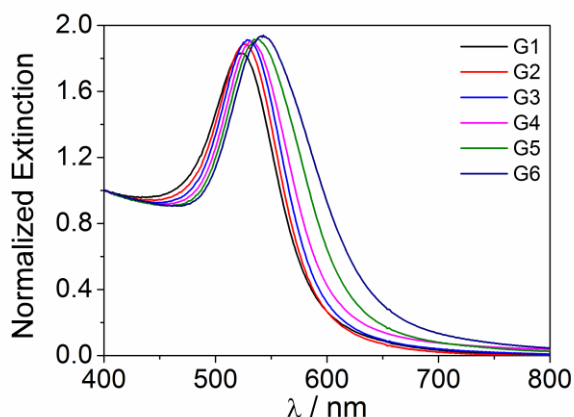


Figure 3.11. Extinction spectra in water of the different **AuNP-Gn@Cit** obtained after each growing step during the seed-growth method synthesis. All spectra are normalized at $\lambda = 400$ nm for better comparison.

UV-vis absorption measurements were next complemented with TEM analysis of selected batches of nanoparticles: **AuNP-G1@Cit**, **AuNP-G3@Cit** and **AuNP-G6@Cit**. As shown in Table 3.2 and Figure 3.10, reasonable agreement was found between the nanoparticle sizes determined by TEM and those estimated from Equation 3.1. More importantly, TEM measurements demonstrated that **AuNP-G6@Cit** was comprised by spherical nanoparticles having the desired size and good polydispersity,

thus proving the capacity of the seed-growth method used to provide large Au NPs of good quality. However, it must be noted that Puentes *et al.* reported a smaller size and better polydispersity for the particles obtained after 6 growth steps applying the very same methodology (54 ± 3 nm) and, actually, they needed up to 9 growth steps to achieve 80 nm-in-diameter Au NPs.²⁴ As described in their original work, this evidences the dramatic effect that slight changes in experimental conditions have (e.g. temperature, pH, seed size and concentration) on the final results of the seed-growth method reported by Puentes *et al.* In spite of this, careful control of the growing process by means of UV-vis absorption spectroscopy allows the obtention of **AuNP-Gn@Cit** of the desired size, as demonstrated in this work.

Table 3.2. Sizes of **AuNP-Gn@Cit** obtained for growing steps G1 to G6.

AuNP-Gn@Cit	Diameter from λ_{LSPR} / nm	Diameter from TEM / nm
AuNP-G1@Cit	28	22 ± 4
AuNP-G2@Cit	35	-
AuNP-G3@Cit	42	38 ± 6
AuNP-G4@Cit	52	-
AuNP-G5@Cit	58	-
AuNP-G6@Cit	72	83 ± 14

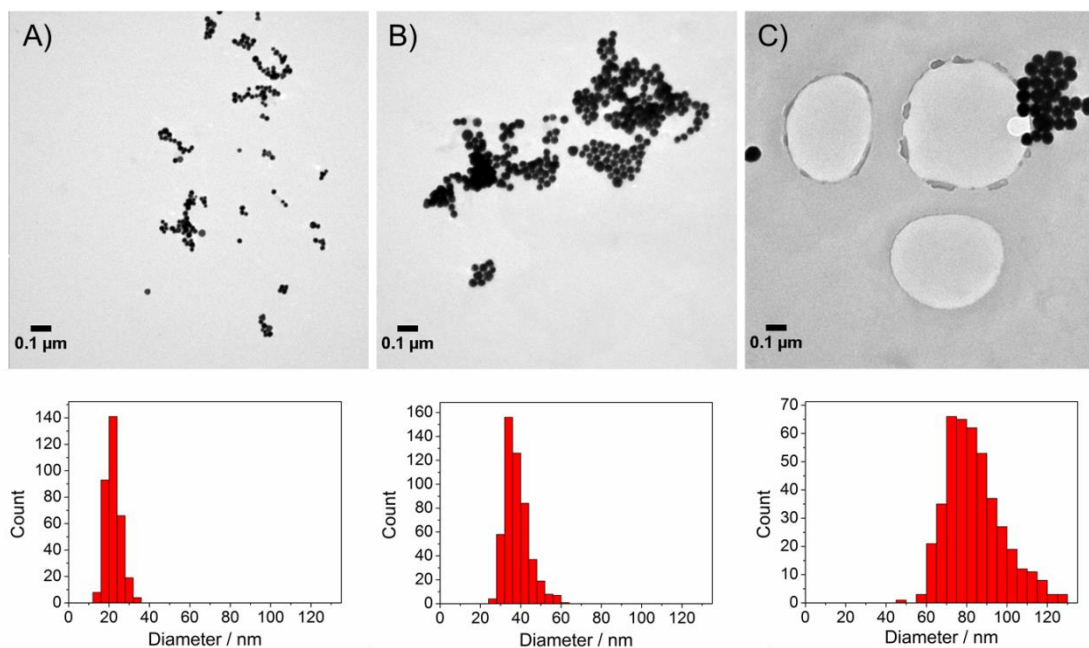


Figure 3.12. TEM images and size histograms of A) **AuNP-G1@Cit**, B) **AuNP-G3@Cit** and C) **AuNP-G6@Cit** synthesized by the seed-growth method.

Despite its capacity to provide large, good-quality Au NPs, the seed-growth method used in this thesis however suffers from an important drawback: each growth step requires a ~2:1 dilution of the initial gold colloid, which means that dispersions with very low concentrations of Au NPs were finally obtained after several of these steps. For instance, while ~8 nM suspensions of ~15 nm-in-diameter, citrate-stabilized Au NPs could be prepared by means of the Turkevich-Frens method, the use of the seed-growth method only allowed the synthesis of 0.6 nM suspensions of **AuNP-G6@Cit.**^a As will be later discussed, this imposes severe limitations to the characterization of the organic layer of the seed-growth Au NPs by means of standard techniques (e.g. IR and NMR spectroscopies, chemical analysis).

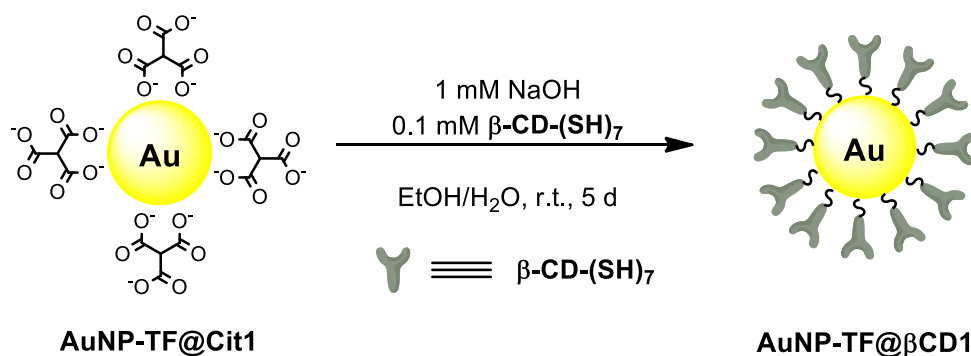
(c) Ligand exchange for the preparation of CD-coated Au NPs: AuNP-TF@ β CD1

After the synthesis of citrate-stabilized Au NPs, the second step in the preparation of thiol-functionalized Au colloids by means of indirect methods consists in replacing the labile citrate stabilizing molecules by the desired ligand thanks to the formation of stronger Au-S bonds. There is no standard protocol to undertake this process and different conditions can be found in the literature depending on the nature of the thiolated ligand.^{26,27,28} However, all of them share a common feature: the new stabilizer is generally added by injecting a small aliquot of a solution of the thiol of choice in a proper solvent into a freshly prepared colloidal dispersion of Au NPs in water. Owing to the high affinity between Au and S atoms, as soon as the addition takes place, replacement of citrate anions by thiolates occurs.²⁹ However, formation of a well-organized and well-packed monolayer of the thiolated ligand onto the Au NP surface may require a longer time.³⁰ It must be noted that these procedures work perfectly well also for ligands which are only partially soluble in water, taking into account that NPs are generally in the nM concentration range and therefore, the effective amount of thiolated stabilizer required for a complete exchange is generally in the μ M range.

The ligand exchange procedure developed in this part of the work was intended to be a general strategy for any water-soluble ligand, including not only the thiolated cyclodextrin derivatives of interest but also other organic thiols that were planned to be

^a A detailed explanation of the methodology used to estimate the concentration of the gold colloids prepared and used along this thesis is given in Chapter 7 (section ?).

used along this thesis. For this, we took the preparation of host-functionalized Au NPs with β -CD-(SH)₇ by ligand exchange from **AuNP-TF@Cit1** (mean diameter ~ 15 nm) as a benchmark process, from which **AuNP-TF@ β CD1** were prepared. Scheme 3.20 shows the procedure developed with this aim, in which the proper amount of β -CD-(SH)₇ was suspended in 10 mM NaOH in ethanol and quickly added over the corresponding citrate-stabilized colloidal suspension of Au NPs. The proper amount of thiolated ligand was estimated according to a full coverage of the Au NP surface, calculated from the β -CD size (~1.84 nm²) and the surface area of Au NPs (~707 nm² for a 15 nm in diameter Au NP). Around 390 β -CD molecules are needed to completely cover the surface of a given Au NP, which would correspond to a 2 μ M β -CD concentration upon complete ligand exchange of the initial colloid (ca. 8 nM). Therefore, using a final 0.1 mM concentration of the thiolated ligand assures a sufficient ligand excess to completely replace the citrate stabilization. In addition, the presence of NaOH facilitates deprotonating the thiol functionalities allowing the interaction of the corresponding thiolates with Au surfaces. Actually, in view of literature reports on the formation of self-assembled monolayers (SAMs) of alkanethiolates over Au surfaces which may require variable times to become compacted depending on the thiolated specie, the ligand exchange mixtures were allowed to stir at room temperature and prevented from light for 5 days.



Scheme 3.20. Preparation of **AuNP-TF@ β CD1** by ligand exchange.

After the ligand exchange process, a purification step was needed in order to remove all excess β -CD-(SH)₇ molecules. However, due to the nature of Au NPs particular purification procedures are normally carried out for such purposes, like dialyses or centrifugation-based procedures.^{8,31} In this thesis **AuNP-TF@ β CD1** was purified by centrifugation and further dialyses against DMF, because of the higher solubility of the free thiolated cyclodextrin ligand in this solvent with respect to water.

Importantly, the capacity of the obtained particles to be centrifuged and dialyzed was an indirect proof that β -CD-(SH)₇ had been incorporated to the surface of Au NPs, since their parent citrate-stabilized Au NPs did not resist such processes. Finally, cleaned host-functionalized Au NPs were resuspended in the minimum amount of water for their proper characterization.

First of all, we inspected the LSPR band of **AuNP-TF@ β CD1** by UV-Vis absorption spectroscopy. An important red-shift and band broadening was observed with respect to **AuNP-TF@Cit**, which demonstrated that partial aggregation of Au NPs took place during the ligand exchange and/or purification processes. Two different effects could account for the formation of aggregates: (i) insufficient coverage of the nanoparticles with the thiolated cyclodextrin derivative once the initial citrate stabilizers were removed, which should result in irreversible aggregation; (ii) supramolecular interactions between close-by CD-functionalized NPs through H-bonding due to the large density of hydroxyl groups being exposed on their surface. In the latter case, dissociation of the aggregates was expected if enough energy was provided to the system as to cleave the weak supramolecular bonds between nearby nanoparticles (e.g. thermally). For this reason, samples of **AuNP-TF@ β CD1** were irradiated at 532 nm with a ns pulsed laser source, aiming to locally increase the temperature around the nanoparticles owing to the plasmon-induced photothermal effect. Surprisingly, irradiation at low powers (~ 70 – 100 mW) for rather short times (~ 5 min) caused blue-shift and spectral narrowing of the LSPR band, indicating disaggregation and the formation of smaller particles (Figure 3.13A). This phenomenon stopped once the LSPR band maximum diminished down to 531 nm and no further spectral changes were observed for longer irradiation times.

As shown in Figure 3.13B, the final extinction spectrum obtained after irradiation did not fully reproduce that of the initial citrate-stabilized Au NPs, but a 10-nm red-shift and a slight band broadening was still observed. Although such spectral changes could be simply attributed to the variation in the electrostatic environment of the NP arising from replacing citrate ligands by thiolates, they could also be due to incomplete light-induced disaggregation of the particles. For this reason, additional experiments were carried out for **AuNP-TF@ β CD1** after irradiation. First, TEM analysis of these particles revealed that they presented a mean diameter of 15 ± 3 nm, evidencing that their size and shape was preserved with respect to **AuNP-TF@Cit**, as can be seen in Figure 3.13C-D. Actually, this result proved that: (i) although the treatment required for preparation of **AuNP-TF@ β CD1** resulted in particle aggregation, this process could be efficiently reverted back photothermally upon irradiation; (ii) light-induced

disaggregation of **AuNP-TF@ β CD1** did not result in particle degradation, as reported for other Au NPs when irradiated at high laser powers.³² Once irradiated and disaggregated, suspensions of **AuNP-TF@ β CD1** in water were observed to preserve their spectral properties for several days, thus indicating that back-aggregation of the particles took place at a very slow rate.

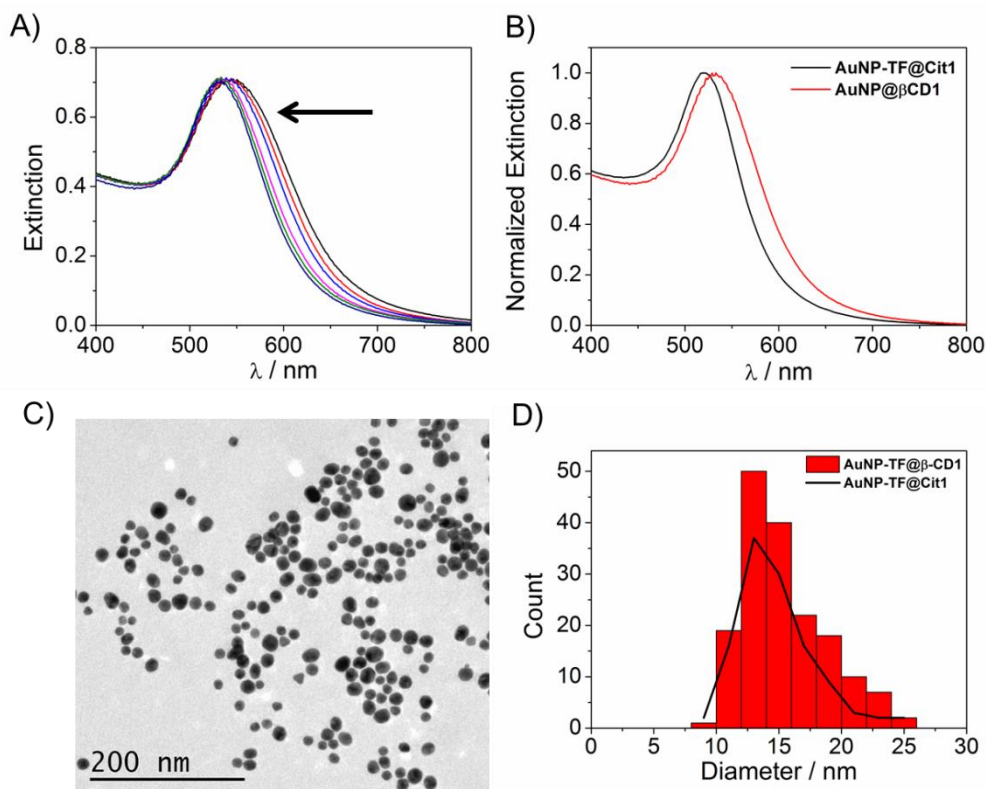


Figure 3.13. A) Extinction spectra of dialyzed **AuNP-TF@ β CD1** after plasmon excitation at 532 nm (70 mW) during variable times. The arrow indicates the observed LSPR shift. B) Comparison of the extinction spectra of **AuNP-TF@Cit1** and irradiated **AuNP-TF@ β CD1**. C-D) TEM image and size distribution of irradiated **AuNP-TF@ β CD1**. For comparison, the size histogram of **AuNP-TF@Cit1** is also shown in D).

Based on the aggregation-disaggregation behavior observed for **AuNP-TF@ β CD1** and their stability in dispersions of different solvents, we could infer that functionalization of their surface with thiolated cyclodextrin molecules had indeed taken place. In spite of this, additional evidences of the presence of **β -CD-(SH)₇** on the surface of the ligand-exchanged Au NPs were forsaken, which should also allow us establishing whether the light-induced disaggregation process of these particles resulted in partial cleavage of Au-S bonds. To start with, characterization by IR spectroscopy was attempted, but it was not possible to detect any signal coming from

the capping layer, probably because the amount of organic component which corresponded to a very small fraction of the sample was probably well below the detection limit of the instrument. The same problem was encountered when characterization of the organic layer was attempted by ICP-MS or chemical analysis.

Next, detection of the organic capping layer of **AuNP-TF@ β CD1** was pursued by means of NMR spectroscopy. For that, their 1D DOSY ^1H NMR spectrum was recorded, for which we chose appropriate settings as to allow selective detection of the ^1H NMR resonances of the organic molecules with very low diffusion coefficients (i.e. those directly attached to the surface of the Au NPs. Figure 3.14 compares the ^1H NMR spectrum of **β -CD-(SH)₇** with that of irradiated **AuNP-TF@ β CD1** and their corresponding 1D DOSY ^1H NMR spectrum. It must be first noticed that no signals were observed in the regular ^1H NMR spectrum of **AuNP-TF@ β CD1** aside from those arising from the solvents (DMF and water). This indicates that the concentration of **β -CD-(SH)₇** in the sample was extremely low, which suggests that the excess of free molecules of this ligand was efficiently removed during the purification of **AuNP-TF@ β CD1**. By contrary, several broad resonances were found in the 1D DOSY ^1H NMR spectrum of the same nanoparticles, which can be attributed to Au NP-tethered **β -CD-(SH)₇** molecules by comparison of their chemical shifts to those of the ^1H NMR spectrum of the free ligand. Moreover, this assignment is supported by additional features of the 1D DOSY ^1H NMR spectrum of **AuNP-TF@ β CD1**: (i) loss of the $-\text{SH}$ signal of **β -CD-(SH)₇** at $\delta = 2.1$ ppm, which confirms the formation of Au-S bonds; (ii) broadening of the 2-OH, 3-OH and H-1, H-3 and H-5 signals, as described for organic ligands immobilized onto the surface of nanoparticles due to reduced molecular tumbling and stronger spin-spin interactions,³³ and (iii) disappearance of the H-6a signal at $\delta = 2.79$ ppm, which must be one of the closest nuclei to the Au NP and, therefore, is expected to be so affected by spectral broadening as to lie hidden in the background of the spectrum. Therefore, these results confirmed successful functionalization of the surface of **AuNP-TF@ β CD1** with the desired **β CD(SH)₇** ligand. In addition, it must be mentioned that a narrower, additional signal at $\delta = 3.5$ ppm was observed in the 1D DOSY ^1H NMR spectrum of **AuNP-TF@ β CD1**, which can be tentatively ascribed to water molecules that supramolecularly interact with the chemisorbed cyclodextrin ligands, probably by H-bonding.

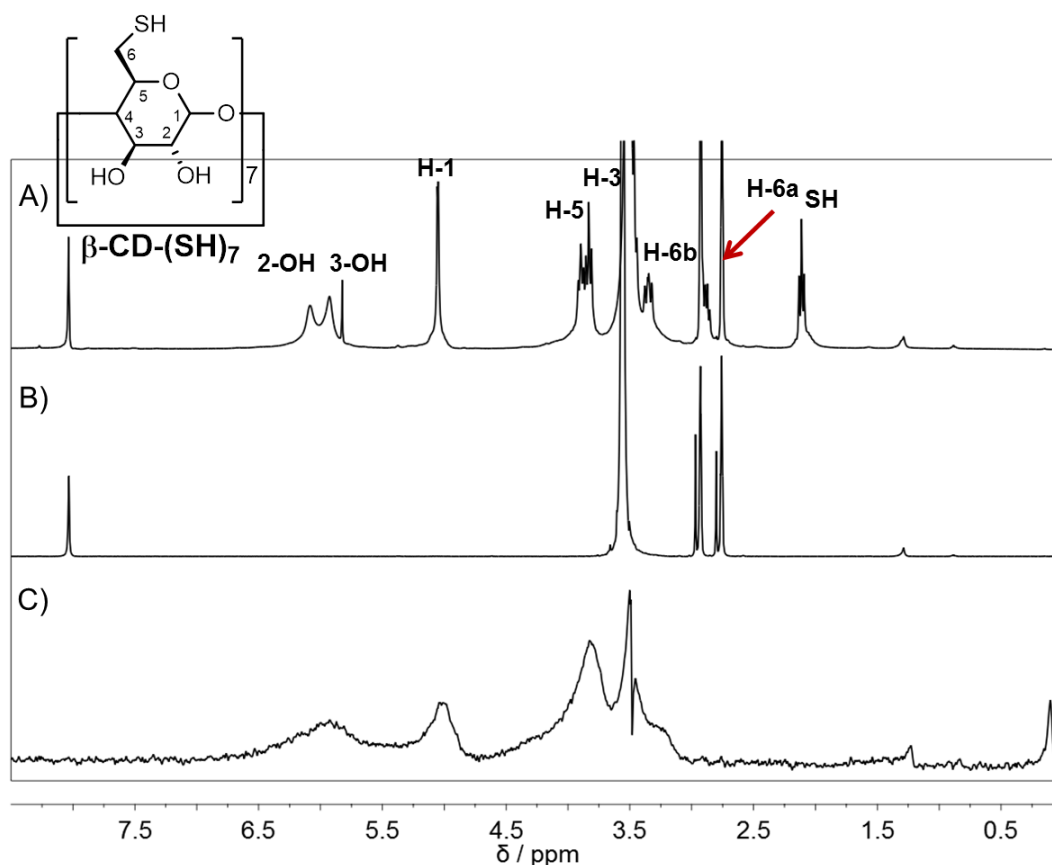


Figure 3.14. A) $^1\text{H-NMR}$ (400 MHz, DMF-d_7) spectrum of free ligand $\beta\text{-CD-(SH)}_7$. B) $^1\text{H-NMR}$ (400 MHz, DMF-d_7) spectrum of $\text{AuNP-TF@}\beta\text{CD(SH)}_7$, where no signals were observed for free ligand $\beta\text{-CD-(SH)}_7$. C) 1D DOSY $^1\text{H-NMR}$ (400 MHz, DMF-d_7) spectrum of the same sample, which was programmed to selectively detect the signals of ligands that are directly attached to the surface of the gold nanoparticles (i.e. those presenting the lowest diffusion coefficients).

(d) Ligand exchange for the preparation of CD-coated Au NPs: $\text{AuNP-TF@}\beta\text{CD}_2$

Au NPs functionalized with the monothiolated $\beta\text{-CD}$ derivative $\beta\text{-CD-(SH)}_1$ ($\text{AuNP-TF@}\beta\text{CD}_2$), were prepared following the very same procedure applied for the preparation of $\text{AuNP-TF@}\beta\text{CD}_1$. The preparation of this NP set proved to be relevant since the final Au NPs had to be irradiated (70-100 mW) to obtain a well-dispersed colloid, and there are some precedents in the literature about Au-S bond cleaving upon NP irradiation with ns-pulsed laser sources.^{27,28} Indeed, $\text{AuNP-TF@}\beta\text{CD}_2$ partially aggregated at regular purification conditions (centrifugation + dialysis + irradiation) and they proved to be unstable in preliminary irradiation experiments at higher powers. In view of this results we abandoned the preparation of CD-modified Au NPs with

monothiolated cyclodextrins, and focused on the derivatization of Au NPs with perthiolated cyclodextrin derivatives.

(e) Ligand exchange for the preparation of CD-coated Au NPs: AuNP-G6@ β CD

To check the viability of the ligand exchange process for both small and large Au NPs, the same procedure followed for **AuNP-TF@ β CD1** was then applied for the bigger **AuNP-G6@Cit** (mean diameter \sim 83 nm) to prepare **AuNP-G6@ β CD** (see Scheme 3.20). After ligand exchange, these nanoparticles were purified in the same way as their smaller counterparts. As previously observed for **AuNP-TF@ β CD1**, **AuNP-G6@ β CD** showed increased stability with respect to parent **AuNP-G6@Cit**, since they could be centrifuged, subsequently dialyzed and finally resuspended in water. This was again a clear indication that the labile citrate ligands which weakly stabilized the colloidal suspension of Au NPs by electrostatic interactions had been replaced by **β -CD-(SH)₇**, which acts as a more robust steric stabilizer.

Upon UV-Vis absorption inspection of the LSPR band of the final Au NPs, a similar result to that previously obtained for **AuNP-TF@ β CD1** was found (Figure 3.15A). On the one hand, the LSPR maximum position presented a 4-nm red-shift with respect to that of the parent **AuNP-G6@Cit** ($\lambda_{\text{LSPR}} = 545$ nm), suggesting the incorporation of the thiol function onto the surface of the Au NPs. In addition, the presence of an intense and broad shoulder from 600 to 750 nm was also observed, uncovering that NP aggregation had occurred during the ligand exchange and/or purification processes. As can be seen in Figure 3.15A, when trying to revert such aggregation photothermally by plasmon excitation at 532 nm at low powers (\sim 70 mW), a huge blue-shift of the LSPR band from 545 to 517 nm together with a decreased extinction intensity was induced. TEM analysis of the same sample revealed that not only NP disaggregation had occurred, but also size reduction and fragmentation of an important part of the NPs into much smaller Au nanostructures (Figure 3.15B), in contrast to what had been observed for **AuNP-TF@ β CD1** under similar irradiation conditions. Although it is not clear to us whether these processes proceeded via photothermal ablation or other mechanisms such as Coulomb explosion,³⁴ this result clearly demonstrated that larger CD-coated Au NPs are more prone to undergo light-induced degradation. For this reason and the fact that photodriven disaggregation would be probably required in the preparation of these systems, the synthesis of very large Au NPs functionalized with thiolated cyclodextrins was avoided in this thesis from then on.

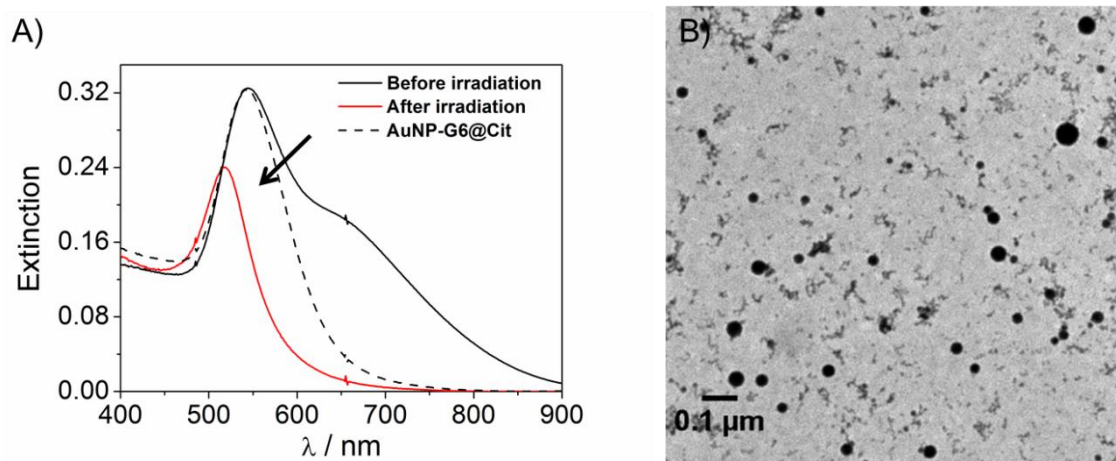


Figure 3.15. A) Extinction spectra of dialyzed **AuNP-G6@ β CD** before and after plasmon excitation at 532 nm (70 mW) for few seconds. The arrow indicates the observed LSPR shift and, for comparison, the spectrum of parent **AuNP-G6@Cit** is also shown. B) TEM image of the irradiated **AuNP-G6@ β CD** sample.

In view of the aforementioned results, other methods of disaggregating **AuNP-G6@ β CD** were explored. The best results were obtained when, after purification by dialysis, these nanoparticles were resuspended in the minimum amount of DMF instead of water. In this case, the extinction spectrum shown in Figure 3.16A was measured, which resembled that determined for **AuNP-G6@Cit** in water prior to ligand exchange and did not show a broad red-shifted shoulder. In spite of this, a 12 nm bathochromic shift of the LSPR band was still observed for **AuNP-G6@ β CD**, a difference that was mainly ascribed to the electrostatic effect caused on the surface of the nanoparticles by replacing citrate molecules with thiolated cyclodextrins as well as water with DMF. Accordingly, no (or minor) particle aggregation was expected under such conditions. As illustrated in Figure 3.16B-C, when avoiding light-induced disaggregation, **AuNP-G6@ β CD** preserved the size and shape of the parent citrate-stabilized particles after the ligand exchange process. In particular, the obtained particles presented a mean diameter of 79 ± 11 nm, which is in the same range of that of **AuNP-G6@Cit** (~ 83 nm). This, together with the redispersibility of these nanoparticles in several organic solvents, evidenced the effectiveness of the ligand exchange process here developed for large Au NPs. Unfortunately, direct characterization of the organic layer of **AuNP-G6@ β CD** by other techniques such as 1D DOSY ^1H NMR or ICP-MS could not be carried out because of: (i) the small amounts of these nanoparticles that could be prepared due to the scale limitation of the

seed-growth method; and (ii) the rather low redispersibility in water and organic solvents displayed by these larger particles compared to **AuNP-TF@ β CD1**.

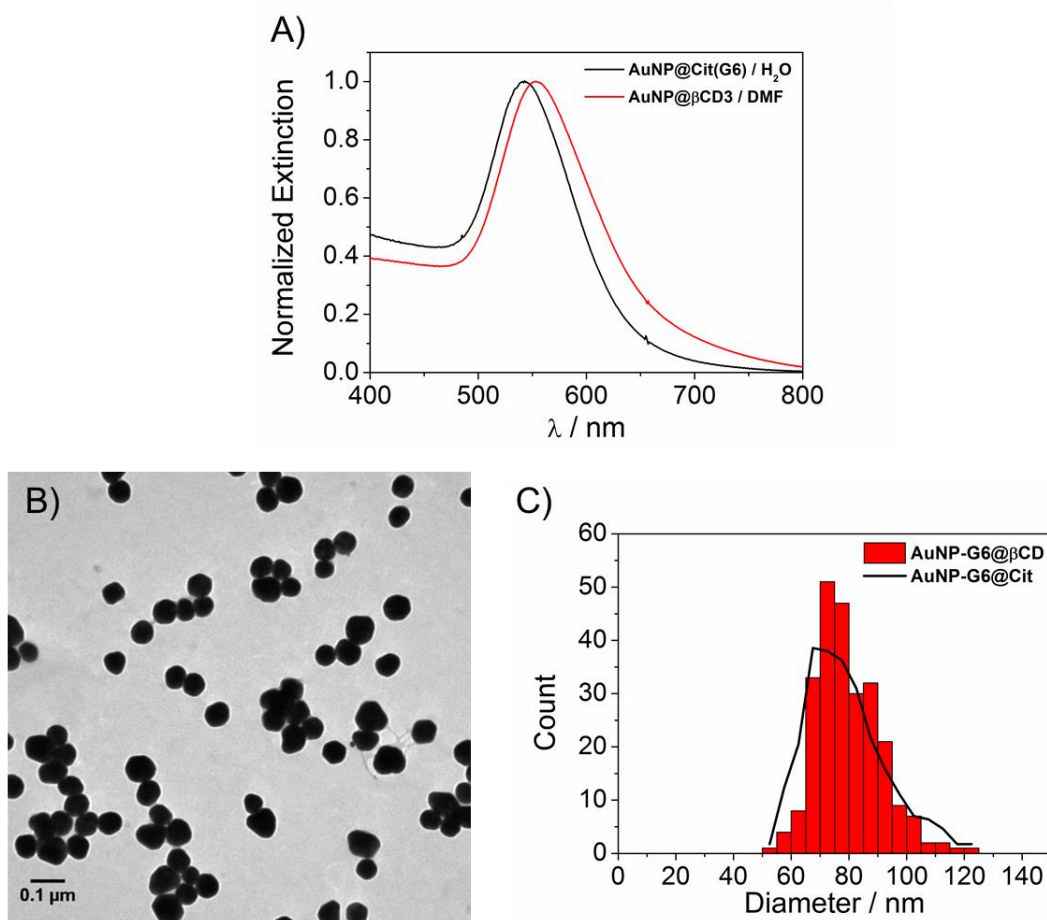


Figure 3.16. A) Comparison of the extinction spectra of **AuNP-G6@Cit** in water and **AuNP-G6@ β CD** in DMF. B) TEM image of **AuNP-G6@ β CD** after dialyses. C) Size histograms of **AuNP-G6@Cit** and **AuNP-G6@ β CD**.

3.4. SUMMARY AND CONCLUSIONS

In this chapter, the synthesis and characterization of CD-functionalized Au NPs prepared by different methods has been described. Such structures were prepared by the Au-S bond strategy by which thiolated ligands attach to the surface of Au NPs. Therefore, proper thiolated derivatives have been prepared for that purpose and later on incorporated to the surface of Au NPs by different methods:

- a) β -CD-(SH)₇ was synthesized in three steps and 41% overall yield. With the same methodology, α -CD-(SH)₆ was synthesized in three steps and 33% overall yield. In the case of the biggest CD host, the obtained yield was much higher. γ -CD-(SH)₈ was synthesized in two steps and 84% overall yield. This fact is mainly due to the higher reactivity observed for γ -CD and the corresponding intermediate, and the possibility to skip the additional step introduced for the other members. Regarding the monothiolated β -CD derivative β -CD-(SH)₁, it was prepared in two steps and 20% overall yield.
- b) The synthesis of the C6-perthiolated derivatives of the CD family qualitatively highlighted the distinct supramolecular capability of the different CDs, as evidenced by our results after the first synthetic step where decreasing affinity towards I₂ was observed when increasing the CD size.
- c) The direct synthesis of CD-functionalized Au NPs provided **AuNP-K@ β CD** with tunable sizes in the 3-10 nm range with rather high polydispersities, but the method failed to produce bigger NPs leading to the formation of irregular Au microstructures.
- d) Bigger host-functionalized NPs were obtained with a two-step process via citrate-stabilized Au NPs which were prepared by the Turkevich-Frens and the seed-growth method. The former provided **AuNP-TF@Cit** of around 15 nm and the latter 6 generations of **AuNP-Gn@Cit** up to 70 nm-in-diameter both with good polydispersities.
- e) A ligand exchange process was applied to obtain the target CD-functionalized NPs. **AuNP-TF@ β CD** (~15 nm diameter) could be obtained with no detrimental effect over the size and the morphology of parent citrate-stabilized NPs but with

an important NP aggregation attributed to *H*-bonding-mediated assembly between nearby CDs of distinct Au NPs which was probably induced by the purification process itself. Interestingly, we were able to revert back such aggregation by the photothermal effect exhibited upon ns-pulsed laser irradiation ($\lambda = 532$ nm, and 70-100 mW) without compromising the NPs. Surprisingly, when trying to apply the same conditions to **AuNP-G6@ β CD** (~70 nm diameter) an important NP fragmentation was observed suggesting increased photothermal effects for bigger particles. The functionalization of Au NPs with **β -CD-(SH)₁** failed to produce a photostable SAM over the surface of Au NPs as evidenced by the partial aggregation observed upon the disaggregation treatment.

In conclusion, we have described different methodologies for the obtention of CD-functionalized Au NPs based on the Au-S bond formation between thiolated CD derivatives and the surface of Au NPs. Such nanostructures have shown promising properties accounting for their improved stability for the applications that will be described in the following chapters.

3.5. BIBLIOGRAPHY

- [1] Szejtli, J. *Chem. Rev.* **1998**, 98, 1743.
- [2] Chen, Y.; Zhang, Y.-M.; Liu, Y. *Chem. Comm* **2010**, 46, 5622.
- [3] Rekharsky, M. V.; Inoue, Y. *Chem. Rev.* **1998**, 98, 1875.
- [4] Duveneck, G. L.; Sitzmann, E. V.; Eisenthal, K. B.; Turro, N. J. *J. Phys. Chem.* **1989**, 93, 7166.
- [5] Banu, H. S.; Lalitha, A.; Srinivasan, C. *Chem. Commun.* **1999**, 607.
- [6] Yang, C.; Mori, T.; Wada, T.; Inoue, Y. *New. J. Chem.* **2007**, 31, 697.
- [7] Park, C.; Youn, H.; Kim, H.; Noh, T.; Kook, Y. H.; Oh, E. T.; Park, H. J.; Kim, C. *J. Mater. Chem.* **2009**, 19, 2310.
- [8] Aykaç, A.; Martos-Maldonado, M. C.; Casa-Solvas, J. M.; Quesada-Soriano, I.; García-Maroto, F.; García-Fuentes, L.; Vargas-Berenguel, A. *Langmuir* **2014**, 30, 234.
- [9] Yang, L.; Chen, C.; Liu, X.; Shi, J.; Wang, G.; Zhu, L.; Guo, L.; Glennon, J. D.; Scully, N. M.; Doherty, B. E. *Electrophoresis* **2010**, 31, 1697.
- [10] Li, X.; Liu, D.; Wang, Z. *Biosens. Bioelectron.* **2011**, 26, 2329.
- [11] Scente, L.; Szejtli, J. *Adv. Drug. Del. Rev.* **1999**, 36, 17.
- [12] Rojas, M. T.; Königer, R.; Stoddart, J. F. Kaifer, A. E. *J. Am. Chem. Soc.* **1995**, 117, 336.
- [13] Defaye, G.; Crouzy, S.; Evrard, N.; Law, H. *WO9961483 (A1)*.
- [14] Nelles, G.; Weisser, M.; Back, R.; Wolhart, P.; Wenz, G.; Mittler-Neher, S. *J. Am. Chem Soc.* **1996**, 118, 5039.
- [15] Wang, H. M.; Wenz, G. *Chem. Asian J.* **2011**, 6, 2390.
- [16] Tomono, K.; Goto, H.; Ueda, H.; Nagai, T.; Watanabe, J. *Drug Dev. Ind. Pharm.* **2002**, 28, 1303.
- [17] Scente, L.; Fenyvesi, É.; Szejtli, J. *Environ. Sci. Technol.* **1999**, 33, 4495.
- [18] Brust, M.; Walker, M.; Bethel, D.; Schiffrin, D.; Whyman, R. *J. Chem. Soc. Chem. Commun.* **1994**, 801.
- [19] Liu, J.; Ong, W.; Román, E.; Lynn, M. J.; Kaifer, A. E. *Langmuir*, **2000**, 16, 3000.
- [20] Bain, C. D.; Troughton, E. B.; Tao, Y. T.; Evall, J.; Whitesides, G. M.; Nuzzo, R. G. *J. Am. Chem. Soc.* **1989**, 111, 321.
- [21] Turkevich, J.; Stevenson, P. C.; Hillier, J. *Faraday Discuss.* **1951**, 55.
- [22] Kimling, J.; Maier, M.; Okenve, B.; Kotadis, V.; Ballot, H.; Plech, A. *J. Phys. Chem B* **2006**, 110, 15700.
- [23] Frens, G. *Nature Phys. Sci.* **1973**, 241, 20.
- [24] Bastús, N. G.; Comenge, J.; Puntès, V. *Langmuir* **2011**, 27, 11098.

- [25] Haiss, W.; Thanh, N. T. K.; Fernig, A. J. D. *Anal. Chem.* **2007**, 79, 4215.
- [26] Jing, B.; Chen, X.; Wang, X.; Zhao, Y.; Qiu, H. *ChemPhysChem* **2008**, 9, 249.
- [27] Bakhtiari, A. B. S.; Hsiao, D.; Jin, G.; Gates, B. D.; Branda, N. R. *Angew. Chem. Int. Ed.* **2009**, 48, 4166.
- [28] Poon, L.; Zandberg, L.; Hsiao, D.; Erno, Z.; Sen, D.; Byron, D. G. *ACS Nano* **2010**, 11, 6395.
- [29] Karpovich, D. S.; Blanchard, G. J. *Langmuir* **1994**, 10, 3315.
- [30] DeBono, R. F.; Loucks, G. D.; Manna, D. D.; Krull, U. J. *Can. J. Chem.* **1996**, 74, 677.
- [31] Yamashita, S.; Fukushima, H.; Niidome, Y.; Mori, T.; Katayama, Y.; Niidome, T. *Langmuir* **2011**, 27, 14621.
- [32] González-Rubio, G.; Martínez-Guerrero, A.; Liz-Marzán, L. M. *Acc. Chem. Res.* **2016**, 49, 678.
- [33] Mayer, C. *Annual Reports on NMR Spectroscopy* **2005**, 55.
- [34] Werner, D.; Hashimoto, S.; Uwada, T. *Langmuir* **2010**, 26, 9956.

Chapter 4:

Photocatalysis with Gold Nanoparticles

4.1. INTRODUCTION

As discussed in chapter 1, a wide number of applications have been proposed for Au NPs based on their plasmonic behavior. For instance, they have already been applied in the fields of therapeutics,¹ sensing^{2,3} and photovoltaics.⁴ Photocatalysis is another relevant field where the application of the intricate optical properties of Au NPs is being explored,^{5,6,7,8} and it is indeed the area of interest of this part of this thesis. For this reason, a brief review of the state of the art in the use of Au NPs for photocatalysis will be done in the introduction of this chapter.

To date photocatalysis with Au NPs has been already investigated for a wide variety of chemical processes, including several reduction reactions,^{9,10} oxidations,^{11,12} dissociation processes^{13,14} and organic syntheses.^{15,16} The photocatalytic efficiency of Au NPs in these processes depends on a number of aspects, such as their optical (and other physico-chemical) properties, the irradiation conditions, and the nature of the chemical process that is to be promoted. Among them, three key factors determining the photocatalytic activity of Au NPs will be next discussed: (i) the specific mechanism of photocatalytic action, (ii) the combined use with other (photo)catalysts, (c) the strategy employed to guarantee the interaction between Au NPs and substrate molecules.

4.1.1. Mechanisms of photocatalytic action

As shown in Figure 4.1,¹⁷ three main mechanisms account for the photocatalytic activity of Au NPs: (i) near field enhancement, which leads to a gigantic increase of the excitation light intensity around the particles and, therefore, of the linear and nonlinear absorption efficiencies of nearby photoreagents; (ii) the photothermal effect, i.e. the conversion of light into heat at their surface, which can promote thermally-induced chemical processes; (iii) the generation of hot charge carriers, which can be injected into surrounding molecules to trigger redox reactions.^{5,6,7,8} All these mechanisms (and some of their combinations) have been already exploited in the photocatalysis with Au NPs, thus evidencing the versatility of such structures to induce or promote a wide variety of chemical processes.

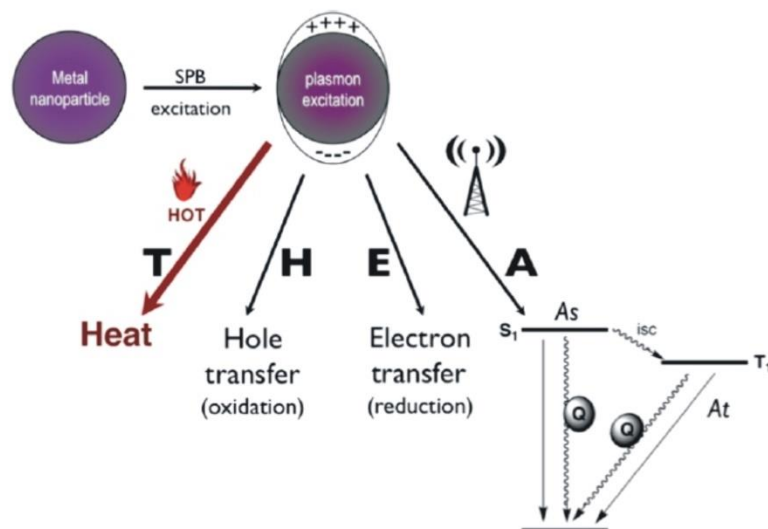


Figure 4.1. Plasmon excitation leads to a variety of effects over molecules adsorbed, bounded or nearby to Au NPs that can lead to photocatalysis. In the presence of the appropriate receptor, field enhancement effects can occur (A). Upon plasmon excitation Au NPs can act as donors (E) or acceptors (H) of electrons. Plasmon relaxation can also lead to heat release by the Au NP (T). Adapted from reference 17.

The first of these mechanisms, electromagnetic field enhancement, is based on the plasmon-based capacity of Au NPs to disperse light of certain frequencies with great efficiency.⁷ As discussed in chapter 1, Au NPs can behave as antennae amplifying the near component of the light, a process which decays exponentially from the surface of Au NPs. Therefore, field-enhancement of incident radiation only occurs at very short distances from the particle surface, in the order of a few tens of nanometers.

This mechanism can be applied to induce photochemical reactions where the optical transition which initiates the process is of very low probability, and consequently, requires the use of high-intensity irradiation sources to be produced. However, if the photoactive molecules initiating the reaction are in close proximity to Au NPs, their excitation will be favored by electromagnetic field enhancement of the incident radiation, even under low-intensity conditions. An application of this mechanism was described by Misawa *et al* to induce the polymerization process of an epoxy resin via two-photon absorption (TPA), a photophysical process which displays very poor probabilities.¹⁸ With this aim, the resin was deposited over a surface covered with Au nanostructures that were separated by few nm one with respect to each other,

in which intersections very important field enhancements effects took place (Figure 4.2A). This allowed the photoinitiator molecules lying close to these intersections to undergo the TPA process, and therefore, to induce the polymerization of the resin in these areas (Figure 4.2B)

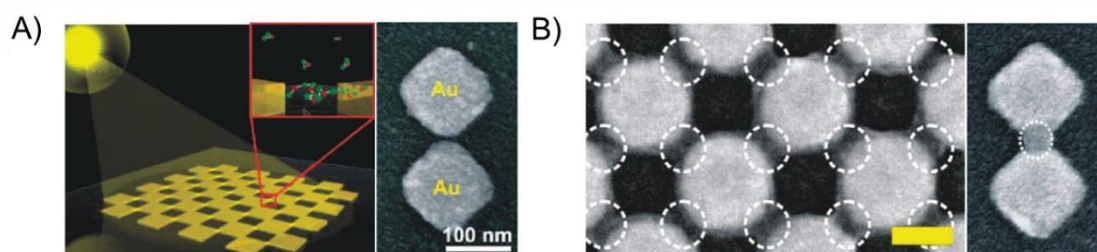


Figure 4.2. A) Left: schematics of the photocatalyst employed consisting in a chess pattern of square-sectioned Au nanostructures (edge ~ 100 nm) deposited over a glass surface. Right: Scanning electron microscopy (SEM) image of two nanostructures separated by 5.6 nm before irradiation (B) SEM images of the photocatalyst after 3 h irradiation at $\lambda = 600\text{-}1000$ nm. Polymerized regions are indicated with discontinuous circles. Adapted from reference 18.

The second photocatalytic mechanism of Au NPs implies the injection of a high-energy electron (or hole) after plasmon excitation to a vicinal species causing its reduction (or oxidation). Obviously, charge carrier injection requires the substrate molecules to be directly on the surface of Au NPs. An interesting example of this type of mechanism is the oxidation of *sec*-phenethyl and benzyl alcohols described by Scaiano *et al* (Figure 4.3A).¹⁹ In this study, the selected alcohols were irradiated with visible light in the presence of Au NPs and hydrogen peroxide to obtain acetophenone and benzaldehyde with yields up to 50 % with pulsed radiation (Figure 4.3B) and 95 % with cw radiation. The proposed mechanism for this process starts with an electron transfer from the surface of Au NPs to hydrogen peroxide to produce a hydroxyl anion and a hydroxyl radical. Then the hydroxyl radical will generate a peroxide radical that will further oxidize the target alcohols. The resulting products of this oxidation regenerate the catalyst by the transfer of an electron before their conversion into the final carbonyl compounds (Figure 4.3C).

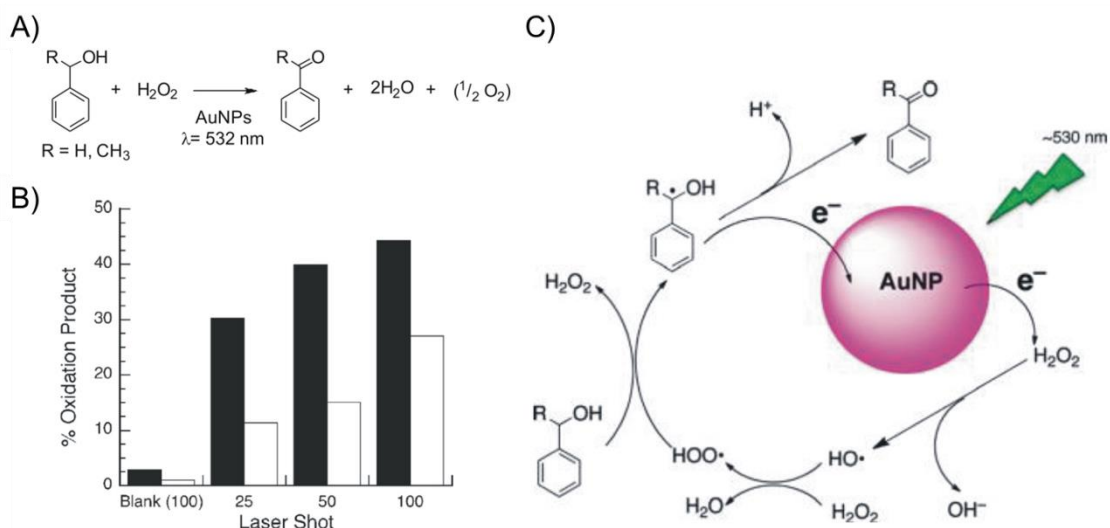


Figure 4.3. (A) Oxidation reaction of benzyl alcohols mediated by plasmon excitation of Au NPs at $\lambda = 532$ nm in the presence of H_2O_2 . (B) Bar plot illustrating the conversion percentage to benzaldehyde (white) and to acetophenone (black) from *sec*-phenethyl and benzyl alcohols, respectively. (C) Proposed mechanism for the photooxidation of benzyl alcohols in the presence of Au NPs. Adapted from reference 19.

Finally, the third photocatalytic mechanism of action of Au NPs is the so called photothermal effect (PTE). As already discussed in chapter 1, this effect is due to the major relaxation pathway of the excited LSPR, and can lead to a temperature rise which can be in the range of several hundreds of degrees at very short distances from the NPs.^{7,17} Therefore, such dramatic increase of the temperature can be exploited to thermally induce chemical reactions. An example of this application is the photocatalytic decomposition of dicumyl peroxide described by Scaiano *et al.*¹⁷ In this study the thermal decomposition of this substrate was achieved in the presence of Au NPs under irradiation with visible light (Figure 4.4).

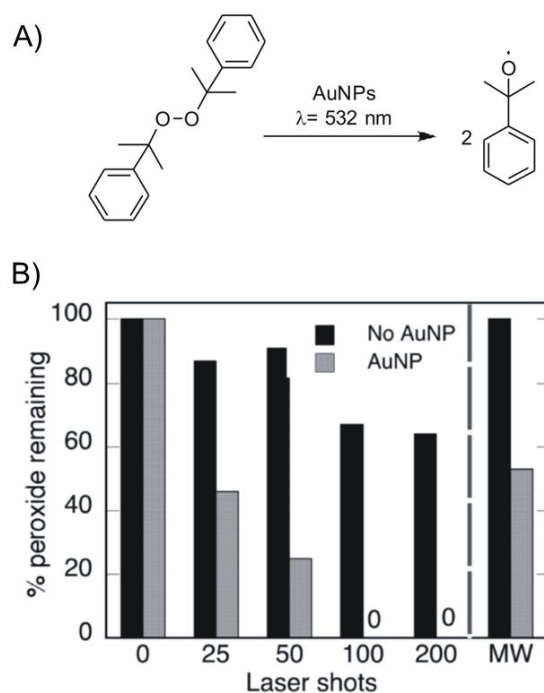


Figure 4.4. (A) Dissociation reaction of dicumyl peroxide under irradiation with a pulsed laser source at $\lambda = 532$ nm in the presence of Au NPs. (B) Unreacted substrate percentage with respect to the number of laser shots applied to a 1 mM dicumyl peroxide solution in 5 % methanol in water. Adapted from reference 17.

4.1.2. Direct photocatalysis vs use of other (photo)catalysts

Regardless of which is the actual mechanism of action of Au NPs in a photocatalytic process, these nanostructures can actuate over the reactant molecules in two different ways: (a) directly, and therefore acting as the only catalyst of the reaction (direct photocatalysis); (b) cooperating with other (photo)catalysts in order to finally induce the desired chemical process. In the latter case, the function of Au NPs can be very diverse depending on the specific reaction that takes place and what the other (photo)catalysts used are. For instance, Au NPs can be used to locally heat the reaction medium by PTE and accelerate in this way the action of the rest of (photo)catalysts. In other situations, Au NPs can be used to inject charges (electrons or holes) to another catalyst upon light irradiation, thereby activating a redox process in this second species.

This is the case of the example depicted in Figure 4.5A-B, where the reaction of H_2 generation from water is photocatalyzed by Au nanorods functionalized at their tips with Pt NPs (Pt@AuNR).²⁰ When exciting this system with visible and infrared light and

upon LSPR absorption by the Au nanostructures, the high-energy electrons generated are transferred and accumulated at Pt NPs, creating in this way a separation of charges in the photocatalyst. This activates the water reduction to H_2 over the Pt NPs, i.e. the desired process, whereas the electron-deficient Au surface oxidizes methanol molecules to regenerate the catalyst. It is important to notice that this effect requires the presence of the Pt co-catalyst, in the absence of which H_2 generation is not observed (Figure 4.5C).

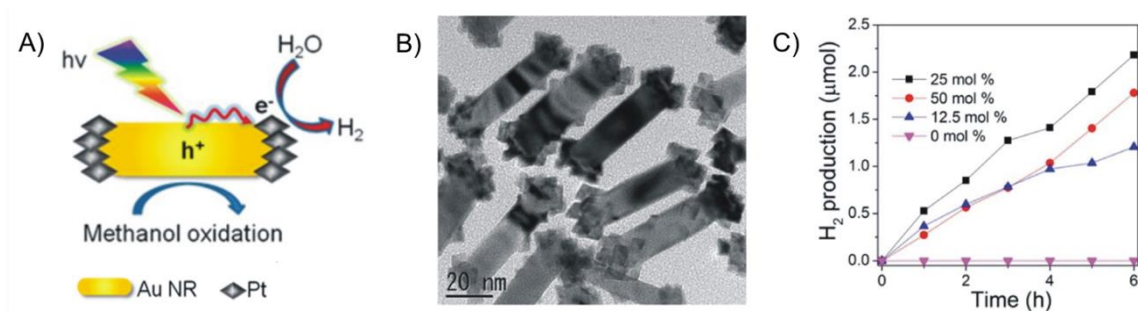


Figure 4.5. (A) H_2 generation in water:methanol mixtures at room temperature and under continuous irradiation with visible light at $\lambda = 460\text{-}820\text{ nm}$ in the presence of Au nanorods ($\sim 50\text{ nm}$ in length, $\sim 13\text{ nm}$ in diameter) functionalized at their extremes with pyramidal Pt NPs ($\sim 7\text{ nm}$ of edge) as photocatalysts. (B) TEM image of the photocatalyst used. (C) H_2 production under continuous irradiation for photocatalysts with different Pt content (0-25 mol %). Adapted from reference 20.

As illustrated by this example, the photocatalytic activity of Au NPs can be expanded to an even larger number of reactions by the combined use with other appropriate species. However, for the sake of simplicity, hereafter only those cases where the Au nanostructures act as direct photocatalysts will be considered.

4.1.3. Strategies of use

Despite their different nature, the three mechanisms described for the photocatalytic activity of Au NPs share a common feature: their effects are highly local and, as a result, they are only operative at nanometer-scale distances from the NPs.⁵⁻⁸ Consequently, maximal approach of the substrate molecules is required to attain optimal photocatalytic efficiencies. In order to fulfill this requirement, some strategies have been developed.⁵⁻⁸

The simplest of these strategies relies in the use of non-coated colloidal Au NPs, the so called “naked” Au NPs. In this case the approach of reactant molecules to the surface of the NPs is controlled just by diffusion processes. For instance, this strategy has been used by Scaiano *et al* in their photocatalytic studies of diverse chemical reactions,²¹ as it is the case of resazurin reduction in the presence of hydroxylamine to generate the fluorescent compound resorufin (Figure 4.6A).¹⁰ As observed in Figures 4.6B-C, the use of “naked” Au NPs of around 13 nm in diameter allowed this reaction to take place almost quantitatively, at room temperature and under visible light irradiation.

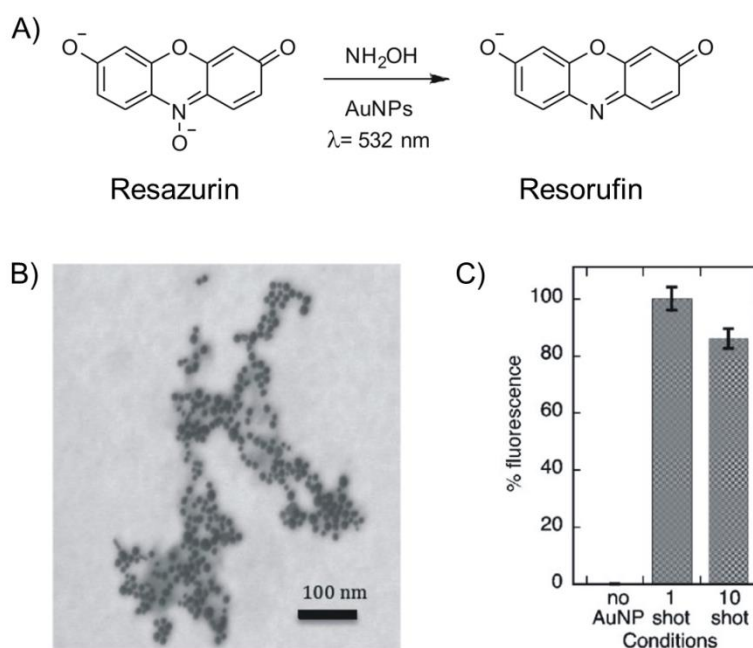


Figure 4.6. (A) Resazurin reduction to resorufin in the presence of hydroxylamine and Au NPs, at room temperature and under irradiation with pulsed green light at $\lambda = 532$ nm. (B) TEM image of the ~13 nm in diameter Au NPs used in this study. (C) Conversion of the reduction reaction in the absence of the photocatalyst (no Au NP), and in the presence of Au NPs with variable number of laser shots of green light. Conversion of the process is expressed as the relative fluorescence enhancement measured with respect to 100 % resorufin. Adapted from reference 10.

Although the absence of stabilizing ligands around Au NPs allows maximal approach of reactant molecules to the NP surface, this strategy implies a great disadvantage: the low stability of “naked” NPs towards aggregation, which normally hampers their separation from the reaction mixture and further recycling. To solve this problem, a different methodology has been developed. It consists in depositing the

“naked” Au NPs over some inert support. This is the case of SiO₂-supported Au NPs (AuNP@SiO₂) that were used to catalyze the amidation reaction between benzaldehyde and morpholine promoted by visible light (Figure 4.7A-B).¹⁶ As shown in Figure 4.7C, this reaction took place selectively and almost quantitatively at room temperature thanks to the photocatalytic effect of the plasmonic nanostructures employed, which allowed a 4-fold conversion increase compared to the situation where no irradiation was applied. Moreover, since a solid support was used to stabilize the photoactive Au NPs, the catalyst could be reused several times without any significant loss of its efficiency.

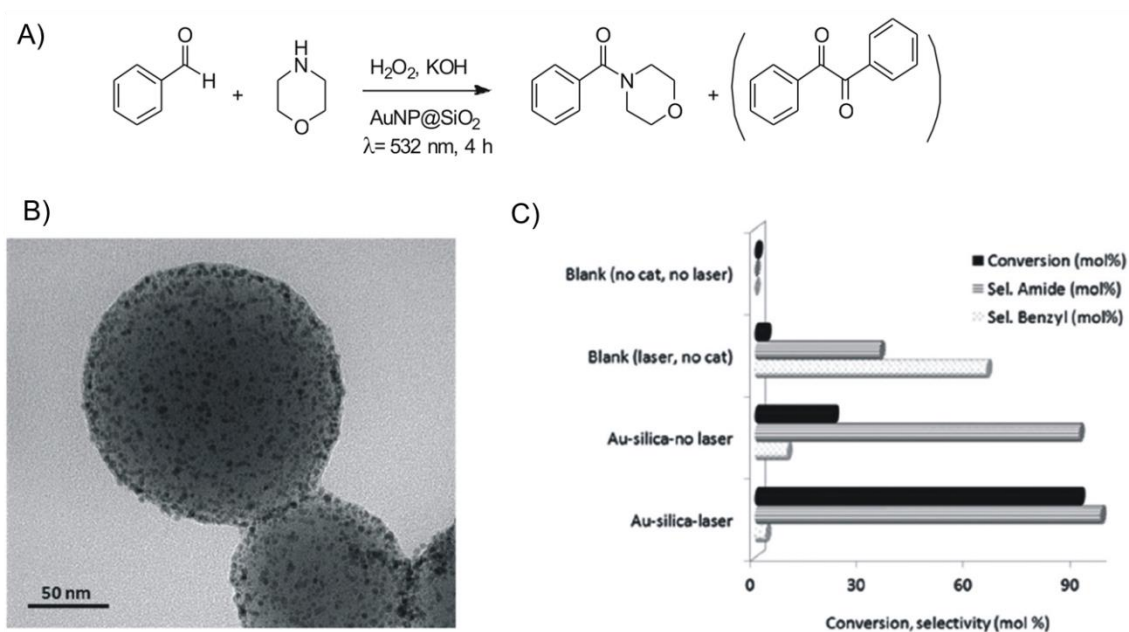


Figure 4.7. (A) Amidation reaction between benzaldehyde and morpholine photocatalyzed by AuNP@SiO₂ at room temperature and under continuous irradiation with green light at $\lambda = 532$ nm. The conditions employed can result in the formation of benzil as a by-product. (B) TEM image of the photocatalyst used, consisting in ~2 nm-in-diameter Au NPs supported over ~150 nm-in-diameter SiO₂ NPs. (C) Conversion and selectivity of the amidation reaction in the absence and presence of photocatalyst and irradiation. Adapted from reference 16.

In spite of its advantages, the anchoring of Au NPs to inert supports decreases the amount of catalytic surface which is exposed to the reaction medium compared to that of freely standing colloidal NPs, and therefore, it should conduct to lower catalytic activities per weight of catalyst used. In addition, the approach of substrate molecules to the photocatalytic nanostructures still relies on diffusion from solution, even though physisorption of the reactant molecules onto the support and, as such, local increase of reagent concentration around Au NPs may take place.

An alternative strategy which allows further minimizing the separation between reactant molecules and Au NPs, and, therefore, optimizing photocatalytic efficiency consists in directly linking the substrate molecules to the particle surface. To achieve this objective, these molecules must present terminal groups that assure their chemisorption over Au NPs prior to the photocatalytic process. An example of this methodology was described by Branda *et al*, who tethered a thiolated fluorescein derivative to colloidal Au NPs through a linker that comprised a furan-maleimide Diels-Alder cycloadduct (Figure 4.8A-B).¹³ When irradiating this system with visible light, the heat generated by PTE induced the dissociation process of the cycloadduct via a thermal retro-Diels-Alder reaction, thus releasing fluorescein units to the surrounding medium with great efficiency (Figure 4.8A,C). In this case, however, and in contrast to the strategies where reactants approximate to Au NPs by diffusion, the scope of the process is very limited, since only the small amount of molecules initially anchored to Au NPs can be photoreacted.

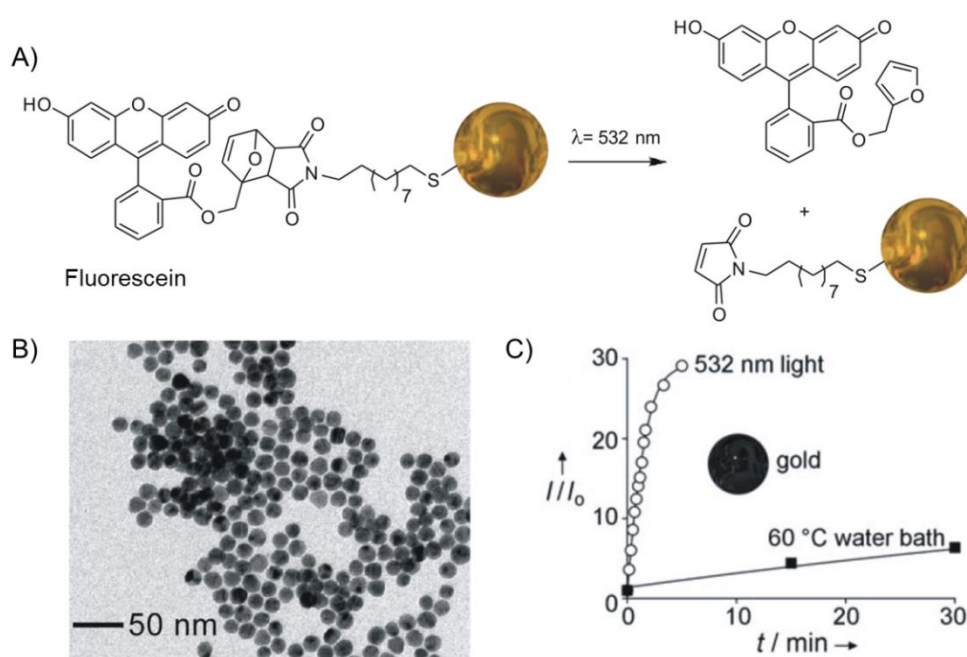


Figure 4.8. (A) Retro-Diels-Alder reaction of the furan-maleimide cycloadduct induced at room temperature by PTE upon irradiation with pulsed green light at $\lambda = 532 \text{ nm}$. This process releases the fluorescein chromophore initially chemisorbed over the photocatalyst, avoiding the quenching of emission by the nearby gold surface and resulting in fluorescence enhancement. (B) TEM image of the Au NPs used in this study ($\sim 16 \text{ nm}$ in diameter). (C) Time-evolution of the retro-Diels-Alder reaction under continuous irradiation with visible light, which can be monitored as a function of the fluorescence enhancement observed for the sample. As a reference, the behavior of the system in the absence of irradiation and under bulk heating to produce the thermal dissociation of the Diels-Alder cycloadduct is also represented. Adapted from reference 13.

4.1.4. Objectives: a new strategy for the use of Au NPs as photocatalysts based on supramolecular chemistry

In this chapter, a new methodology to enhance the photocatalytic activity of Au NPs is presented, which pursues increasing the efficiency with which the reactant molecules approach to the surface of the particles while overcoming the disadvantages of the strategies that have been described so far. To attain this objective, a novel strategy has been proposed herein that relies on functionalizing Au NPs with supramolecular hosts that are able to form labile host:guest complexes with the reactants (and products) of the process to be photocatalyzed. As shown in Figure 4.9, this should allow for: (i) promoting the approach of the reagent to the surface of Au NPs by formation of supramolecular complexes; (ii) warranting longer times of residence of the reactant molecules at the particle surface, thus favoring the photocatalytic reaction to be produced; (iii) continuous renewal of substrate molecules around the NP due to the lability of the complexes formed with reactants and products, thereby increasing the extent of the reaction; (iv) enhanced stability of Au NPs owing to the stabilizing nature of the chemisorbed supramolecular hosts, from which their separation and subsequent recycling should greatly benefit.

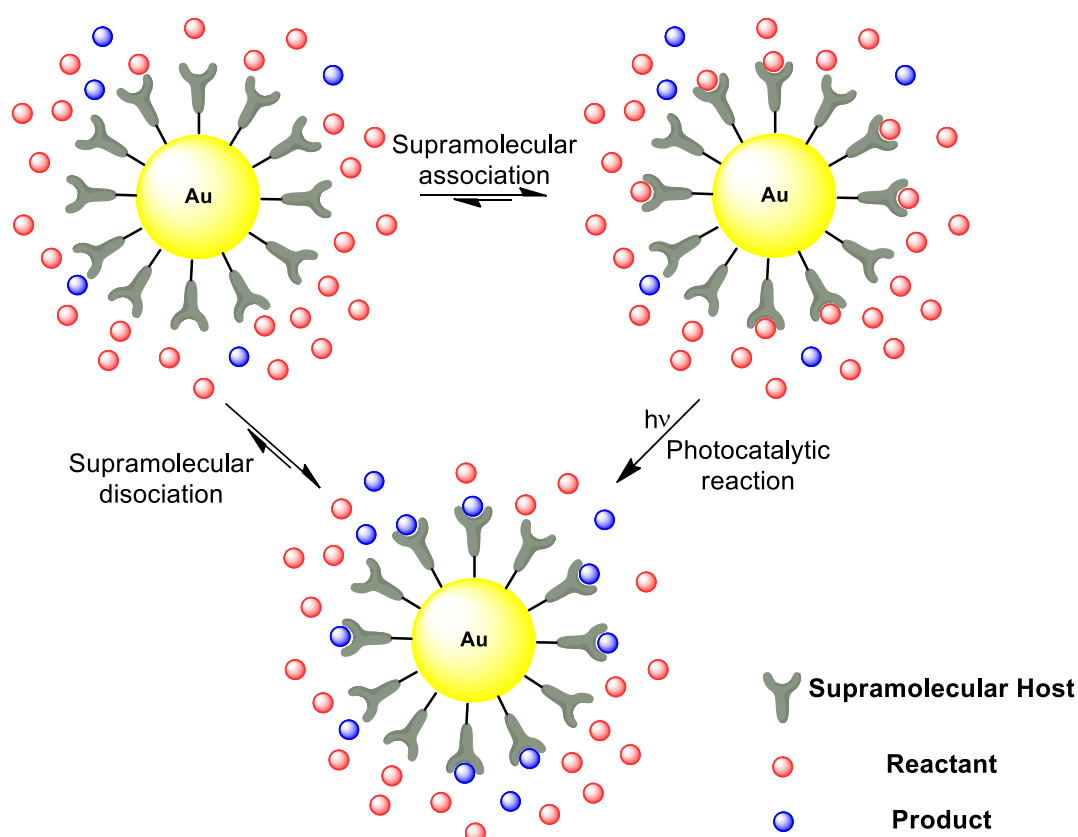


Figure 4.9. Schematic representation of the supramolecular approach developed to enhance the photocatalytic efficiency of Au NPs.

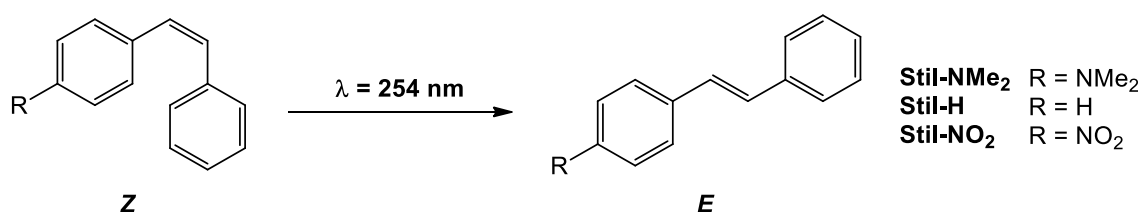
Cyclodextrins were found to be ideal hosts to carry out the supramolecular approach presented herein. As commented in chapter 3, they are able to supramolecularly interact with a wide variety of organic molecules in aqueous media with low-to-moderate association constants ($K_a < 10^4 \text{ M}^{-1}$), which can display different stoichiometries depending on the cyclodextrin member and the type of guest. As discussed in chapter 3, they are easy to functionalize for the obtaining of appropriate thiolated derivatives, enabling their anchoring onto the surface of Au NPs by means of Au-S bonds.

In order to test the applicability of the proposed approach, in the present thesis two types of reactions have been considered. Both unimolecular and bimolecular processes photocatalyzed by Au NPs were studied. For that, two different sets of Au NPs functionalized with cyclodextrin derivatives were prepared, and afterwards their photocatalytic performance under plasmon excitation was tested over selected benchmark reactions, as discussed in the following sections.

4.2. PHOTOCATALYSIS OF UNIMOLECULAR REACTIONS

In a first step, we explored the application of the supramolecular methodology outlined in the previous section to the enhancement of the photocatalytic activity of Au NPs in unimolecular reactions. With this aim, non-supported β -CD functionalized Au NPs were chosen as a photocatalytic system, since the dimensions of the inner cavity of this type of supramolecular host allow the formation of 1:1 inclusion complexes with low-to-moderate association constants (typically, $K_a < 10^4$) for a large number of organic molecules.²² Therefore, they are especially suited for supramolecularly-enhancing processes where a single molecule of reactants must interact with the catalyst. As a proof of concept, a simple unimolecular reaction was chosen to test the photocatalytic activity of β -CD functionalized Au NPs: the $Z \rightarrow E$ isomerization of stilbenes. The reasons for this choice were diverse. On the one hand, stilbenes are a relevant family of photoswitches²³ capable of supramolecularly interacting with CDs.²⁴ On the other hand, the direct photoswitching performance of most stilbene derivatives presents several downsides, some of which could be overcome by means of Au NP-based photocatalysis.²³ For instance, this is the case of the highly energetic UV light needed to induce $Z \rightarrow E$ isomerization (254 nm) and of the moderate interconversion yields usually obtained in this way. Finally, stilbene $Z \rightarrow E$ isomerization can take place thermally²⁵ or upon charge transfer,²⁶ which may therefore enable plasmon-based photocatalysis of this process via photothermal effects and/or hot charge carrier injection using Au NPs and visible light.

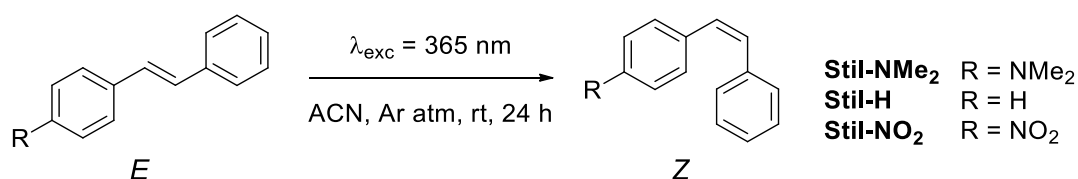
As shown in Scheme 4.1, three different commercially-available stilbene derivatives with differing electronic properties were selected for our photocatalytic studies: 4-dimethylaminostilbene (**Stil-NMe₂**), stilbene (**Stil-H**) and 4-nitrostilbene (**Stil-NO₂**). Since the thermodynamically stable isomer of these compounds corresponds to their *E* form, the synthesis of (*Z*)-**Stil-NMe₂**, (*Z*)-**Stil-H**, and (*Z*)-**Stil-NO₂** had to be first carried out, and this is the topic of the next section.



Scheme 4.1. *Z-E* isomerization of stilbenes, the selected unimolecular reaction to test supramolecularly-enhanced photocatalysis with β -CD-coated Au NPs.

4.2.1. Synthesis of (*Z*)-stilbenes

As can be seen in Scheme 4.2, the selected stilbene derivatives (*Z*)-**Stil-NMe₂**, (*Z*)-**Stil-H** and (*Z*)-**Stil-NO₂** were photochemically synthesized from their commercially available *E* counterparts. In particular, (*E*)-**Stil-NMe₂**, (*E*)-**Stil-H** and (*E*)-**Stil-NO₂** were photoisomerized in acetonitrile solution with a UV-lamp operating at $\lambda = 365$ nm and, after proper purification, their *Z* isomers were obtained in 44, 25 and 22 % yields, respectively. Irradiation was conducted under argon atmosphere, since the presence of molecular oxygen is known to lead to the irreversible formation of phenantrenes upon light-induced photocyclization of the freshly prepared (*Z*)-stilbenes.²⁷



Scheme 4.2. General procedure for the photochemical synthesis of (*Z*)-**Stil-NMe₂**, (*Z*)-**Stil-H**, and (*Z*)-**Stil-NO₂**.

Two main factors accounted for the low yields with which these compounds were prepared. On the one hand, even though the formation of phenantrene by-products was minimized at our experimental conditions, the intrinsic conversions of the photoisomerization of (*E*)-**Stil-NMe₂**, (*E*)-**Stil-H** and (*E*)-**Stil-NO₂** at $\lambda = 365$ nm were found not to be quantitative (< 80 %). This was due to the fact the both the *E* and *Z* isomers of these stilbene derivatives absorbed and photoisomerized at the irradiation wavelength. As such, competitive *E* → *Z* and *Z* → *E* isomerization processes simultaneously occurred upon illumination and, once the rates of these two processes became equal, an equilibrium state was achieved. This state is called photostationary state (PSS), the composition of which depends on the absorptivity of each isomer at the irradiation wavelength and the corresponding photoisomerization quantum yield. As such, different PSS mixtures were obtained for each of the stilbene derivatives, which in all the cases contained a significant amount of the initial *E* isomer.

On the other hand, purification of the desired products was not straightforward due to the low solubility of the (*Z*)- and, specially, (*E*)-stilbenes of interest and their high sensitivity to ambient light. Actually, only in the case of (*Z*)-**Stil-H**, this product could be isolated by successive flash column chromatographies. By contrast, other purification methods had to be applied for (*Z*)-**Stil-NMe₂** and (*Z*)-**Stil-NO₂**, the best of which turned

to be repetitive fractional precipitation in *n*-hexane, a process that benefited from the extremely low solubility of their (*E*)-isomers. In this way, only *Z*-enriched mixtures of both stereoisomers could be obtained, the *Z*:*E* molar ratio of which was determined to be 98:2 (**Stil-NMe₂**) and 97:3 (**Stil-NO₂**) by NMR spectroscopy. These samples and (*Z*)-**Stil-H** were characterized by ¹H and ¹³C NMR, and they were found to be stable for months when stored in the dark and at low temperatures.

4.2.2. Host-guest supramolecular interaction between β-CD and stilbenes

After preparation of the substrate molecules for our photocatalytic experiments, we characterized the supramolecular interaction between both the *Z* and *E* isomers of **Stil-NMe₂**, **Stil-H** and **Stil-NO₂** with β-CD, the host of choice. Since β-CD-stilbene complexes are mainly driven by hydrophobic effects, this study was performed in aqueous media. However, because of the insolubility of β-CD-(**SH**)₇ at the range of concentrations needed, such characterization was carried out with pristine β-CD. There are different methods available on the literature that allow the association constant (*K_a*) of a given host:guest pair to be determined. All of them are based on the variation of an experimental parameter upon host:guest association (or dissociation), such as chemical shift,²⁸ absorbance,²⁹ fluorescence,³⁰ enthalpy,³¹ etc. According to the properties of the systems under study and the available instrumentation, it was decided to determine the *K_a* values for β-CD-stilbene complexes by means of optical measurements.

By simplicity, determination of the desired *K_a* values by UV-Vis spectroscopy was first attempted.²⁹ Unfortunately, no variation of the absorbance of the (*E*)- and (*Z*)-stilbenes of interest was observed upon addition of increasing amounts of β-CD, which prevented characterization of their supramolecular association. On the contrary, preliminary fluorescence experiments demonstrated that the emission of both isomers of **Stil-NMe₂**, **Stil-H** and **Stil-NO₂** did vary upon interaction with β-CD. For this reason, we applied a reported methodology to determine the association constants of β-CD and stilbenes by means of fluorescence spectroscopy.³² This methodology assumes a 1:1 stoichiometry for the β-CD-stilbene complexes, the *K_a* value of which can then be obtained from the fluorescence enhancement (or quenching) (*F*/*F*₀) observed as a function of the concentration of β-CD added to a solution of constant concentration of stilbene:³²

$$F/F_0 = 1 + (F_\infty/F_0 - 1) \frac{[CD]_0 K_a}{1 + [CD]_0 K_a} \quad (4.1)$$

In this expression F is the fluorescence intensity in the presence of β -CD for a certain β -CD-stilbene mixture, F_0 is the fluorescence intensity in the absence of β -CD, and F_∞ is the fluorescence intensity when all guest molecules are complexed (i.e. at infinite concentration of β -CD). Fitting the experimental fluorescence values to this equation provided the K_a value of the corresponding β -CD-stilbene complex. An example of such determination for (*Z*)-**Stil-H** is depicted in Figure 4.10. Table 4.1 shows the association constant values found for all stilbene derivatives investigated.

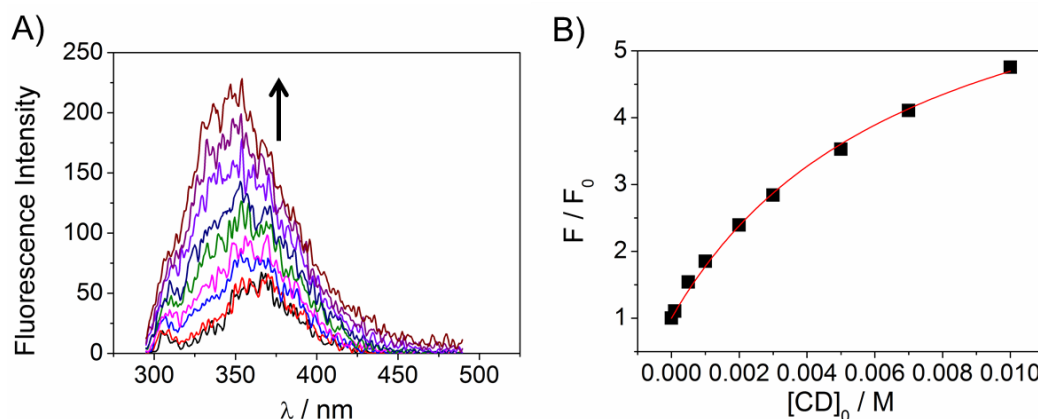


Figure 4.10. A) Variation of the fluorescence emission of (*Z*)-**Stil-H** in water:acetonitrile 94:6 upon addition of increasing amounts of β -CD (from 0 to 0.01 M). B) Plot of the fluorescence enhancement factor against the β -CD concentration added in (A). Black dots correspond to the experimental F/F_0 values, while the red line corresponds to the fitting to equation 4.1, which provided a K_a value of $140 \pm 13 \text{ M}^{-1}$ for the β -CD:(*Z*)-**Stil-H** association complex.

Because of the limited solubility of stilbenes in aqueous media, K_a determination was not carried out in pure water, but in acetonitrile:water mixtures. Actually, this was also the case for the photocatalytic experiments that were later on performed, where 94:6 water:acetonitrile was used as a solvent. Accordingly, we decided to measure the association constants for β -CD:stilbene complexes in the same medium, as shown in Table 4.1. Unfortunately, owing to the very low solubility in water of the (*E*)-stilbenes under investigation, their K_a values could not be determined at these conditions. Instead, a solvent mixture with a larger content of acetonitrile had to be used (water:acetonitrile 75:25). For this reason, β -CD:(*Z*)-stilbene K_a values were measured

in both media, which demonstrated that host-guest association constants decreased in ca. 85 % for (*Z*)-**Stil-NMe₂**, 70 % for (*Z*)-**Stil-H** and 76 % for (*Z*)-**Stil-NO₂** when increasing acetonitrile concentration. This allowed rough estimates of β -CD-(*E*)-stilbene K_a values in water:acetonitrile 94:6 to be made for the same compounds, as shown in Table 4.1.

Table 4.1. Association constants determined for the supramolecular complexes formed between β -CD and the *Z* and *E* isomers of **Stil-NMe₂**, **Stil-H** and **Stil-NO₂**.

Compound	K_a (<i>Z</i> isomer) / M ⁻¹		K_a (<i>E</i> isomer) / M ⁻¹	
	Water:acetonitrile	Water:acetonitrile	Water:acetonitrile	Water:acetonitrile
	94:6	75:25	75:25	94:6 ^{a)}
Stil-NMe₂	1783 ± 265	291 ± 64	1306 ± 321	8000
Stil-H	140 ± 13	44 ± 14	190 ± 58	600
Stil-NO₂	106 ± 19	25 ± 6	48 ± 14	200

^{a)} Estimated from K_a (*Z* isomer) values.

As can be seen in Table 4.1 all the stilbene derivatives studied were able to form supramolecular host-guest complexes with β -CD. The highest association constant values were found for **Stil-NMe₂**, being one order of magnitude higher than those found for **Stil-H** and **Stil-NO₂**. Probably the existence of *H*-bonds between the secondary hydroxyls at the exterior of the CD and the stilbene substituent plays an important role. However, if that was the case, we would have expected **Stil-NO₂** to have an even higher K_a value. It must be noticed that *Z*-stilbenes showed smaller association constants than *E*-stilbenes, probably because the latter fit better inside the CD cavity than the corresponding *Z* isomers, but this should not interfere in the photocatalytic process, since K_a values are small enough in all cases as to assume that rather labile complexes would be formed assuring a continuous renewal of substrate molecules around Au NPs.

4.2.3. Preparation and characterization of β -CD-coated Au NPs

As previously commented, the system devised to validate the proposed supramolecular approach towards Au NP-based photocatalysis of unimolecular

reactions consisted in gold nanoparticles functionalized with β -CD-(SH)₇. Aside from its interesting supramolecular properties already discussed, the choice of this type of host was also driven by the fact that it attaches to the nanoparticle surface via multiple sulfur bonds, which should provide the coated Au NPs with sufficient stability as to sustain long irradiation times and various photocatalytic cycles without requiring the use of supports. Actually, the photostability of β -CD-(SH)₇-functionalized Au NPs was already demonstrated in chapter 3, especially for nanostructures presenting relatively small sizes (diameter < 20 nm).

Based on this result and aiming at procuring good quality nanoparticles for the photocatalytic experiments, we conducted their synthesis via ligand exchange from citrate-stabilized Au NPs previously prepared by the Turkevich-Frens method. Namely, the procedure described in detail in section 3.3.2 was employed to obtain a new batch of **AuNP-TF@ β CD** (**AuNP-TF@ β CD3** from hereafter), for which a citrate:gold precursor ratio of 2.7 was used. This allowed the obtention of β -CD(SH)₇-coated Au NPs, which after light-induced disaggregation by laser pulsed irradiation at $\lambda = 532$ nm (70 mW) were found to present an average diameter of 14 ± 2 nm and a LSPR band centered at $\lambda = 523$ nm (Figure 4.11). As already described in chapter 3, the functionalization of the surface of these gold nanoparticles with β -CD(SH)₇ was confirmed by 1D DOSY ¹H NMR spectroscopy.

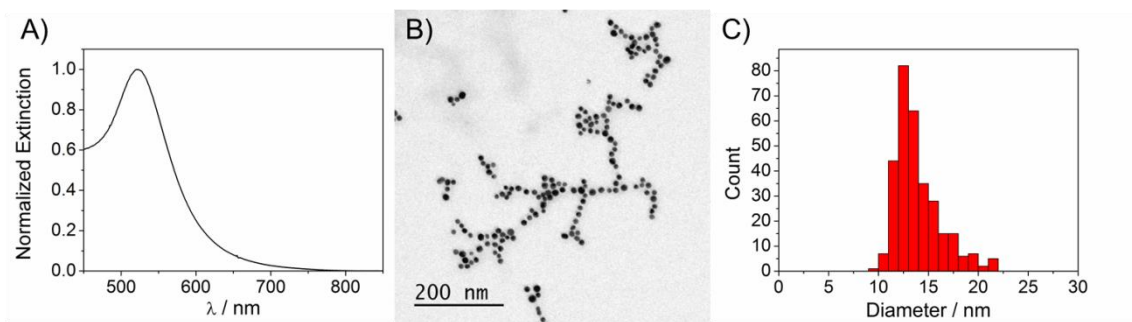
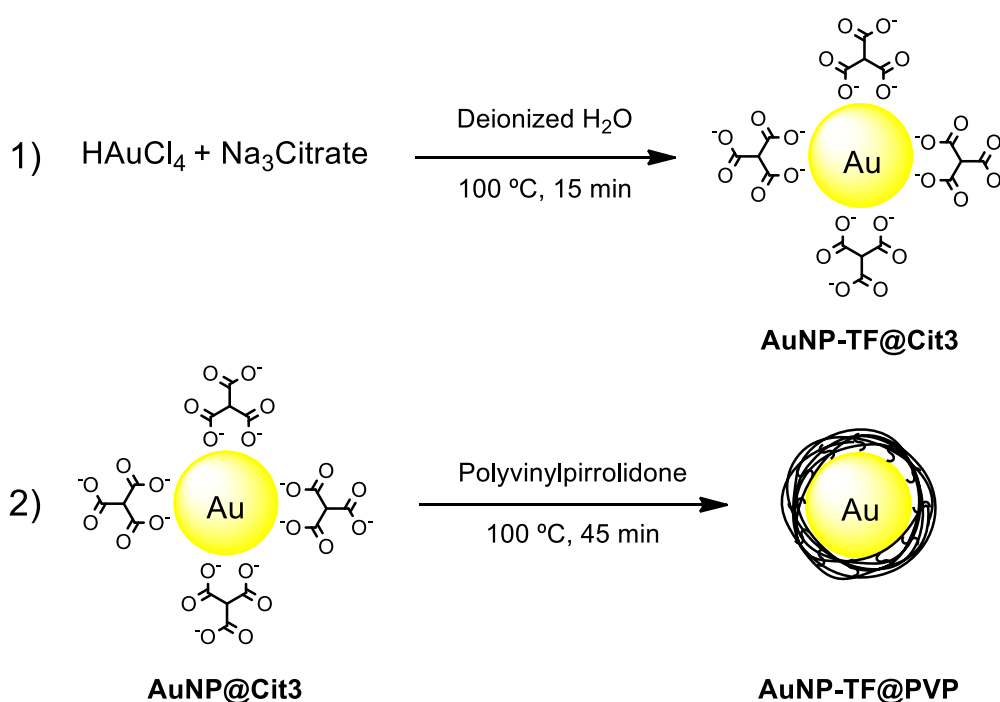


Figure 4.11. A) Extinction spectrum in water of **AuNP-TF@ β CD** after irradiation to induce particle disaggregation. B) TEM image of these nanoparticles, the size histogram of which is shown in C).

Although **AuNP-TF@ β CD3** was the photocatalyst of choice for our studies on (*Z*)-stilbene isomerization, an additional set of NPs was prepared. They consisted in polyvinylpyrrolidone (PVP) stabilized Au NPs (**AuNP-TF@PVP**) that were used to perform blank experiments during the photocatalytic measurements. For this reason,

they were coated with a continuous organic polymer layer with a thickness of the order of that of the β -CD layer around **AuNP-TF@ β CD3** (~0.8 nm).³³ As such, substrate molecules should be capable to reach **AuNP-TF@PVP** surface at similar distances as for **AuNP-TF@ β CD3** and, therefore, be subjected to comparable PTE-induced temperature increments upon irradiation. However, the lack of β -CD hosts in **AuNP-TF@PVP** should prevent supramolecularly-enhanced approach of the reactants as well as direct contact with the particle surface (e.g. for charge carrier injection).

AuNP-TF@PVP were also prepared by ligand exchange from the same batch of citrate-stabilized particles used for the synthesis of **AuNP-TF@ β CD3**, thus ensuring that both sets of samples presented similar sizes (Scheme 4.3).



Scheme 4.3. Two-step procedure for the preparation of **AuNP-TF@PVP** via citrate-stabilized Au NPs.

In this case, the ligand exchange process was done right after the reduction of HAuCl_4 had taken place and Au NPs had been formed. Without stopping the heating source, the proper amount of a 0.2 mg/mL polyvinylpyrrolidone solution in water was then added and the mixture was allowed to boil for an additional period, during which time the PVP molecules wrapped around the surface of citrate-stabilized Au NPs. With this procedure, the final Au NPs displayed capping layers with varying thicknesses depending on the amount of PVP added to the colloidal dispersion. For this reason,

preliminary experiments were undertaken in order to tune the thickness of the PVP layer and reach the target value for **AuNP-TF@PVP** (~ 1 – 1.5 nm). The final particles were characterized by UV-vis absorption spectroscopy and TEM, and they displayed similar properties to those of **AuNP-TF@ β CD3** ($\lambda_{\text{LSPR}} = 524$ nm, average diameter = 15 ± 2 nm, Figure 4.12).

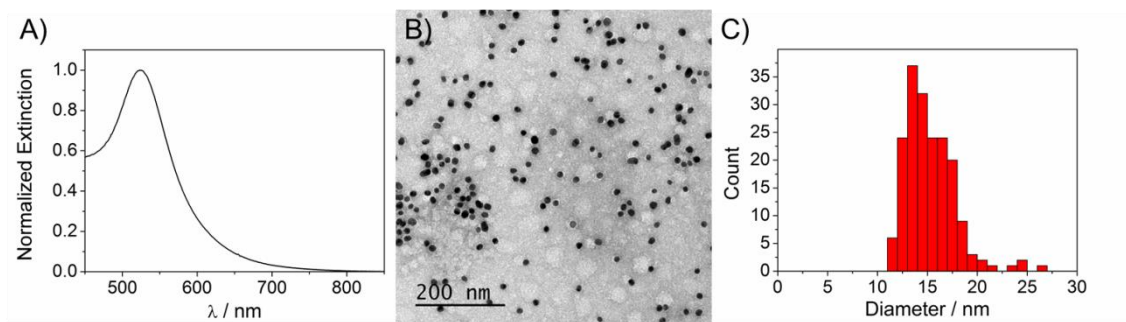


Figure 4.12. A) Extinction spectrum in water of **AuNP-TF@PVP**. B) TEM image of these nanoparticles, the size histogram of which is shown in C).

In what regards to their PVP shell, **AuNP-TF@PVP** presented a 1.4 nm thick capping layer as evidenced by TEM analysis under negative staining with uranium acetate (Figure 4.13). Such technique consists in the application of an uranium acetate solution directly onto the copper grid where the sample of interest was previously deposited. After removal of the excess solution, positive or negative staining may occur increasing the contrast of certain structures of the sample where uranium acetate has adsorbed (in our case, onto the carbon grid), and therefore allowing for their visualization under regular TEM conditions.

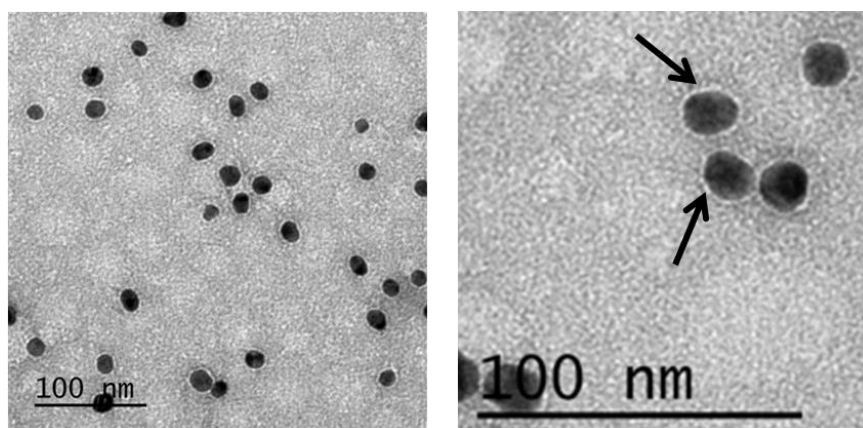


Figure 4.13. A) Representative TEM image of **AuNP-TF@PVP**, where sample negative staining with uranium acetate allows visualization of the organic shell. The black arrows in the right image point towards the PVP shell of two different Au NPs.

4.2.4. Photochemical and thermal isomerization of stilbenes

Prior to conducting the photocatalytic isomerization of stilbenes in the presence of Au NPs under visible light irradiation, it was decided to carry out control experiments of the pure photochemical and thermal $Z \rightarrow E$ and $E \rightarrow Z$ isomerization of **Stil-NMe₂**, **Stil-H** and **Stil-NO₂** in the same medium (water:acetonitrile 94:6). The obtained values served to compare the performance of our subsequent photocatalytic experiments using Au NPs and, more importantly, to select the particular stilbene derivative that was finally submitted to an exhaustive photocatalytic study.

(a) Photochemical isomerization of stilbenes

As was commented at the beginning of this section, the photochemical isomerization of stilbenes takes place at rather energetic frequencies and with non-quantitative yields due to the obtention of photostationary states. This is due to the fact that both stereoisomers of these compounds typically absorb in the same UV region of the spectrum, as shown in Figure 4.14 for **Stil-NMe₂**, **Stil-H** and **Stil-NO₂**. Based on this data, $Z \rightarrow E$ photoisomerization for these compounds was induced by irradiation at 254 nm, while $E \rightarrow Z$ photoisomerization was investigated by irradiation at 365 nm. After illumination, the photoisomerization conversions were determined by comparison of the UV-vis absorption spectra of the PSS mixtures with those of the pure Z and E isomers (Scheme 4.3). In all the cases, experiments were conducted in argon atmosphere to prevent the formation of phenantrene derivatives, as already discussed.

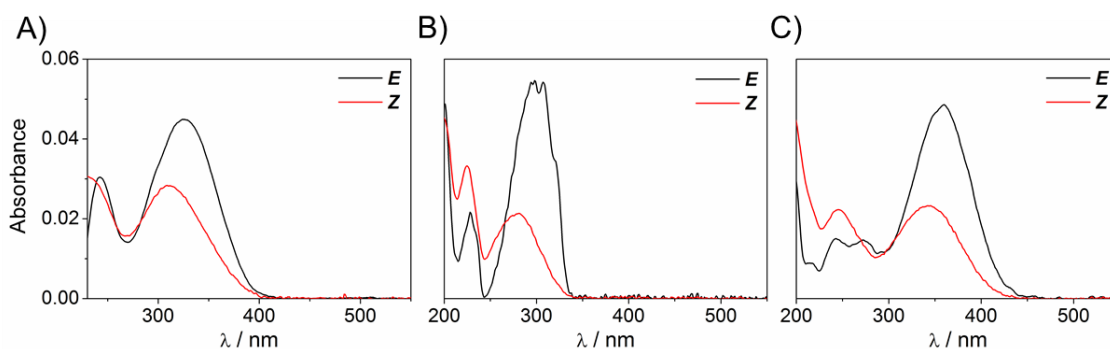
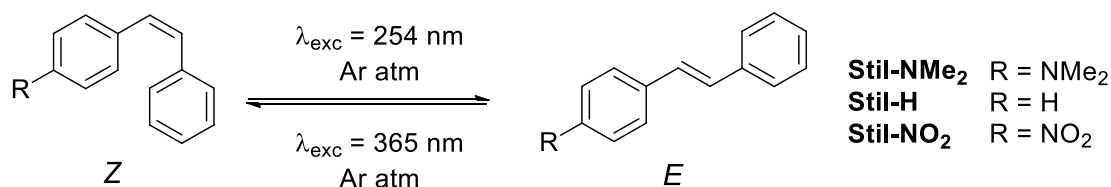


Figure 4.14. Absorption spectra in water:acetonitrile 94:6 of both stereoisomers of: A) **Stil-NMe₂** ($c = 2 \cdot 10^{-6}$ M); B) **Stil-H** ($c = 2 \cdot 10^{-6}$ M); C) **Stil-NO₂** ($c = 2 \cdot 10^{-6}$ M).



Scheme 4.3. Photochemical $Z \rightarrow E$ and $E \rightarrow Z$ isomerization of **Stil-NMe₂**, **Stil-H** and **Stil-NO₂** under UV irradiation at $\lambda = 254 \text{ nm}$ and 365 nm , respectively.

As can be seen in Table 4.2, moderate conversion yields were obtained in the case of the $Z \rightarrow E$ isomerization of **Stil-NMe₂**, **Stil-H** and **Stil-NO₂** under irradiation at 254 nm , which lay below 65 %. By contrast, much higher conversion values were found for the opposite process when irradiating E -stilbenes at 365 nm , with a maximum value of 92 % obtained for (E)-**Stil-H**. As expected, quantitative photoisomerization was therefore observed in none of these cases.

Table 4.2. Photoisomerization conversions (%) of **Stil-NMe₂**, **Stil-H** and **Stil-NO₂** upon direct UV irradiation in water:acetonitrile 94:6.

Compound	$Z \rightarrow E^{\text{a}}$	$E \rightarrow Z^{\text{b}}$
Stil-NMe₂	41	83
Stil-H	48	92
Stil-NO₂	64	68

^{a)} Irradiation at 254 nm . ^{b)} Irradiation at 365 nm .

b) Thermal isomerization of stilbenes

Concerning the thermal isomerization of **Stil-NMe₂**, **Stil-H** and **Stil-NO₂**, several experiments were carried out. First of all, isomerization of these compounds was investigated in deuterated water:acetonitrile 94:6 at 373 K , the highest temperature that could be achieved at ambient pressure. As shown in Table 4.3, only (Z)-**Stil-NMe₂** underwent isomerization at these conditions with 10 % conversion, whereas no reaction were observed for neither (E)-**Stil-NMe₂** nor both isomers of the rest of stilbenes. To unravel supramolecular and/or catalytic effects on the bulk thermal isomerization of these compounds, further controls were conducted upon addition of β -CD and **AuNP-TF@ β CD3** to the stilbene samples at the same concentrations as in the

photocatalytic experiments (see below). The presence of β -CD had no effect over the thermal stilbene isomerization, but the presence of Au NPs increased (*Z*)-**Stil-NMe₂** and (*Z*)-**Stil-NO₂** conversion up to 26 and 29 %, respectively (Table 4.3). The latter results, however, were affected by the rapid degradation found for **AuNP-TF@ β CD3** upon bulk heating, which might have produced highly active gold catalytic species accounting for stilbene isomerization in the dark.

Table 4.3. Thermal isomerization conversions (%) of **Stil-NMe₂**, **Stil-H** and **Stil-NO₂** upon bulk heating.^{a)}

T (K)	Solvent	β -CD	AuNP-TF@ β CD3	Z \rightarrow E			E \rightarrow Z		
				Stil-NMe ₂	Stil-H	Stil-NO ₂	Stil-NMe ₂	Stil-H	Stil-NO ₂
373	D ₂ O:CD ₃ CN	No	No	10	0	0	0	0	0
373	D ₂ O:CD ₃ CN	Yes	No	12	0	0	0	0	0
373	D ₂ O:CD ₃ CN	No	Yes	26	0	29	0	0	0
373	DMSO- <i>d</i> ₆	No	No	2	0	2	0	0	0
423	DMSO- <i>d</i> ₆	No	No	99	2	3	0	0	0

^{a)} Experiments conducted in deuterated water:acetonitrile 94:6 under reflux (~373 K) for 2 h and in DMSO-*d*₆ for 30 min (423 K). $c_{\beta\text{-CD}} = 15 \mu\text{M}$. $c_{\text{AuNP-TF@}\beta\text{CD3}} = 45 \text{ nM}$.

In an attempt to increase thermal isomerization conversions of stilbene derivatives, additional experiments were conducted in DMSO-*d*₆, which allowed reaching higher heating temperatures. While nearly no conversions were observed at 373 K, almost quantitative isomerization was observed for (*Z*)-**Stil-NMe₂** by heating at 423 K during 30 minutes in DMSO-*d*₆; on the contrary, negligible conversion was observed for (*Z*)-**Stil-H** and (*Z*)-**Stil-NO₂** at these conditions (Table 4.3). In what regards to thermal *E* \rightarrow *Z* isomerization, no effect was observed for any of the compounds assayed.

For better understanding the thermal *Z* \rightarrow *E* conversion measured for (*Z*)-**Stil-NMe₂** in water:ACN and DMSO at 373 and 423 K, it was decided to investigate its isomerization kinetics at these conditions (Figure 4.15). Clearly, a logarithmic first-order reaction rate was not found in any of the experiments performed, in contrast to what is expected for this simple unimolecular reaction. Instead, an induction period with

negligible conversion was first observed in both cases ($t = 0$ -100 min and 0-15 min, respectively), which was then followed by a sudden rise of the reaction rate ($t > 100$ min and 15 min, respectively). Although the actual mechanism accounting for this behavior is not currently clear, it unambiguously indicated that, at these conditions, the reaction proceeded through a multistep process requiring the formation of a thermally activated species. This means that the simple unimolecular mechanism of $Z \rightarrow E$ isomerization of (*Z*)-**Stil-NMe₂** did not take place at such temperatures, in agreement to (*Z*)-**Stil-H** and (*Z*)-**Stil-NO₂** and, as will be discussed below, to theoretical calculations (see section 4.2.6).

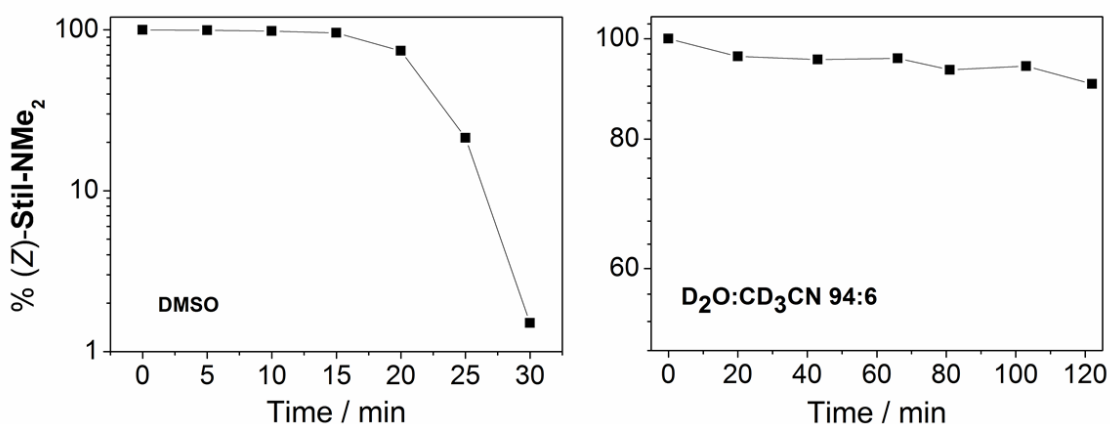


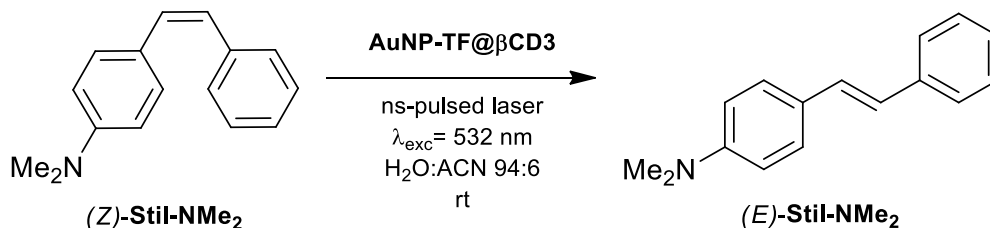
Figure 4.15. $Z \rightarrow E$ isomerization kinetics of (*Z*)-**Stil-NMe₂** in the absence of AuNPs and upon bulk heating at 423 K in DMSO-*d*₆ and at ~373 K in D₂O:CD₃CN 94:6.

In spite of this, our thermal experiments demonstrated that (*Z*)-**Stil-NMe₂** was the stilbene derivative of choice more prone to undergo temperature-induced isomerization. This, in combination with its ~10-fold larger association constant with β -CD with respect to (*Z*)-**Stil-H** and (*Z*)-**Stil-NO₂**, made us select (*Z*)-**Stil-NMe₂** as the benchmark system to validate the new supramolecular approach to plasmon-based photocatalysis presented in this work.

4.2.5. Photocatalytic studies with gold nanoparticles

As has been discussed all along this chapter, Au NPs can effectively act as photocatalysts in a wide variety of chemical reactions. The aim herein was to demonstrate that a new strategy based on supramolecular host-guest chemistry could

increase their efficiency towards selected reactions. To explore this strategy, the $Z \rightarrow E$ isomerization of (*Z*)-**Stil-NMe₂** in the presence of β -CD-functionalized Au NPs was first considered in detail (Scheme 4.4), although photocatalytic experiments were later on expanded to (*Z*)-**Stil-H** and (*Z*)-**Stil-NO₂**.



Scheme 4.4. Regular experimental conditions of the photocatalytic isomerization of (*Z*)-**Stil-NMe₂** in the presence of **AuNP-TF@ β CD3**.

Unless otherwise specified, photocatalytic experiments with (*Z*)-**Stil-NMe₂** and **AuNP-TF@ β CD3** were performed at room temperature, in water:acetonitrile 94:6 and under ns-pulsed laser irradiation at 532 nm, with variable excitation powers and illumination times. It must be noticed that neither (*Z*)-**Stil-NMe₂** nor the rest of *Z*- and *E*-stilbenes considered in this work absorbed at this frequency, as previously shown in Figure 4.15. Therefore, any photoreactivity observed could be ascribed to plasmon excitation of gold nanoparticles with visible light. After irradiation, samples were treated to eliminate the solvent and Au NPs, and the extent of $Z \rightarrow E$ isomerization was determined by ¹H NMR analysis of the resulting crude. On the other hand, colloidal suspensions of Au NPs were irradiated at 100 mW (10 mJ/pulse) for 30 minutes prior to the addition of the reactant molecules in our photocatalytic experiments. This induced disassembly of the Au NP aggregates formed during the ligand exchange and/or purification process and attributed to H-bonding between CD molecules (see section 3.3.2 in chapter 3). All blank samples for control experiments were pre-treated in the same way (100 mW, 30 min) before the addition of the reactant molecules. Next, results are discussed for all the variety of photocatalytic experiments that were performed.

a) Preliminary control experiments

First of all, control isomerization experiments were conducted for (*Z*)-**Stil-NMe₂** in the absence of laser irradiation, Au NPs or both. As can be seen in Figure 4.16, minimal $Z \rightarrow E$ conversion values below 6 % were obtained in all cases. On the one hand, this proved thermal and photochemical stability of (*Z*)-**Stil-NMe₂** at our

photocatalytic conditions, since it negligibly isomerized in the absence of catalyst both in the dark and under irradiation. In addition, no significant conversion was also observed in the presence of **AuNP-TF@ β CD3** at 45 nM concentration without laser irradiation, which demonstrated that Au NPs (or β -CD) did not isomerize (*Z*)-**Stil-NMe₂** if plasmon excitation did not occur. Importantly, this is in contrast to the behavior of (*Z*)-azobenzenes, the isomerization of which was found to be catalyzed by Au NPs even in the dark.³⁴

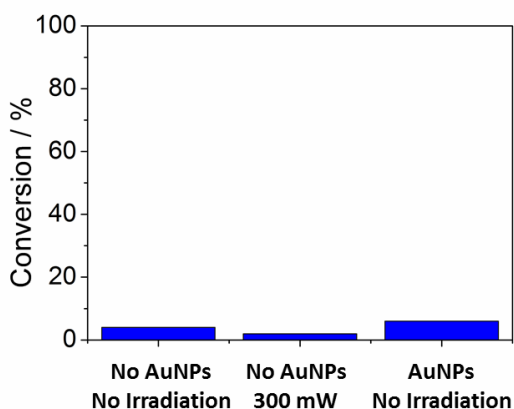
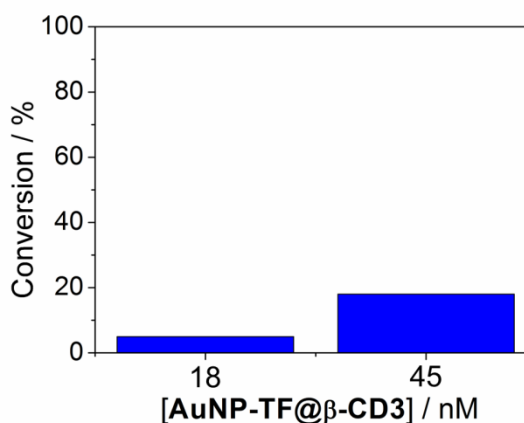


Figure 4.16. Conversion values determined in control experiments for the *Z* → *E* isomerization of (*Z*)-**Stil-NMe₂** after 2 hours: (i) in the absence of catalyst and irradiation (4 %); (ii) in the absence of catalyst and upon irradiation with pulsed laser light at 532 nm and 300 mW (2 %) and (iii) in the presence of 45 nM **AuNP-TF@ β CD** and without irradiation (6 %).

b) Effect of photocatalyst concentration

Once the photostability of (*Z*)-**Stil-NMe₂** had been proven according to the results obtained in the control experiments shown above, the effect of the amount of photocatalyst was investigated. Photocatalytic experiments of (*Z*)-**Stil-NMe₂** isomerization with a 18 nM suspension of **AuNP-TF@ β CD3** and under irradiation with pulsed laser light at 532 nm and 300 mW power for 30 minutes provided the same minor conversion (6 %) as observed in control experiments. Surprisingly, raising the concentration of the photocatalyst up to 45 nM resulted in a 3-fold increase in conversion (18 %) under the same illumination conditions, as shown in Figure 4.17. Therefore, this result uncovered the feasibility of inducing (*Z*)-**Stil-NMe₂** isomerization under Au NP photocatalysis.

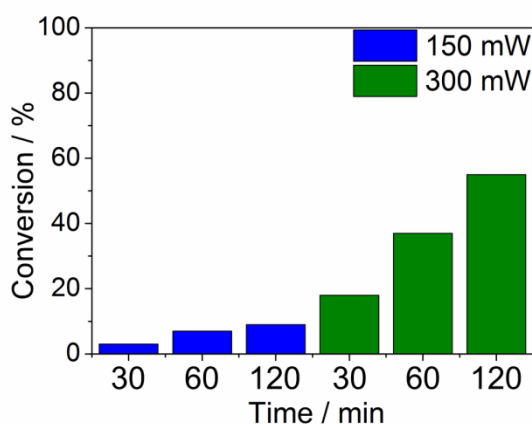
Figure 4.17. Conversion values determined for the photocatalytic $Z \rightarrow E$ isomerization of (*Z*)-**Stil-NMe₂** in the presence of two different concentrations of **AuNP-TF@ β CD3**: 18 nM (6 %) and 45 nM (18 %). Pulsed laser irradiation took place at 532 nm and 300 mW during 30 minutes.



c) Power and time dependence of photocatalytic activity

After the encouraging results obtained at high concentrations of **AuNP-TF@ β CD3**, it was decided to explore in more detail the time and power dependence of the photocatalytic process, thus aiming to maximize the isomerization conversion. As depicted in Figure 4.18, either extending the irradiation time or increasing the irradiation power enhanced the efficiency of the $Z \rightarrow E$ isomerization reaction of (*Z*)-**Stil-NMe₂**. Thus, conversion values of 5, 11 and 16 % were obtained when irradiating this compound in the presence of Au NPs (45 nM) at 150 mW of 532 nm-pulsed laser light during 30, 60 and 120 minutes, respectively. These values underwent a 3-fold increase when the excitation power was raised to 300 mW, affording $Z \rightarrow E$ conversions of 18, 37 and 56 % for the 30, 60 and 120 minutes experiments, respectively. Unfortunately, longer irradiation times did not improve these yields, while fast **AuNP-TF@ β CD3** degradation was observed at higher powers (600 mW).

Figure 4.18. Conversion values determined for the photocatalytic $Z \rightarrow E$ isomerization of (*Z*)-**Stil-NMe₂** in the presence of **AuNP-TF@ β CD3** (45 nM) upon irradiation with 532 nm-pulsed laser light at different conditions: 150 mW during 30 (5 %), 60 (11 %) and 120 minutes (16 %), and 300 mW during 30 (18 %), 60 (37 %) and 120 minutes (56 %).



Two main conclusions could be drawn from these results and those shown in the previous section. First of all, the dependence observed for the reaction conversion with **AuNP-TF@ β CD3** concentration and irradiation conditions clearly demonstrated that $Z \rightarrow E$ isomerization of (*Z*)-**Stil-NMe₂** could be photocatalyzed upon plasmon excitation, as targeted in this work. Second, the highest conversion yield achieved under Au NP-based photocatalysis with visible light (56 %) notably enhanced the results obtained upon direct excitation of (*Z*)-**Stil-NMe₂** with UV radiation (41%), thus improving some of the downsides of the photochemical performance of this system. Actually, the best of our photocatalytic results accomplished at 300 mW irradiation with 532-nm pulsed laser for 120 min was reproduced with high accuracy (less than 5% standard deviation) in repetitive experiments conducted with the same and other batches of ~15-nm-in-diameter **AuNP-TF@ β CD3**.

In regards of the highest conversion values achieved, a possible explanation would be that some sort of photostationary state was reached as in the case of stilbene isomerization with UV light. To rule out this possibility, an experiment at the best photocatalytic conditions (45 nM catalyst concentration, 300 mW and 2 h) involving (*E*)-**Stil-NMe₂** were carried out. No $E \rightarrow Z$ isomerization was found in this assay, evidencing the absence of any photostationary state under plasmon excitation. Even though we cannot explain why higher conversion values could not be achieved, what it became clear was **AuNP-TF@ β -CD3** were able to selectively catalyze the $Z \rightarrow E$ isomerization process, contrary to what occurs when stilbenes are directly excited with UV light.

d) Effect of supramolecular host-guest association in plasmon-based photocatalysis

Once proven the photocatalytic activity of **AuNP-TF@ β CD3** in the isomerization reaction of (*Z*)-**Stil-NMe₂**, we aimed at demonstrating the occurrence of supramolecular enhancement effects. For this reason, several different experiments were designed in order to elucidate the role played by β -CD in the observed catalytic performance of **AuNP-TF@ β CD3**.

In a first set of experiments, we intended to disable the host-guest interaction between **AuNP-TF@ β CD3** and the substrate molecules, which should minimize supramolecular effects on reactivity. There were basically two ways to do that: (i) the addition of a large excess of a competing guest molecule, or (ii) the addition of excess free β -CD to the reaction medium. In the former case, the new guest introduced would

compete with (*Z*)-**Stil-NMe₂** for interacting with the β -CD hosts at the surface of Au NPs, thus decreasing the number of substrate molecules that may be photoreacted. With this purpose, we added 1-adamantylamine (**Ad-NH₂**) to the photocatalytic medium, since it is able to form highly stable complexes with β -CD ($K_a > 10^3 \text{ M}^{-1}$).³⁵ On the other hand, the addition of excess non-thiolated β -CD would favor the formation of β -CD:(*Z*)-**Stil-NMe₂** inclusion complexes in solution, which were expected to have a similar detrimental effect over the amount of photoreacted substrate. The results obtained in these experiments are shown in Figure 4.19, which were conducted by adding 80 mM of **Ad-NH₂** or 100 mM of β -CD and under the best photocatalytic conditions previously found (45 nM **AuNP-TF@ β CD3**, irradiation at 532 nm and 300 mW for 120 min). In both cases, \sim 3.5-fold lower *Z* \rightarrow *E* conversions were achieved (17 and 16 %, respectively), thus revealing that hindering host-guest association on the surface of the gold nanoparticles significantly decreased the photocatalytic efficiency. Therefore, this clearly supported the occurrence of supramolecular effects on our catalytic system, the main objective of this part of the thesis.

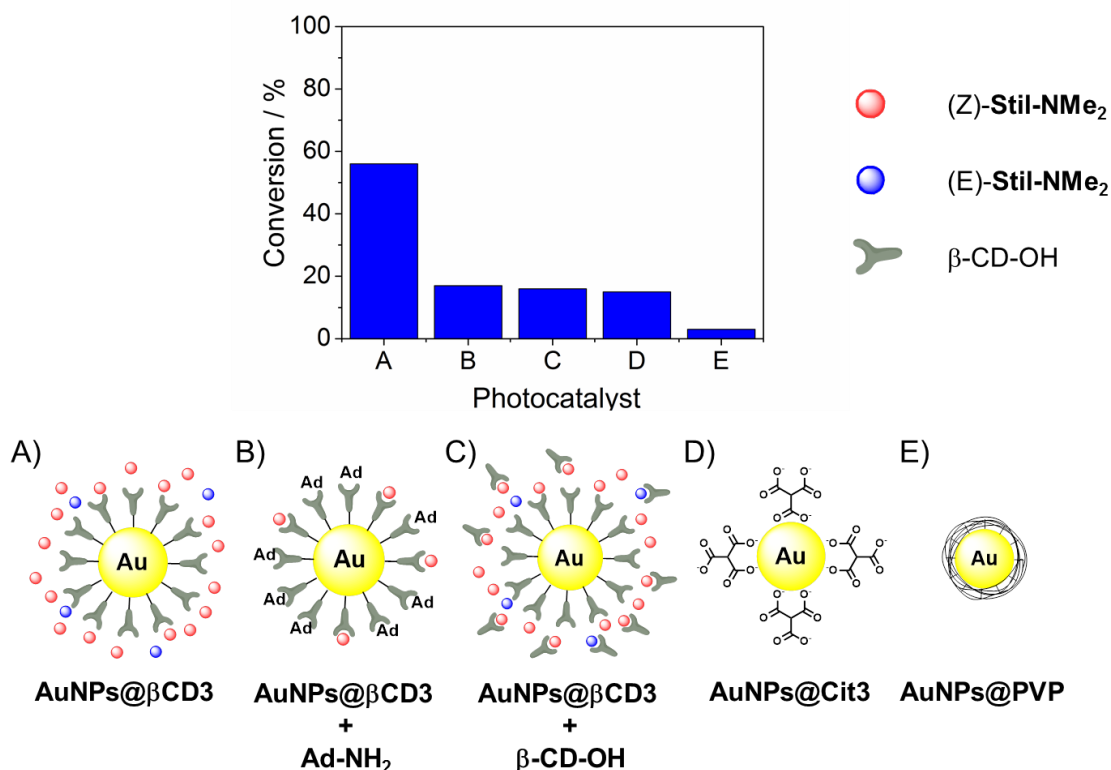


Figure 4.19. Conversion values determined for the photocatalytic *Z* \rightarrow *E* isomerization of (*Z*)-**Stil-NMe₂** under different conditions: (A) in the presence of **AuNP-TF@ β CD3** (56 %) and upon addition of (B) 80 mM **Ad-NH₂** (17 %) and (C) 100 mM β -CD (16 %); in the presence of (D) **AuNP-TF@Cit3** (15 %) and (E) **AuNP-TF@PVP** (3 %). In all the cases, the concentration of

gold nanoparticles was 45 nM and the sample was irradiated with 532 nm-pulsed laser at 300 mW for 120 minutes.

To further corroborate this result, other experiments were conducted using CD-free Au NPs of similar sizes (~15 nm in diameter) that could not supramolecularly interact with (*Z*)-**Stil-NMe₂** or even preclude direct catalyst-substrate contact. This was the case of **AuNP-TF@Cit**, the citrate-stabilized particles used to obtain **AuNP-TF@βCD3** by ligand exchange, and **AuNP-TF@PVP**, which were coated with a ~1.4 nm-thick polyvinylpyrrolidone shell. Low-to-negligible stilbene isomerization was observed in these cases (15 and 3 %, respectively), which further proved enhancement of **AuNP-TF@βCD3** photocatalysis by supramolecular chemistry (Figure 4.19). It must be mentioned that both **AuNP-TF@Cit3** and **AuNP-TF@PVP** fully degraded during the photocatalytic experiment or the subsequent work-up, in contrast to **AuNP-TF@βCD3**. Therefore, this demonstrated the added value of using the heptathiolated ligand **β-CD-(SH)₇** as a photocatalyst stabilizer, which opened the door to catalyst recycling for **AuNP-TF@βCD3** as next discussed.

e) Photocatalyst recycling

As already commented, a further advantage of the use of **AuNP-TF@βCD3** as photocatalyst could be an increased stability owing to the formation of 7 relatively strong Au-S bonds between every host molecule and the surface of the nanoparticle. This should prevent (or slow down) the (photo)chemically-induced loss of stabilizing molecules, therefore preserving the integrity of the capping layer and enlarging the lifetime of the photocatalyst. In view of that, we explored the recycling of **AuNP-TF@βCD3** for the plasmon-based catalysis of (*Z*)-**Stil-NMe₂** isomerization. As shown in Figure 4.20A, **AuNP-TF@βCD3** could be recovered and reused again with no loss in its photocatalytic activity up to three times at the optimal conversion conditions of the model reaction (45 nM **AuNP-TF@βCD3**, irradiation at 532 nm and 300 mW for 120 min).

Despite these promising results, two factors were found to ultimately limit the recyclability of our catalytic system. First, **AuNP-TF@βCD** recovery from the reaction mixture by centrifugation was not fully efficient and a loss of ~66% of the catalyst mass was observed in each step, as demonstrated by the extinction spectra in Figure 4.20B.

For this reason, the conversion yields shown in Figure 4.21A had to be corrected for the amount of catalyst recovered, which allowed demonstrating that the gold nanoparticles retrieved their photocatalytic activity for at least 3 consecutive catalytic cycles.

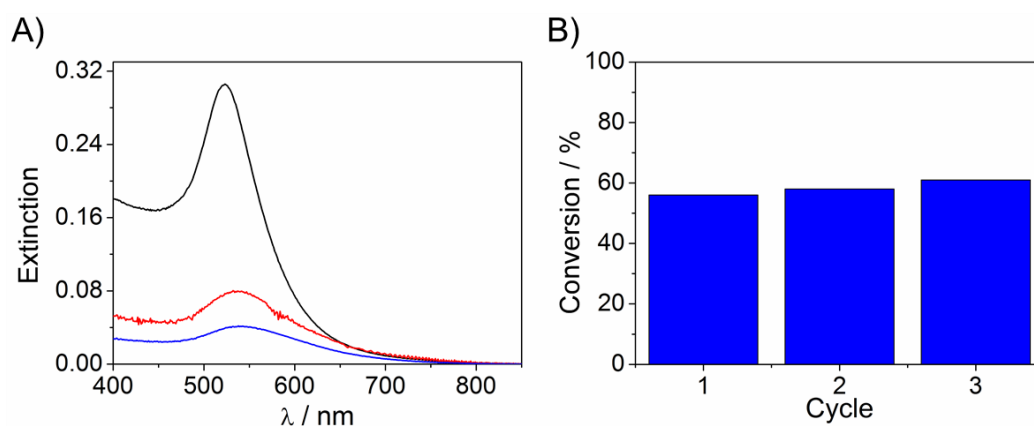


Figure 4.20. Conversion values determined for the photocatalytic $Z \rightarrow E$ isomerization of (*Z*)-**Stil-NMe₂** with **AuNP-TF@ β CD3** for three consecutive catalytic cycles. The initial concentration of gold nanoparticles was 45 nM, and the sample was irradiated with 532 nm-pulsed laser at 300 mW for 120 minutes in all the cases.

In addition, slow photodegradation of **AuNP-TF@ β CD3** into smaller nanostructures (~2-7 nm in size) was also found after prolonged irradiation at 300 mW, as demonstrated by the TEM images in Figure 4.21A-B. Actually, as observed in Figure 4.21C for two independent experiments, a new population of small size nanostructures could clearly be detected in the weight distribution of the Au NPs recovered after one catalytic cycle. Statistical analysis of the two types of nanoparticles found in the TEM images allowed us determining that photodegradation affected between 1-6 % of the initial catalyst mass per each catalytic cycle. Importantly, such process did not take place during the pre-treatment of the nanoparticles at low irradiation power (100 mW, 30 min), but only during the photocatalytic experiments involving higher light intensities and longer illumination times (300 mW, 120 minutes).

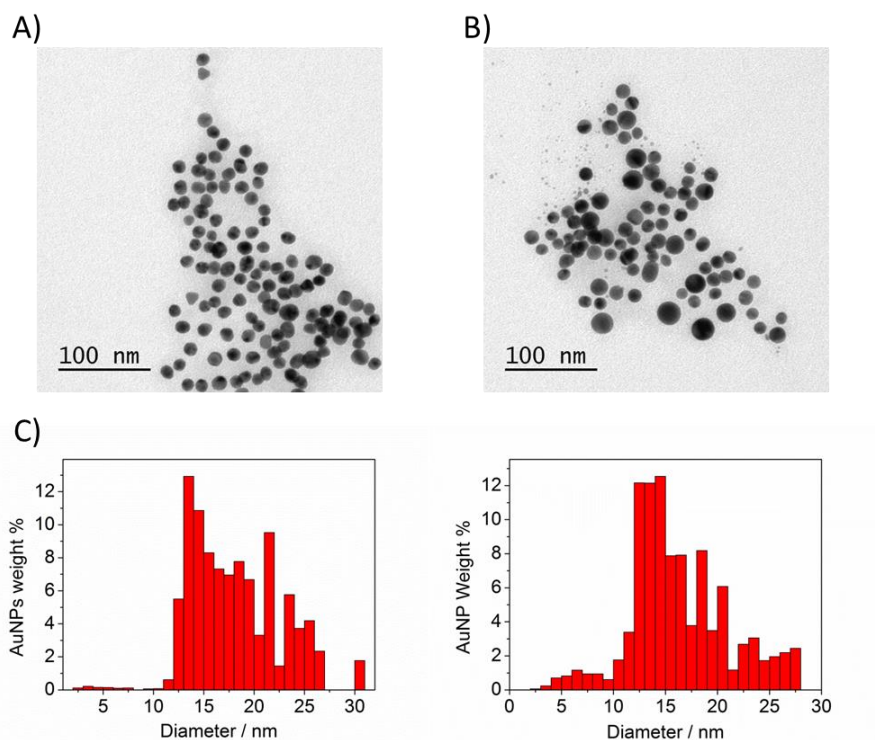


Figure 4.21. A-B) Representative TEM images of A) pre-treated **AuNP-TF@βCD3** (100 mW at 532 nm, 30 min) and B) recovered **AuNP-TF@βCD3** after one photocatalytic experiment (300 mW at 532 nm, 120 minutes). C) Weight distribution of the **AuNP-TF@βCD3** recovered after the first catalytic cycle for two independent assays (300 mW at 532 nm, 2 h).

In order to rule out the possibility that the small Au nanostructures formed by photodegradation were altering the observed conversion values, additional photocatalytic measurements were carried out with ~5 nm-in-diameter Au NPs coated with β -CD-(SH)₇ (**AuNP-K@βCD2**). This NP set was prepared following the direct Kaifer's procedure described in chapter 3 and their photocatalytic efficiencies were assessed independently. To make a proper comparison with the data obtained for **AuNP-TF@βCD3**, two different concentration conditions were taken into account for **AuNP-K@βCD2**: (i) **AuNP-K@βCD2** concentration that matched the extinction value at the irradiation wavelength of the **AuNP-TF@βCD3** suspensions used in the best catalytic experiments (1.94- μ M); (b) **AuNP-K@βCD2** concentration that matched the total catalyst surface area of the **AuNP-TF@βCD3** suspensions used in the best catalytic experiments (420 nM). As can be seen in Table 4.4, at the optimal irradiation conditions established for **AuNP-TF@βCD3**, the use of **AuNP-K@βCD2** led to significantly lower conversion yields (<20 %). These results unambiguously proved that

the $Z \rightarrow E$ isomerization efficiencies determined for **AuNP@ β CD3** arose from the photocatalytic activity of the initial ~15 nm-in-diameter particles prepared.

Table 4.4. $Z \rightarrow E$ isomerization conversions of the control experiments with **AuNP-K@ β CD2**.

Entry	c_{catalyst} / nM	Irradiation power / mW	Irradiation time / min	Yield (%)
1	1940	300	120	18
2	420	300	120	8

f) Photocatalytic isomerization of (Z)-Stil-H and (Z)-Stil-NO₂

To gain deeper insight into the supramolecularly-enhanced activity of **AuNP-TF@ β CD3**, it was decided to expand the photocatalytic studies to stilbenes **Stil-H** and **Stil-NO₂**. With this aim, (Z)-**Stil-H** and (Z)-**Stil-NO₂** were submitted to the best photocatalytic conditions found for (Z)-**Stil-NMe₂**. These compounds showed remarkably lower photocatalytic yields than those previously measured for (Z)-**Stil-NMe₂** (8 and 15 % for (Z)-**Stil-H** and (Z)-**Stil-NO₂**, respectively). However, as can be seen in Figure 4.22, they were ca. 2.5-fold larger than those registered when using **AuNP-TF@Cit3** as a catalyst under the same conditions (3 and 6 % for (Z)-**Stil-H** and (Z)-**Stil-NO₂**, respectively).

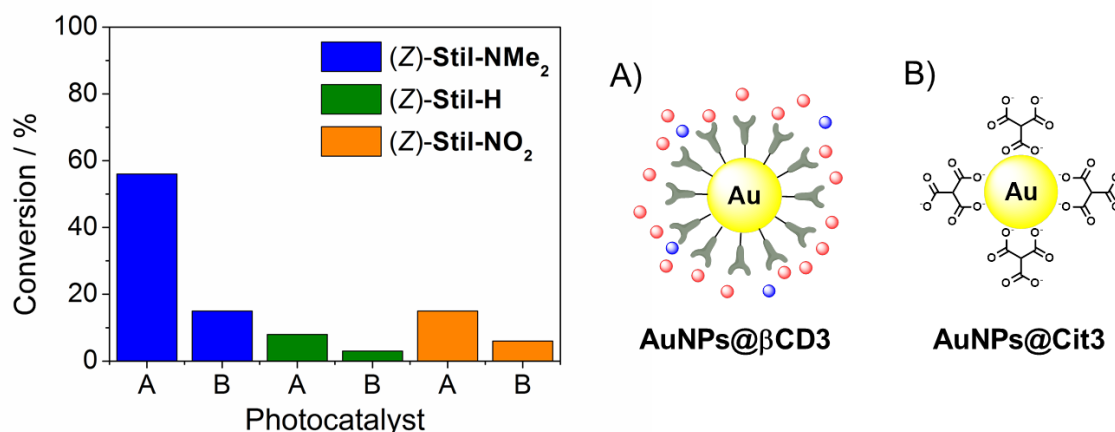
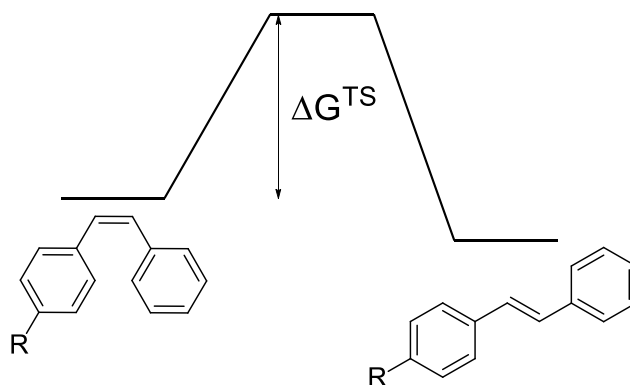


Figure 4.22. Conversion values determined for the photocatalytic $Z \rightarrow E$ isomerization of (Z)-**Stil-H** and (Z)-**Stil-NO₂** in the presence of **AuNP-TF@ β CD3** (8 % for (Z)-**Stil-H** and 15 % for (Z)-**Stil-NO₂**) or **AuNP-T@Cit3** (3 % for (Z)-**Stil-H** and 6 % for (Z)-**Stil-NO₂**) at the best photocatalytic conditions encountered for (Z)-**Stil-NMe₂** (45 nM concentration of nanoparticles, laser pulsed irradiation at 532 nm and 300 mW for 120 min).

These results suggested the existence of supramolecular effects on the photocatalytic isomerization of (*Z*)-**Stil-H** and (*Z*)-**Stil-NO₂** despite their lower association constants with β -CD compared with that of (*Z*)-**Stil-NMe₂** (see Table 4.1 above). This was ascribed to the similar amounts of reactive CD-stilbene complexes which were expected to be formed in all the cases regardless of the distinct K_a values (~ 0.1 % in the steady state at our conditions). Actually, the dramatic changes in photocatalytic activity observed for the stilbene derivatives under study cannot be explained on the sole basis of their different supramolecular association constants, since clearly larger photocatalytic efficiencies were also found for (*Z*)-**Stil-NMe₂** with **AuNP-TF@Cit3**. Therefore, a crucial role should also be played by the intrinsic capacity of Au NPs to photoinduce the isomerization of electronically-different stilbenes, which must be ultimately related with the underlying catalytic mechanism.

4.2.6. Photocatalytic mechanism of (*Z*)-stilbenes isomerization with Au NPs

Once proven the supramolecularly-enhanced photocatalytic activity of **AuNP-TF@ β CD3** for the isomerization reaction of different (*Z*)-stilbenes, we turned our attention to the study of the reaction mechanism for the catalytic process. On the one hand, plasmon-based photocatalysis of stilbene isomerization could be attributed to a photothermal mechanism, where the heat released after Au NP excitation could allow the *Z* \rightarrow *E* isomerization barrier in the electronic ground state to be overcome (Scheme 4.5). From an experimental point of view, this was explored by bulk heating the (*Z*)-stilbenes of choice in the dark at different conditions, the results of which have already been discussed (see Table 4.3 above). Briefly, in the absence of Au NPs, thermal *Z* \rightarrow *E* conversion was only observed for (*Z*)-**Stil-NMe₂**, a behavior that qualitatively resembled our photocatalytic results. Nevertheless, it must not be overlooked that the kinetics determined for the thermal isomerization of (*Z*)-**Stil-NMe₂** did not correspond to that of a simple unimolecular reaction, but to a more complex mechanism (see Figure 4.15 above), which hampered assigning plasmon-based stilbene *Z* \rightarrow *E* conversion to pure photothermal effects.



Scheme 4.5. Pure thermal mechanism of the $Z \rightarrow E$ isomerization of stilbenes.

To better assess on the photothermal effects on **AuNP-TF@ β CD3** photocatalysis, computational calculations were performed by Dr. Francesca Peccati from Prof. Mariona Sodupe's group in the Department of Chemistry of UAB. In particular, previously calibrated broken symmetry density functional theory calculations were carried out to compute the energy barrier for the thermal $Z \rightarrow E$ isomerization (ΔG^{TS}) of **Stil-NMe₂**, **Stil-H** and **Stil-NO₂**, among other parameters. Interestingly, large and very similar barriers were obtained for the three compounds, which were higher than 160 kJ mol^{-1} in all the cases (Table 4.5). As such, no significant differences in $Z \rightarrow E$ conversion should be expected for these compounds if **AuNP-TF@ β CD3** photocatalytic effect was purely photothermal, which was in striking contrast with our experimental data. Therefore, the occurrence of this mechanism was ruled out.

Table 4.5. Relative stabilities of isomers Z and E (ΔG_{Z-E} , in kJ mol^{-1}), $Z \rightarrow E$ isomerization energy barriers (ΔG^{TS} , in kJ mol^{-1}) and ionization energies (**IE**, in eV) for the neutral and radical cation forms of (Z)-**Stil-NMe₂**, (Z)-**Stil-H** and (Z)-**Stil-NO₂**.^{a)}

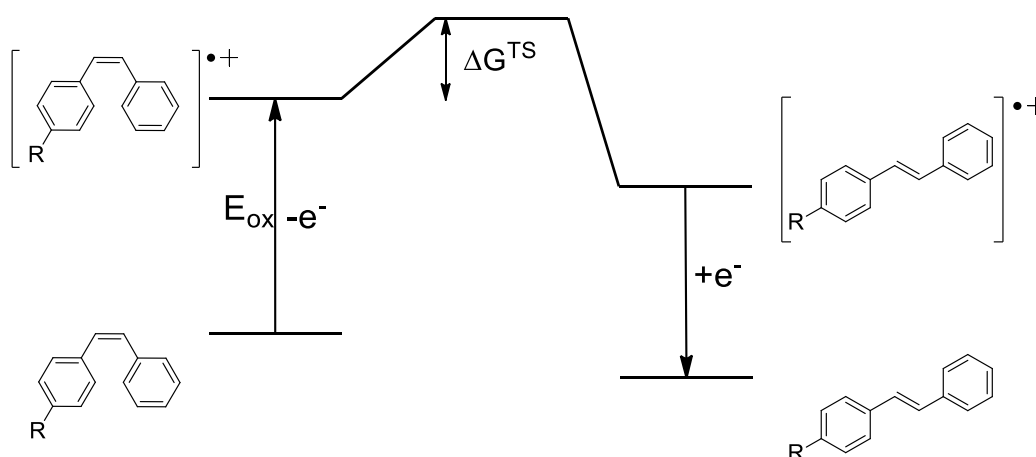
Reactant	ΔG_{Z-E}	ΔG^{TS}	IE	Reactant	ΔG_{Z-E}	ΔG^{TS}
Stil-NMe₂	19.7	162.9	6.5	Stil-NMe₂^{•+}	31.3	77.2
Stil-H	19.6	165.2	7.5	Stil-H^{•+}	33.5	96.9
Stil-NO₂	20.6	161.4	8.0	Stil-NO₂^{•+}	30.9	83.8

^{a)} Computed at the MPWB1K/6-311+G(2d,p) level of theory.

An alternative photocatalytic mechanism would be near-field enhancement of the two-photon (2P) isomerization of (Z)-stilbenes with visible light, as reported for azobenzenes.^{36a} However, this hypothesis was dismissed on the basis of two different

factors. On the one hand, it must be taken into account that (*E*)-stilbenes are known to present larger 2P absorption cross-sections than their *Z* isomers, which makes $E \rightarrow Z$ isomerization the most favored nonlinear optical process under irradiation at 532 nm.^{36b} On the other hand, no $E \rightarrow Z$ conversion was observed for (*E*)-**Stil-NMe₂** when subjected to the best photocatalytic conditions found for (*Z*)-**Stil-NMe₂**, as already discussed. For these reasons, it was concluded that the **AuNP-TF@βCD3**-induced $Z \rightarrow E$ stilbene conversion could not be ascribed to near-field enhancement of 2P isomerization.

Finally, we explored a third type of mechanism for **AuNP-TF@βCD3** photocatalysis, which involves hot charge carrier injection from the particles followed by isomerization of the resulting stilbene ion, as can be seen in Scheme 4.6.



Scheme 4.6. Proposed isomerization mechanism of stilbenes based on hot charge injection.

In particular, our attention focused on analyzing the effect of hole injection from **AuNP-TF@βCD3** to the substrate, since the largest yields were measured for electron-rich (*Z*)-**Stil-NMe₂** (i.e. the stilbene derivative of choice that was *a priori* more prone to undergo oxidation). Two main parameters were evaluated to assess the viability of this mechanism. First, the oxidation tendency of **Stil-NMe₂**, **Stil-H** and **Stil-NO₂** was characterized, for which we determined: (i) their electrochemical potentials by cyclic voltammetry (Table 4.6 and Figure 4.23), a study developed in collaboration with Dr. Gonzalo Guirado from our own research group; and (ii) their ionization potentials computationally, which were already shown in Table 4.5 above. As expected, our results demonstrated that (*Z*)-**Stil-NMe₂** shows the lowest oxidation (E_{ox}) and ionization potentials and, therefore, it must have the higher tendency to capture holes from Au NPs. In a second step, the energy barrier for the thermal $Z \rightarrow E$ isomerization of **Stil-**

$\text{NMe}_2^{\bullet+}$, $\text{Stil-H}^{\bullet+}$ and $\text{Stil-NO}_2^{\bullet+}$ were estimated theoretically in order to assess the capacity of these species to react once oxidized (see Table 4.5 above and Figure 4.23). Clearly, isomerization energy barriers for the cationic species were found to be significantly smaller ($\sim 50\%$) than those of the corresponding neutral species and, indeed, the lowest value was computed for (*Z*)- $\text{Stil-NMe}_2^{\bullet+}$, the more reactive stilbene derivative in our experiments. In addition, it must be noted that such barriers are on the upper limit of available thermal energy at room temperature ($\sim 80 \text{ kJ mol}^{-1}$), which should make the isomerization of (*Z*)- $\text{Stil-NMe}_2^{\bullet+}$, (*Z*)- $\text{Stil-H}^{\bullet+}$ and (*Z*)- $\text{Stil-NO}_2^{\bullet+}$ feasible at 298 K and, even better, upon photothermal heating.

Table 4.6. Redox potentials determined for stilbene derivatives Stil-NMe_2 , Stil-H and Stil-NO_2 .

Compound	E_{red} vs SCE (V)	E_{ox} vs SCE (V)
(<i>Z</i>)- Stil-NMe_2	-2.47 ^{a)}	0.58 ^{a)}
(<i>Z</i>)- Stil-H	-2.31 ^{a)}	1.59 ^{b)}
(<i>Z</i>)- Stil-NO_2	-1.11 ^{a)}	1.74 ^{b)}
(<i>E</i>)- Stil-NMe_2	-2.42 ^{a)}	0.51 ^{a)}
(<i>E</i>)- Stil-H	-2.28 ^{a)}	1.49 ^{b)}
(<i>E</i>)- Stil-NO_2	-1.08 ^{a)}	1.72 ^{b)}

^{a)} Reversible wave. E^0 is given. ^{b)} Irreversible wave. Anodic or cathodic peak potentials are given.

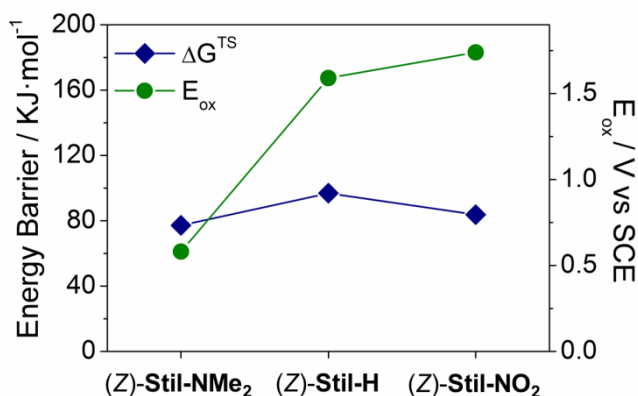


Figure 4.23. Theoretical isomerization energy barriers computed for the radical cation forms (ΔG^{TS}) of (*Z*)- Stil-NMe_2 , (*Z*)- Stil-H and (*Z*)- Stil-NO_2 , and experimental oxidation potentials (E_{ox}) of these compounds.

Based on these evidences, a tentative mechanism was proposed for the large photocatalytic $Z \rightarrow E$ conversion of **Stil-NMe₂** (Figure 4.24), which consists in: (i) host-guest complex formation onto **AuNP-TF@ β CD3**, (ii) light-induced hole transfer to the nearby stilbene molecule, the isomerization of which is probably accelerated by the concomitant photothermal effect caused, and (iii) subsequent reduction of (*E*)-**Stil-NMe₂^{•+}** to render the final neutral product of the reaction, which must take place at the nanoparticle surface (or by interaction with a free (*Z*)-**Stil-NMe₂** molecule, although this is a more unlikely process due to the lower oxidation potential of (*E*)-**Stil-NMe₂**).

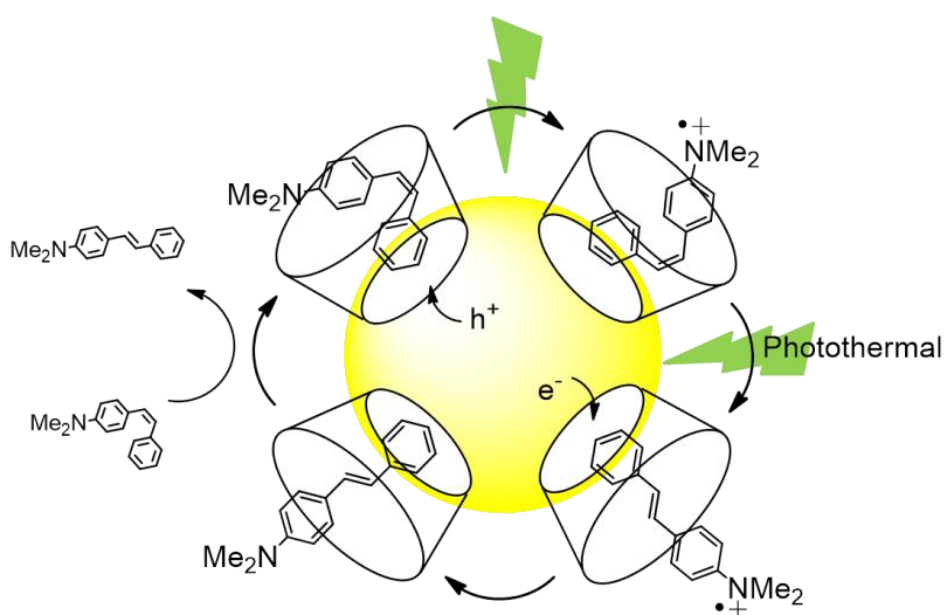


Figure 4.24. Mechanism proposed for the photocatalytic isomerization of (*Z*)-**Stil-NMe₂** on **AuNP-TF@ β CD**.

To corroborate the mechanism proposed, additional experiments were performed with another electron-rich stilbene derivative capable to display similar reactivity to (*Z*)-**Stil-NMe₂**. For this purpose, commercially available (*Z*)-4-hydroxystilbene ((*Z*)-**Stil-OH**), which showed relatively low oxidation and ionization potentials, high thermal isomerization barrier and large capacity to supramolecularly interact with β -CD (Table 4.7). Large photocatalytic $Z \rightarrow E$ conversion with **AuNP-TF@ β CD3** was also measured for **Stil-OH** (88 %), thus supporting the reaction scheme devised for electron-rich stilbenes in Figure 4.24. Actually, non-negligible (*Z*)-**Stil-OH** isomerization was observed by effect of **AuNP@ β CD3** even in the dark (17 %), which hinted for a stronger catalyst-substrate interaction in this case that might explain the larger photocatalytic efficiency observed with respect to (*Z*)-**Stil-NMe₂**.

Table 4.7. Association constants with β -CD (K_a in M^{-1}) and oxidation potential (E_{ox} vs SCE, in V) of (*E*)-**Stil-OH** and (*Z*)-**Stil-OH**. Ionization energies (IE, in eV), $Z \rightarrow E$ isomerization energy barriers (ΔG^{TS} , in $kJ\ mol^{-1}$) for the neutral (n) and radical cation (rc) forms of (*Z*)-**Stil-OH**.

Compound	K_a / M^{-1}	E_{ox} vs SCE	IE	ΔG^{TS}_n	ΔG^{TS}_{rc}
(<i>E</i>)- Stil-OH	1056 ± 163^a	1.10^b	-	-	-
(<i>Z</i>)- Stil-OH	724 ± 223^a	1.13^b	7.1	164.1^c	83.8^c

^a Determined in water:acetonitrile 94:6. ^b Irreversible wave. ^c Computed at the MPWB1K/6-311+G(2d,p) level of theory.

According to the photocatalytic mechanism proposed in this section, the significantly lower $Z \rightarrow E$ conversions achieved for (*Z*)-**Stil-H** and (*Z*)-**Stil-NO₂** with **AuNP-TF@ β CD3** could be rationalized on the basis of their larger oxidation potentials and, therefore, their lower capacity to suffer hole injection from gold nanoparticles. However, Au NPs are also known to photocatalyze reduction reactions via electron injection.^{9,10} In view of this, an alternative photocatalytic pathway for the isomerization of electron-poor (*Z*)-stilbenes such as (*Z*)-**Stil-NO₂** could be devised in analogy to the mechanism shown in Figure 4.24, which would evolve through electron injection from Au NPs to the molecular substrate followed by isomerization of the resulting radical anion. Although we did not explore this mechanism in detail in this work due to the low conversions obtained for (*Z*)-**Stil-NO₂**, it might explain why slightly larger photocatalytic efficiencies were measured for this compound with respect to (*Z*)-**Stil-H** despite presenting lower association constants with β -CD.

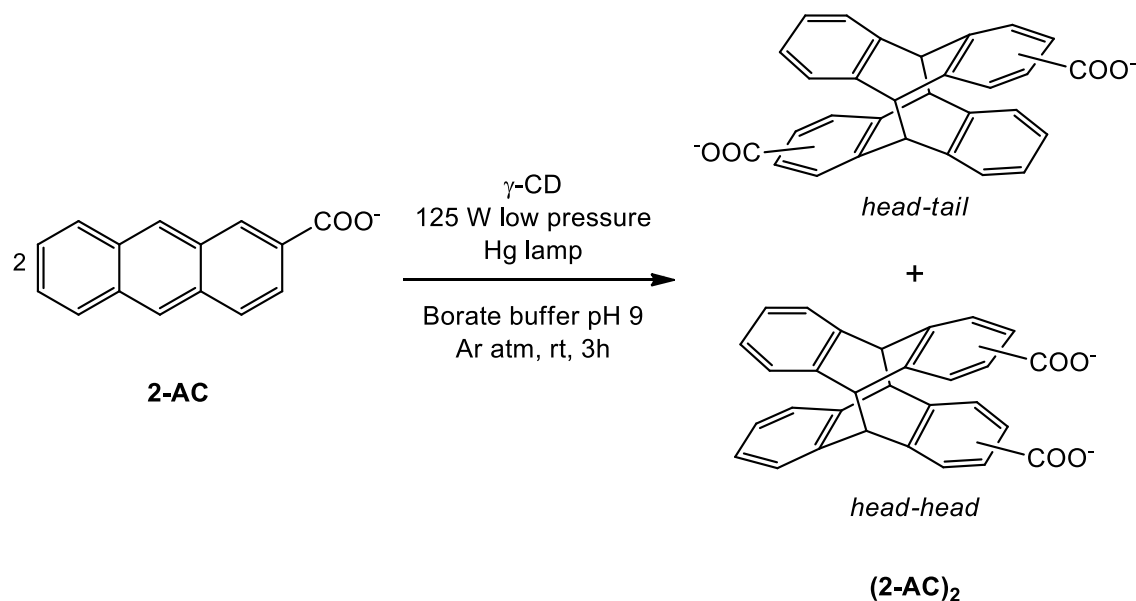
In summary, a new strategy for plasmon-based catalysis has been introduced that relies on the functionalization of noble metal nanoparticles with supramolecular hosts. Although similar approaches have already been used to design drug delivery systems, catalysts for thermal aqueous biphasic reactions and separation agents,³⁷ the results described in this chapter prove for the first time that it enhances the photocatalytic activity of Au NPs by (a) promoting approximation to the catalyst, (b) ensuring reactant and product renewal, and (c) rising catalyst stability.

4.3. PHOTOCATALYSIS OF BIMOLECULAR REACTIONS

Once demonstrated that our supramolecular approach for enhancing Au NP photocatalysis worked for unimolecular reactions, it was decided to expand the scope of this strategy to more complicated processes. In particular, the substitution of β -CD by γ -CD, the largest member of the CD family, opened up the possibility to undertake photocatalytic studies of bimolecular reactions, since the bigger cavity of this supramolecular host allows the formation of host:guest complexes with 1:2 stoichiometry. There are indeed several examples in the literature describing such complexes between γ -CD and different organic molecules, such as stilbenes,³⁸ anthracenes,³⁹ etc. In some of them, γ -CD is used as a molecular template to induce bimolecular photochemical processes owing to its supramolecular host-guest behavior and, therefore, its capacity to bring two molecular guests into close proximity when they are encapsulated into its hydrophobic cavity. This is the case of 2-anthracenecarboxylate (**2-AC**) photodimerization under UV irradiation in the presence of γ -CD. In this reaction the use of γ -CD (and γ -CD derivatives) not only favors photoreactivity, but it was also demonstrated that it causes a preferential orientation of the substrate molecules allowing the photochemical reaction to take place regio- and enantioselectively.^{40,41} Therefore, reproduction of this reaction under Au NP photocatalysis to test the viability of the supramolecular approach developed in this work was found an interesting challenge, especially since the dimerization of electron-poor anthracenes has also been reported to occur electrochemically upon reduction.⁴² As a consequence, plasmon-induced photocatalysis of this process by hot electron injection from Au NPs might well be conceivable. In view of this, γ -CD-functionalized Au NPs were prepared and their capacity to promote the [4+4] photocycloaddition of **2-AC** upon plasmon excitation at 532 nm was investigated.

4.3.1. Photoinduced [4+4] cycloaddition of 2-anthracenecarboxylate

Prior to photocatalytic experiments, the γ -CD-enhanced photodimerization of **2-AC** under direct UV excitation was first attempted as a reference following the procedure described by Inoue *et al*⁴³ (Scheme 4.7). In this procedure the reaction is carried out in the presence of an excess of γ -CD and in an aqueous borate buffer (pH 9) to increase the solubility of **2-AC**, while irradiation is performed at 254 nm using a low pressure Hg 125 W lamp and a quartz reactor. To minimize photodegradation, inert atmosphere is typically used.

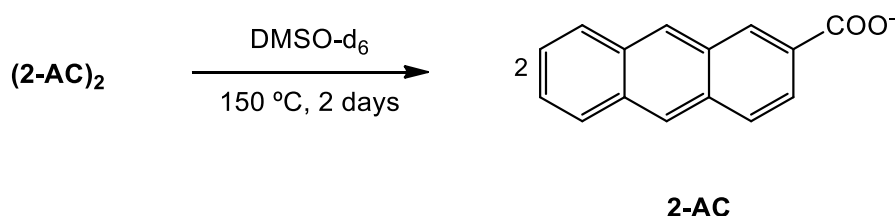


Scheme 4.7. Photoinduced dimerization of 2-AC in the presence of γ -CD.

According to Woodward-Hoffman rules, [4+4] cycloadditions are thermally forbidden and must follow a photochemical mechanism.⁴⁴ In the case of anthracene dimerization, it proceeds via photoexcitation of one **2-AC** molecule followed by formation of an excimer complex by π - π interaction with another **2-AC** molecule in the ground state, which should finally relax via cycloaddition reaction.⁴⁴ Since excimer formation must take place during the short lifetime of the excited state of **2-AC**, this process and, therefore, the overall photochemical reaction is highly favored by the presence of γ -CD, since the formation of the corresponding 1:2 host-guest complex allows the reactant molecules to be close to each other for longer times.

The photodimer product obtained for **2-AC** in this way (**(2-AC)₂**) is a mixture of 4 different regio- and stereoisomers, two *head-head* and two *head-tail* isomers, according to the different orientation of the carboxylic groups of the two tethered anthracene moieties. Although the mixture obtained in our case with 38 % yield was not resolved, it is reported that at the conditions employed the resulting is composed of around 90 % of *head-tail* isomers and 10 % of *head-head* isomers.⁴³ This regioisomer ratio is attributed to the preferred orientation of **2-AC** molecules inside the CD cavity, which minimizes electrostatic repulsion between carboxylate groups and, as such, favors *head-tail* isomers. In what regards to the elucidation of the stereoisomer mixture for each of two types of regioisomers of the photodimerization reaction, it requires further HPLC characterization and was beyond the scope of our work.

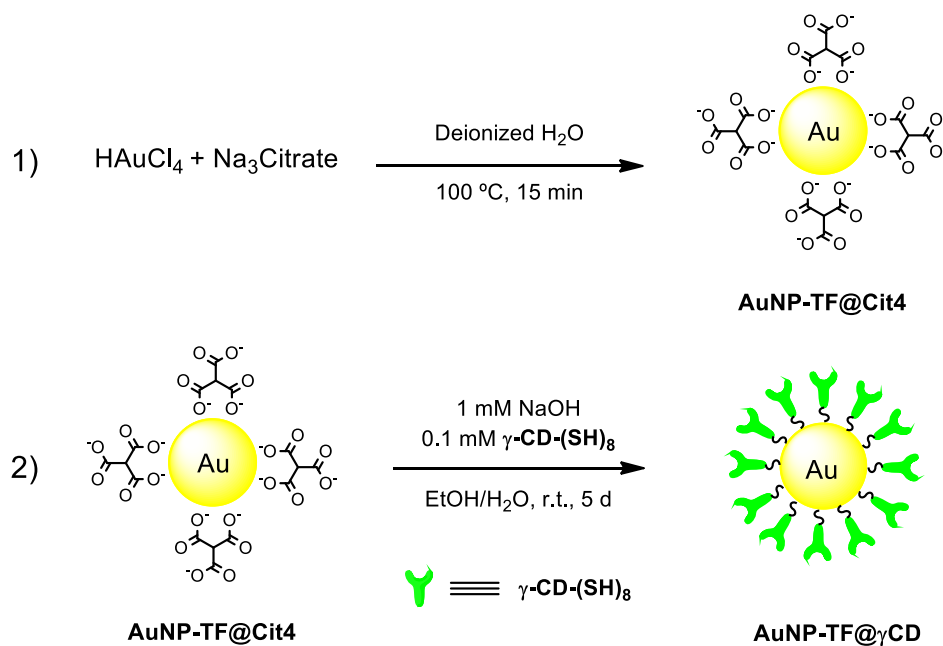
Once **(2-AC)₂** was prepared, some additional experiments were carried out with this mixture of **2-AC** photodimers. As already commented, Au NPs exhibit a strong photothermal effect upon plasmon excitation. For this reason, the thermal stability of **(2-AC)₂** was investigated to evaluate the possibility of photothermal retrocycloaddition that could occur after dimer formation under Au NP photocatalysis. As shown in Scheme 4.8, thermal assays consisted in heating the photodimer mixture at 150 °C during 2 days while it was monitored by ¹H NMR spectroscopy. After 24 h, a 11 % of **(2-AC)₂** had been already converted back to anthracene monomers and this value raised up to 25 % after 48 h. Therefore, this evidenced that retrocycloaddition of **(2-AC)₂** occurs at high temperatures, and although it takes place at rather slow rates, it might interfere with our photocatalytic experiments.



Scheme 4.8. Thermal retrocycloaddition of **2-AC** photodimers.

4.3.2. Preparation of gold nanoparticles functionalized with γ -cyclodextrin

In order to assay the photocatalytic [4+4] cycloaddition of **2-AC**, Au NPs functionalized with thiolated γ -CD derivative **γ -CD-(SH)₈** described in chapter 3 had to be prepared. Prompted by the good results obtained with **AuNP-TF@ β CD3** in terms of photocatalytic efficiency and photostability, analogous γ -CD-coated Au NPs were synthesized (**AuNP-TF@ γ CD**). Namely, they were prepared of ~15 nm in diameter and they were obtained in two steps via Turkevich-Frens synthesis of citrate-stabilized gold nanoparticles (**AuNP-TF@Cit4**) and subsequent ligand exchange, as illustrated in Scheme 4.9.



Scheme 4.9. Two-step procedure for the preparation of **AuNP@ γ CD**.

As already described for **AuNP-TF@ β CD3**, **AuNP-TF@ γ CD** showed significant aggregation after preparation and purification, which could be reverted back by pulsed laser illumination at 532 nm and relatively low powers. After this treatment, **AuNP-TF@ γ CD** displayed a rather narrow extinction spectrum located at $\lambda_{\text{LSPR}} = 530$ nm, which however presented a non-negligible red-shift with respect to parent **AuNP-TF@Cit** (Figure 4.25A). In addition, **AuNP-TF@ γ CD** preserved their size and shape after ligand exchange and had an average diameter of 17 ± 4 nm, as evidenced by TEM analysis (Figure 4.25B).

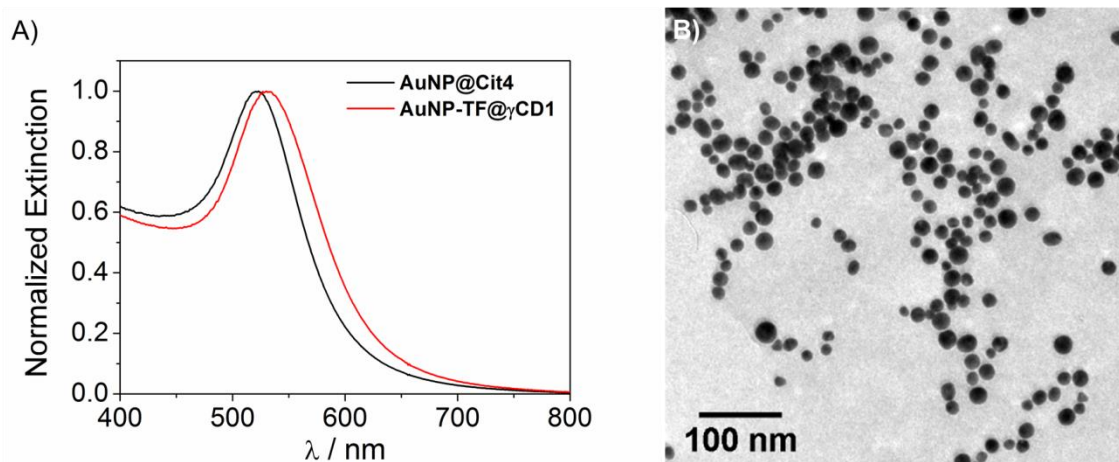
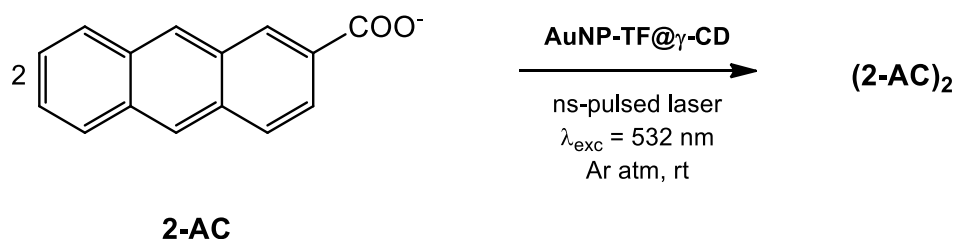


Figure 4.25. A) UV-Vis extinction spectra in water of **AuNP-TF@Cit4** ($\lambda_{\text{LSPR}} = 523$ nm) and **AuNP-TF@ γ CD** ($\lambda_{\text{max}} = 530$ nm). B) TEM image of **AuNP-TF@ γ CD**.

4.3.2. Photocatalytic dimerization of 2-antracencarboxylate with gold nanoparticles

After preparation and characterization of **AuNP-TF@ γ CD**, the photocatalytic [4+4] cycloaddition of **2-AC** under plasmon excitation of gold nanoparticles was attempted. Analogous conditions to those used for the photocatalysis of stilbene isomerization with **AuNP-TF@ β CD3** were applied, which consisted in irradiation at room temperature and under inert atmosphere with a ns-pulse laser at 532 nm (Scheme 4.10). In what regards to the medium used, two different conditions were considered: (i) 94:6 water:DMSO mixtures, and (ii) 94:6 aqueous borate buffer (pH 9):DMSO. The latter was preferred to ensure deprotonation of the starting 2-antracencarboxylic substrate and, therefore, maximum concentration of **2-AC** in solution. Unfortunately, **AuNP-TF@ γ CD** were found not to be fully stable in this medium and they were observed to aggregate in time. For this reason, the photocatalytic experiments in aqueous borate buffer could not be extended for more than 120 minutes.



Scheme 4.10. [4+4] cycloaddition of **2-AC** under plasmon excitation of **AuNP-TF@ γ CD**.

Once conducted the photocatalytic experiments, the resulting samples were treated with acid and centrifuged to separate the photocatalyst from the mixture of **(2-AC)₂** products and non-reacted **2-AC**, which was analyzed by ¹H NMR spectroscopy. Table 4.8 summarizes the results obtained in this way for the most important experiments carried out. As can be observed, formation of **(2-AC)₂** was observed in none of them (and in none of other assays performed). It must be taken into account that for the experiments shown in Table 4.8, we used: (i) the maximum dispersable amount of **AuNP-TF@ γ CD**, which was found to be around 30 nM; (ii) the maximum irradiation power at which **AuNP-TF@ γ CD** was observed to be stable for relatively long times (300 mW).; (iii) the maximum irradiation time for which **AuNP-TF@ γ CD** showed

stability in aqueous borate buffer (2 h). In view of all, stronger photocatalytic conditions could not be applied to enhance conversion.

Table 4.8. Summary of the reaction conditions assayed in the photocatalytic studies.

Experiment	[AuNP-TF@ γ CD1] / nm	[2-AC] / mM	Irr power / mW	Irr time / h	[Borate buffer] / mM	Conversion / %
1	30	10	300	2	-	0
2	30	10	300	2	50	0
3	30	10	300	4	-	0

Two main factors may account for the observed results on the photocatalytic **2-AC** dimerization with **AuNP-TF@ γ CD**. On the one hand the injection of hot electrons from Au NPs to **2-AC** may not be efficient at all, accounting for their respective redox potentials. This could be investigated by varying the photocatalyst in order to improve its reducing capacity or simply implementing the use of more electron-poor anthracene substrates which would have more tendency to be reduced. On the other hand the solubility problems encountered when trying to raise the catalyst concentration, ultimately limited the amount of CD molecules in the photocatalytic experiments. Taking in to account that γ -CD concentration was ca. 16 μ M (~310 γ -CD molecules/NP), and the expected K_a value for the 1:2 complex between γ -CD and **2-AC** at 25 °C,⁴³ the amount of γ -CD molecules in the form of supramolecular host-guest complexes with 2-AC are around 0.001 % at our photocatalytic conditions. This handicap and the low probability of the reaction to occur may have limited the amount of photoreactive species in solution making imperceptible the eventual formation of photodimers.

4.4. SUMMARY AND CONCLUSIONS

In this chapter, a new supramolecular approach for the enhancement of Au NP photocatalysis based on CD-functionalized Au NPs is described. With the methodology described in chapter 3, functionalized Au NPs with different CD derivatives have been prepared, with which we tested the viability of the proposed supramolecular approach towards selected benchmark reactions:

- a) Our study on stilbene isomerization demonstrated that supramolecular host-guest interactions can be used to enhance Au NP photocatalysis. **AuNP-TF@ β CD** showed increased photocatalytic activity towards the isomerization of stilbenes with respect to non-functionalized Au NPs **AuNP-TF@Cit**. Such increase was higher in the case of electron-rich stilbenes (**Z**)-**Stil-NMe₂** and (**Z**)-**Stil-OH**.
- b) The observed increase in catalytic activity came from the host-guest interactions established between β -CD at the surface of the NP and reactant molecules. In addition, the multiple Au-S bond attachment of the CD derivative to the NP surface allowed for catalyst recycling while preserving the photocatalytic performance of **AuNP-TF@ β CD**.
- c) The study of the reaction mechanism, suggested that the photocatalytic activity observed for **AuNP-TF@ β CD** came from a combination of hole (or electron) injection from the Au NP to the stilbene substrate, followed by thermal isomerization of the corresponding radical cation (or anion) and subsequent back reduction (or oxidation) to the neutral form of the molecule.
- d) The exploration of more complex processes to expand the scope of the supramolecular approach described in this chapter, like the cycloaddition of **2-AC** mediated by **AuNP-TF@ γ CD**, gave any good result since no product formation could be detected from our experiments.

4.5. BIBLIOGRAPHY

- [1] Love, J. C.; Estroff, L. A.; Kriebel, J. K.; Nuzzo, R. G.; Whitesides, G. M. *Chem. Rev.* **2005**, 105, 1103.
- [2] Sepúlveda, B.; Angelomé, P. C.; Lechuga, L. M.; Liz-Marzán, L. M. *Nano Today* **2009**, 4, 244.
- [3] Saha, K.; Agasti, S. S.; Kim, C.; Li, X.; Rotello, V. M. *Chem. Rev.* **2012**, 112, 2739.
- [4] Yang, Y.; Feng, S.; Li, M. Wu, Z.; Fang, X.; Wang, F.; Geng, D.; Yang, T.; L, X.; Sun, B.; Gao, X. *ACS Appl. Mater. Interfaces* **2015**, 7, 24430.
- [5] Zhou, X.; Liu, G.; Yu, J.; Fan, W. *J. Mater. Chem.* **2012**, 22, 21337.
- [6] Wang, C.; Astruc, D. *Chem. Soc. Rev.* **2014**, 7188.
- [7] Baffou, G.; Quidant, R. *Chem. Soc. Rev.* **2014**, 43, 3898.
- [8] Linic, S.; Aslam, U.; Boerigter, C.; Morabito, M. *Nat. Mater.* **2015**, 14, 567.
- [9] Zhu, H.; Ke, X.; Yang, X.; Sarina, S.; Liu, H. *Angew. Chem. Int. Ed.* **2010**, 49, 9657.
- [10] Bueno-Alejo, J. C.; Fasciani, C.; Grenier, M.; Netto-Ferreira, J. C., Scaiano, J. C. *Catal. Sci. Technology* **2011**, 1, 1506.
- [11] Chen, X.; Zhu, H.-Y.; Zhao, J.-C.; Zheng, Z.-F.; Gao, X.-P. *Angew. Chem. Int. Ed.* **2008**, 47, 5353.
- [12] Xiao, Q.; Liu, Z.; Bo, A.; Zavahir, S.; Sarina, S.; Bottle, S.; Riches, J. D.; Zhu, H. *J. Am. Chem. Soc.* **2015**, 137, 1956.
- [13] Bakhtiary, A. B. S.; Hsiao, D.; Jin, G, Gates, B. D.; Branda, N. R. *Angew. Chem. Int. Ed.* **2009**, 48, 4166.
- [14] Mukherjee, S.; Zhou, L.; Goodman, A. M.; Large, N.; Ayala-Orozco, C.; Zhang, Y.; Nordlander, P.; Halas, N. J. *J. Am. Chem. Soc.* **2014**, 136, 64.
- [15] Wang, F.; Li, C.; Chen, H.; Jang, R.; Sun, L.-D.; Li, Q.; Yu, J. C.; Yan, C. H. *J. Am. Chem. Soc.* **2013**, 135, 5588.
- [16] Pineda, A.; Gómez, L.; Balu, A. M.; Sebastián, V.; Ojeda, M., Romero, A.-A.; Santamaría, J.; Luque, R. *Green Chem.* **2013**, 15, 2043.
- [17] Fasciani, C.; Bueno-Alejo, J. C.; Grenier, M.; Netto-Ferreira, J. C.; Scaiano, J. C. *Org. Lett.* **2011**, 13, 204.
- [18] Ueno, K.; Juodkacis, S.; Shibuya, T.; Yokota, Y.; Mizeikis, V.; Sasaki, K.; Misawa, H. *J. Am. Chem. Soc.* **2008**, 130, 6928.
- [19] Hallet-Tapley, G. L.; Silvero, M. J.; González-Béjar, M.; Grenier, M.; Netto-Ferreira, J. C.; Scaiano, J. C. *J. Phys Chem C* **2011**, 115, 10784.
- [20] Zeng, Z.; Tachikawa, T.; Majima, T. *J. Am. Chem. Soc.* **2014**, 136, 6870.
- [21] Scaiano, J. C.; Netto-Ferreira, J. C.; Alarcon, E.; Billone, P.; Bueno-Alejo, C. J.; Crites, C.-O. L.; Decan, M.; Fasciani, C.; González-Béjar, M.; Hallet-Tapley, G.;

- Grenier, M.; McGilvray, K. L.; Pacioni, N. L.; Pardoe, A.; René-Boisneuf, L.; Schwartz-Narbone, R.; Silvero, M. J.; Stampelcoskie, K. G.; Wee, T.-L. *Pure Appl. Chem.* **2011**, 83, 913.
- [22] Dsouza, R. N.; Pischel, U.; Nau, W. M. *Chem. Rev.* **2011**, 111, 2941.
- [23] Waldeck, D. H. *Chem. Rev.* **1991**, 91, 415.
- [24] Herrmann, W.; Wehrle, S.; Wenz, G. *Chem. Commun.* **1997**, XX, 1709.
- [25] (a) Kistiakowsky, G.; Smith, W. R. *J. Am. Chem. Soc.* **1934**, 56, 638.
(b) Saltiel, J.; Ganapathy, S.; Werking, C. *J. Phys. Chem.*, **1987**, 91, 2755.
- [26] (a) Ward, T. A.; Levin, G.; Szwarc, M. *J. Am. Chem. Soc.*, **1975**, 96, 258.
(b) Abdul-Rahim, O.; Simonov, A. N.; Boas, J. F.; Ruther, T.; Collins, D. J.; Perlmutter, P.; Bond, A. M. *J. Phys. Chem. B*, **2014**, 118, 3183.
- [27] Moore, W. M.; Morgan, D. D.; Stermitz, F. R. *J. Am. Chem. Soc.* **1963**, 85, 829.
- [28] Yamaguchi, H.; Kobayashi, Y.; Kobayashi, R.; Takashima Y.; Hashidzume, A.; Harada, A. *Nat. Commun.* **2012**, 3:603.
- [29] Suresh, P.; Pitchumani, K. *J. Photochem. Photobiol. A: Chem.* **2009**, 206, 40.
- [30] Granadero, D.; Bordello, J.; Pérez-Alvite, M. J.; Novo, M.; Al-Soufi, W. *Int. J. Mol. Sci.* **2010**, 11, 173.
- [31] Herrmann, W.; Wehrle, S.; Wenz, G. *Chem. Commun.* **1997**, 0, 1709.
- [32] Wagner, B. D.; Fitzpatrick, S. *J. Inclus. Phen. Macrocyclic Chem.*, **2000**, 38, 467.
- [33] Chen, Y.; Zhang, Y.-M.; Liu, Y. *Chem. Commun.* **2010**, 46, 5622.
- [34] Hallet-Tapley, G. L.; D'Alfonso, C.; Pacioni, N. L.; McTiernan, C. D.; González-Bejar, M.; Lanzalunga, O.; Alarcon, E. I.; Scaiano, J. C. *Chem. Commun.* **2013**, 49, 10075.
- [35] K. H. Poon and Y. Cheng, *J. Incl. Phenom. Macrocycl. Chem.*, 2008, **60**, 211.
- [36] (a) Lim, C.-K.; Li, X.; Li, Y.; Drew, K. L. M.; Palafox-Hernandez, J. P.; Tang, Z.; Baev, A.; Kuzmin, A. N.; Knecht, M. R.; Walsh, T. R.; Swihart, M. T.; Ågren H.; Prasad, P. N. *Nanoscale*, **2016**, 8, 4194.
(b) Miyazawa, T.; Koshihara, S.; Segawa, Y.; Kira, M. *Chem. Lett.*, **1995**, 217.
- [37] (a) Park, C.; Youn, H.; Kim, H.; Noh, T.; Kook, Y. H.; Oh, E. T.; Park, H. J.; Kim, C. *J. Mater. Chem.*, **2009**, 19, 2310.
(b) Alvarez, J.; Liu, J.; Román, E.; Kaifer, A. E. *Chem. Commun.*, **2000**, 36, 1151.
(c) Liu, Y.; Yang, Y.-W. Chen, Y. *Chem. Commun.* **2005**, 41, 4208.
- [38] Rao, K. S. S. P.; Hubig, S. M.; Moorthy, J. N.; Kochi, J. K. *J. Org. Chem.* **1999**, 64, 8098.

- [39] Yang, C.; Ke, C.; Liang, W.; Fukuhara, G.; Mori, T.; Liu, Y.; Inoue, Y. *J. Am. Chem. Soc.* **2011**, 133, 13786.
- [40] Ikeda, H.; Nihei, T.; Ueno, A. *J. Org. Chem.* **2005**, 70, 1237.
- [41] Yang, Y.; Mori, T.; Inoue, Y. *J. Org. Chem.* **2008**, 73, 5786.
- [42] El-Desoky, H.; Heinze, J.; Ghoneim, M. M. *Electrochem. Commun.* **2001**, 3, 697.
- [43] Nakamura, A.; Inoue, Y. *J. Am. Chem.* **2003**, 125, 966.
- [44] Carey, F. A.; Sundberg, R. J. New York, *Kluwer Academic/Plenum Publishers*, **2004**.